4. Crystallization and Glass-Ceramics

Mathieu Allix, Laurent Cormier

Glass-ceramics are innovative technological materials made up of crystals dispersed in a glass matrix. This dual feature enables the combination of the advantages of glass, mostly ease of shaping/forming, with the specific properties of crystalline phases. Since their discovery in the 1950s, numerous studies have been devoted to glass crystallization mechanisms. Such an understanding is of primary importance to further design glass-ceramics with tailored properties that are closely related to their microstructure. This chapter will thus start with a description of the different nucleation and growth processes. Some practical examples will be provided to illustrate the particular interest of nucleating agents and phase separation in order to master nucleation and growth processes. A brief overview of the complementary characterization techniques used to finely describe the multiscale structure of these glass-ceramic materials will then be presented. Finally, the large range of accessible glass-forming compositions and microstructures will be illustrated by a variety of technological materials combining mechanical, thermal, optical, energetic, and bioactive properties.

4.1 Tailoring Glass Crystallization for Glass-Ceramic Processing

Crystallization from glass is a fascinating fundamental process which leads to the elaboration of glass-ceramics, innovative materials containing at least one amorphous and one crystalline phase. Controlling the crystallization process in glass to tailor unique physical properties in glass-ceramics became possible after the serendipitous discovery by D. Stookey from Corning Glass Works in 1953. After he accidentally overheated a lithium silicate glass with dispersed silver nanoparticles, the as-synthesized glass-ceramic material showed enhanced mechanical properties. Actually, crystallization not only improves the mechanical properties but may also affect various physical properties (optical, electrical, magnetic, thermal, machinability, biocompatibility, etc.) over a large range of glass compositions [4.1]. This discovery opened the way to a new class of materials, glass-ceramics, with numerous applications. Great commercial success has been encountered in several areas so far [4.2]: domestic (heat-resistance cookware or cooktops, fireproof windows), health (dental restoration, bioactive materials for bone replacement), space (radome), electronics (substrate for electronic packaging, magnetic memory discs), architecture, coating and sealing materials, waste management, etc. Moreover, the development of new synthesis methods is foreseen to extend the available functional glass-ceramic compositions in the near future.

J.D. Musgraves, J. Hu, L. Calvez (Eds.), *Springer Handbook of Glass*, Springer Handbooks, https://doi.org/10.1007/978-3-319-93728-1_4

Understanding the nucleation and growth processes is mandatory for developing glass-ceramic materials. Therefore, this chapter starts with a theoretical description of the two main crystallization mechanisms generally considered: homogeneous nucleation taking place randomly within the glass volume and heterogeneous nucleation arising at external surfaces or impurity interfaces. The glass-ceramic industry strongly developed the second process which is usually induced by the addition of nucleating agents. These latter improve glass crystallization kinetics and allow surface crystallization to be avoided. Although glass-ceramics have found industrial applications since the mid of the twentieth century, nucleation and growth have remained hot topics of research since the pioneering Gibbs's works [4.3]. The classical nucleation theory (CNT) is the most widely used and simplest approach to understanding crystallization mechanisms, based on the appearance of nuclei. It considers that a nucleation event takes place in most liquids due to fluctuations. This step leads to the formation of a nucleus preceding the growth stage. Nucleation is the key factor, although the less understood, since critical nuclei have a nanometer size and a short lifetime that usually hinder their experimental observation. However, the development of in situ or atomistic characterization tools and computational studies has recently enabled researchers to probe atomistic, molecular, and nanometer ranges with unprecedented resolution, providing valuable information to go beyond the classical nucleation picture.

Glass-ceramics are usually produced by controlled crystallization from glass using appropriate thermal treatment. The macroscopic properties of a glass-ceramic material are not only closely related to the composition of the parent glass but they also depend to a great extent on the nature and the microstructure of the crystalline phases. The nature of the crystalline phase, the size distribution, the shape of the crystals, and the microstructure are key parameters that must be controlled to foster specific properties. A precise control of the glass-ceramics microstructure and of the structural modifications taking place during crystallization must be finely achieved. The contribution of numerous complementary techniques (thermal analysis, diffraction, electron microscopy, spectroscopies, etc.) available to observe and characterize multiscale organization during crystallization are discussed and illustrated in Sect. 4.4. During the design of a glass-ceramic material with specific properties, it is of great importance to tailor the crystallization mechanism to determine the adapted elaboration process leading to the desired microstructure. Some of these processes are detailed in this chapter, ranging from the classic use of nucleating agents favoring strong volume crystallization to the modern laser irradiation process opening the way to the design of glass-ceramics with complex 3-D structuration. Lastly, the large range of accessible glass-forming compositions combined with the development of diverse microstructures enables the elaboration of glass-ceramics with various properties. Recent remarkable applications and developments are detailed in Sect. 4.5, with a focus on establishing the link between the microstructure of the glass-ceramic material and the associated properties.

4.2 Theoretical Description of Glass Crystallization

Crystallization can be described as the formation of a solid crystalline phase from an amorphous state, leading to a glass-ceramic material at ambient temperature, in which crystals are embedded in the glass matrix. It is therefore essential to understand the phenomenon of crystallization in order to control the size, morphology, distribution, and the nature of the crystalline phases that will be formed. Crystallization can occur directly during cooling from the melt [4.4], but the crystal phase and size are difficult to control and therefore this event is generally not desired.

The classic crystallization process involves two steps: a nucleation at low temperature (often slightly above the glass transition temperature T_g) followed by crystal growth at higher temperature.

Nucleation mechanisms are historically modeled by the classical nucleation theory (CNT). This theory derives from the historical work of *Gibbs* [4.5] and Arrhenius, which was then taken up and developed by *Volmer* [4.6] and later by *Becker* and *Döring* [4.7]. Only the basics of this model will be presented here. A more detailed description is available in various books [4.1, 2].

CNT is based on two fundamental assumptions (the so-called capillary approximations, coming from the Gibbs thermodynamic model that describes the interface in a two-component system [4.5]) allowing a simple and understandable approach to the thermodynamic processes in play:

- The quantities associated with the nucleus (a small group of atoms having a crystalline arrangement) are considered identical to those of the macroscopic crystal, regardless of its size, which implies the

same properties, thermodynamic values, structure, composition, and density.
- The nucleus is spherical in shape (radius r) in order to minimize the surface energy with a sharp boundary between the nucleus and the liquid.

We shall see that this model is, however, imperfect and is today supplemented by more comprehensive but also more complex approaches (Sect. 4.2.4).

4.2.1 The Classical Nucleation Theory

Nucleus formation can occur by two general mechanisms: homogeneous nucleation in the volume or heterogeneous nucleation triggered by surfaces and impurity interfaces.

Phase Transformation

Thermodynamically, the stability of a phase is determined by its Gibbs free energy (G or free enthalpy). As crystallization is a first-order phase transition, it is accompanied by a change of its Gibbs free energy, usually due to a change in temperature, in order to minimize G and to reach equilibrium at a given temperature.

Above the melting temperature (T_m for a pure body, $T_{liquidus}$ for a mixture), the equilibrium phase corresponds to the liquid state, having the lowest free energy, and the crystalline state is not stable. When $T < T_m$, the supercooled liquid is in a metastable state and the crystalline solid phase has the lowest free energy and, hence, is the most stable phase. The volumic free-energy difference, ΔG_V, is defined as the difference between the free energy of the supercooled liquid, G_L, and that of the crystal, G_C, per unit of volume

$$\Delta G_V = G_C - G_L < 0 \quad \text{for} \quad T < T_m \,. \tag{4.1}$$

Above T_m, the liquid-to-crystal phase transition is not thermodynamically possible, whereas below T_m, the phase transformation is thermodynamically driven by ΔG_V. Since ΔG_V increases when the temperature decreases, crystals must appear spontaneously with an increasing driving force as the supercooling increases. This degree of supercooling, ΔT, is measured as the difference between the temperature T of the system and T_m, such as $\Delta T = T_m - T$.

The change in free energy associated with the liquid–crystal transformation can also be written as a function of the change in volumic enthalpy $\Delta H_V = -L_V < 0$ with L_V the latent heat of melting, and the associated change in entropy, $\Delta S_V = S_C - S_L < 0$

$$\Delta G_V = \Delta H_V - T\Delta S_V \,, \tag{4.2}$$

ΔH_V corresponds to the heat released during crystallization and is a constant. The variation in free energy comes only from the temperature dependence of the second, entropic, term in equation (4.2). When T increases, the entropic term ($T\Delta S_V$) also increases, which favors crystal formation.

At T_m, the free-energy difference is zero because the crystal and liquid have the same free energy

$$(\Delta G_V)_{T_m} = \Delta H_V - T\Delta S_V = 0 \tag{4.3}$$

which leads to

$$\Delta G_V = \Delta H_V \frac{\Delta T}{T_m} \,. \tag{4.4}$$

Equation (4.4) indicates that the thermodynamic driving force for crystallization increases with the degree of supercooling.

Homogeneous Nucleation

Homogeneous nucleation is a spontaneous and stochastic event, resulting from local fluctuations of density, composition, or organization, in relation to temperature variation. This kind of nucleation process is only observed for a small number of compositions. When the crystalline phase has the same composition as the initial glass, this is a special case referred to as congruent crystallization.

The thermodynamic approach used in the classical nucleation theory considers the system initially in a metastable state (supercooled liquid) that may evolve by thermal activation to reach its thermodynamically stable state, corresponding to the macroscopic crystal. Therefore, a nucleus will be promoted and stabilized if the Gibbs free energy (G) is minimized (Fig. 4.1a). This phase transition is favored by the volumic free-energy difference between the crystal and the liquid (ΔG_V), which is the thermodynamic driving force for crystallization. The gain is proportional to the volume of the new phase. To achieve this phase change, an energetic barrier must be overcome, which corresponds to the formation of an interface between the nucleus and the supercooled liquid (associated with a nucleus/liquid surface tension γ). The energy cost to form this interface is proportional to the surface area (S) of the nucleus.

The work of formation W takes into account the different thermodynamic aspects of the phase transition leading to the formation of a spherical nucleus of radius r

$$W = 4\pi r^2\gamma + \frac{4\pi}{3} r^3 \Delta G_V + \Delta G_E \,, \tag{4.5}$$

with ΔG_E the elastic energy, which is often overlooked for a solid–liquid transformation since the liquid relaxes quickly.

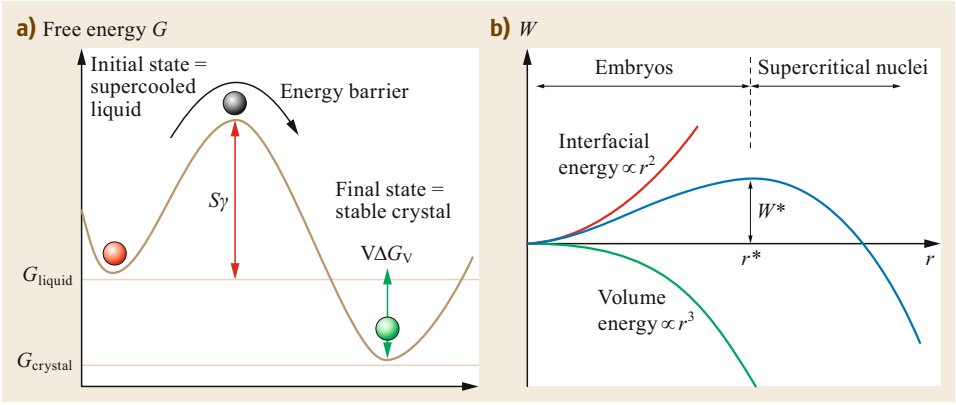

Fig. 4.1 **(a)** Energy diagram illustrating the liquid to crystal phase transition. **(b)** Variation of the work of formation (W) of a spherical nucleus with a radius r (*blue curve*) including the surface (*red curve*) and volume (*green curve*) components as a function of r

The work of formation W corresponds to the competition between the interfacial term (thermodynamic barrier to surmount) and the volumic term which favors nucleation (Fig. 4.1b).

The maximum of the work of formation W^* is obtained by the first derivative of W relative to the nucleus radius, $\partial W/\partial r = 0$. The extremum corresponds to a critical radius r^* which is equivalent to the minimum size that a nucleus must reach to allow for irreversible crystal growth

$$r^* = -\frac{2\gamma}{\Delta G_V} \quad \text{and} \quad W^* = \frac{16}{3}\frac{\gamma^3}{\Delta G_V^2}\,. \tag{4.6}$$

For $r < r^*$, W is dominated by the surface energy. The nucleus, called embryo, is not stable and is dissolved with a high probability after its appearance, in order to reduce the free energy of the system.

For $r > r^*$, the nucleus is defined as supercritical and can grow since an increase of its radius entails a reduction of W and therefore of the free energy of the system.

As the degree of supercooling increases, the thermodynamic driving force increases and W is lowered. The crystallization should thus be favored. However, kinetic aspects must be taken into account. Indeed, the nucleus formation requires that atoms (or structural units) move from the liquid to the crystal/liquid interface. The diffusion atomic rate is associated with a diffusion activation energy, ΔG_D, which is related to the diffusion coefficient, D

$$D = \frac{k_B T l^2}{h}\exp\left(-\frac{\Delta G_D}{k_B T}\right), \tag{4.7}$$

with k_B and h the Boltzmann and Planck constants, respectively, and l the jump distance.

Since the diffusion coefficients are rarely known and their measurements are complex, the Stokes–Einstein relation is usually used

$$D = \frac{k_B T}{6\pi l \eta}\,. \tag{4.8}$$

This equation considers that viscous flow controls mass transport and the kinetic term can be approximated by the viscosity, η, that can be easily measured.

The steady-state homogeneous nucleation rate, $I(T)$, defines the number of critical nuclei appearing per volume unit and per time unit (I in $m^{-3}s^{-1}$) and it can be expressed as a thermally activated process implying the thermodynamic and kinetics parts [4.8]

$$I(T) = I_0 \exp\left(-\frac{W^* + \Delta G_D}{k_B T}\right), \tag{4.9}$$

$$I_0 = 2N_1 \frac{k_B T}{h}\left(\frac{a^2\gamma}{k_B T}\right)^{1/2}, \tag{4.10}$$

with N_1 the number density of structural units of size a.

Figure 4.2 illustrates the shape of $I(T)$. As the temperature decreases, there is a first metastable zone where no nucleation can occur since the thermodynamic term is dominated by the surface effects (no critical nucleus can form). As T continues to decrease, the thermodynamic driving force dominates the surfacic term and the nucleation rate increases, until reaching the maximum nucleation rate at T_N. When the kinetic barrier begins to control the process ($T < T_N$), the atomic mobility is reduced as the viscosity increases and critical fluctuations are less probable, thereby decreasing $I(T)$ as T decreases.

Examples of Homogeneous Nucleation

There are only a few glasses that exhibit homogeneous nucleation. In stoichiometric glass-forming systems, the macroscopic crystalline phase and the initial glass have the same composition (congruent crystallization). However, for some glasses, the final crystal reaches

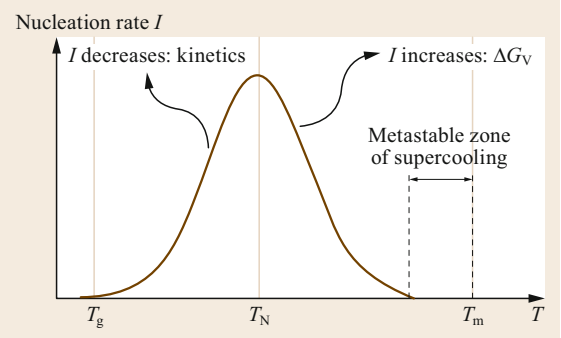

Fig. 4.2 Evolution of the nucleation rate with temperature (T_g = glass transition temperature; T_N = temperature of maximum nucleation; T_m = melting temperature). Compared to homogeneous nucleation, heterogeneous nucleation will shift the curve $I(T)$ to lower temperature and the maximum intensity will increase

the stoichiometric composition of the initial glass but after a heterogeneous nucleation (Table 4.1). This observation denotes that metastable crystalline phases, not necessarily congruent, can appear at intermediate stages [4.9–11]. These transient phases act as a precursor for the formation of a more stable macroscopic phase, implying more complex pathways than suggested by the CNT.

On the basis of experimental observations, a simple rule has been proposed to predict the nucleation mechanism using the reduced glass transition temperature ($T_{gr} = T_g/T_{liquidus}$). For compositions with $T_{gr} <$ 0.58–0.60, internal homogeneous nucleation is observed, while for glasses with higher values of T_{gr}, mainly surface nucleation occurs [4.8]. Using this criteria, ≈ 90% of silicate glasses have $T_{gr} > 0.60$ while most metallic alloys exhibit $T_{gr} < 0.60$, which can explain why the latter are poor glass-formers [4.8]. Figure 4.3 illustrates this trend for 51 glass compositions: the maximum nucleation rate drops when T_{gr} decreases, which is accompanied by an increase in the time-lag of nucleation at T_{max} (insert of Fig. 4.3a). As the maximum nucleation rate drastically drops, the time lag of nucleation (time before reaching a steady-state regime in the nucleation process, see Sect. 4.2.1, *Induction Time*) increases (Fig. 4.3b).

The density difference between the glass and the crystalline phase can also provide some clues regarding the nature of the nucleation mechanism [4.15, 16]: a low density difference (1.8% for $Na_2Ca_2Si_3O_9$) is observed for homogeneous (volume) nucleation, while a high density difference (18.5% for $CaMgSi_2O_6$) can accompany a strong surface nucleation. However, this criterion is very qualitative and must be used carefully.

Another important relationship has been proposed between glass/crystal structure and crystallization processes. Structural similarities or dissimilarities between the glass and the compositionally equivalent crystal can correlate strongly with homogeneous or heterogeneous events, respectively. Indeed, a homogeneous nucleation can be favored when small structural reorganization is required, which is especially important just above the glass transition temperature where nucleation occurs and viscosity is high. As shown by EXAFS investigation [4.17], the short-range order around cations is similar in glasses nucleating homogeneously. Conversely, the local environment is different between the

Table 4.1 Glass compositions that exhibit homogeneous or heterogeneous nucleation [4.12–15]

Composition	Homogeneous/heterogeneous	Crystalline phase
Li_2O-SiO_2	Homogeneous	Li_2SiO_3
Li_2O-$2SiO_2$	Homogeneous	$Li_2Si_2O_5$
Na_2O-SiO_2	Homogeneous	Na_2SiO_3
CaO-SiO_2	Homogeneous	$CaSiO_3$
BaO-SiO_2	Homogeneous	β-$BaSi_2O_5$, $Ba_5Si_8O_{21}$
BaO-$2SiO_2$	Homogeneous	$BaSi_2O_5$
Na_2O-$2CaO$-$3SiO_2$	Homogeneous	$Na_2Ca_2Si_3O_9$
$2Na_2O$-CaO-$3SiO_2$	Homogeneous	$Na_4CaSi_3O_9$
$2BaO$-TiO_2-$2SiO_2$	Homogeneous	$Ba_2TiSi_2O_8$
Li_2O-$2B_2O_3$	Homogeneous	$Li_2B_4O_7$
CaO-MgO-$2SiO_2$	Heterogeneous	$CaMgSi_2O_6$
CaO-Al_2O_3-$2SiO_2$	Heterogeneous	$CaAl_2Si_2O_8$
Na_2O-Al_2O_3-$6SiO_2$	Heterogeneous	$NaAlSi_3O_8$
PbO-SiO_2	Heterogeneous	$PbSiO_3$
Na_2O-$2B_2O_3$	Heterogeneous	$Na_2B_4O_7$
Na_2O-$2SiO_2$	Heterogeneous	$Na_2Si_2O_5$
K_2O-$2SiO_2$	Heterogeneous	$K_2Si_2O_5$
B_2O_3	No nucleation	B_2O_3

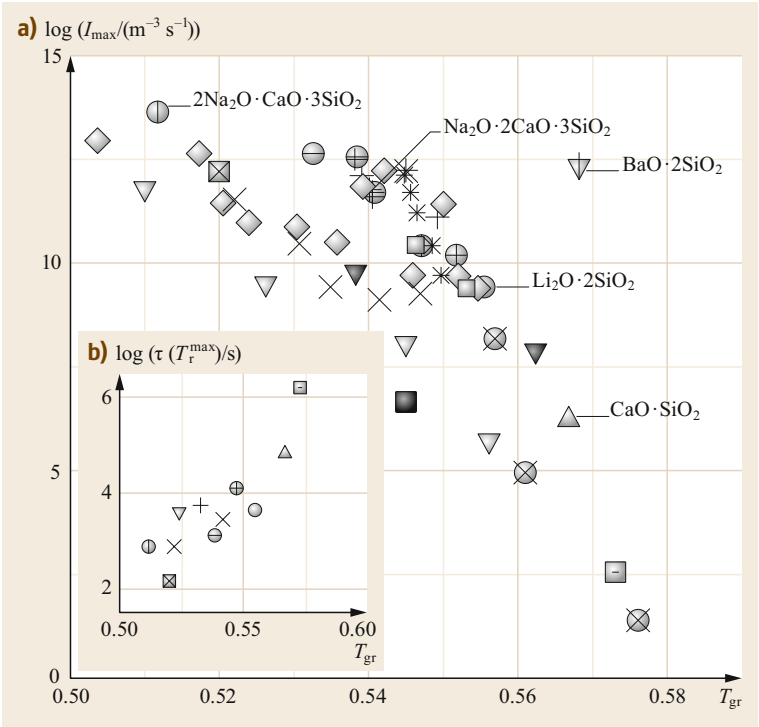

Fig. 4.3 **(a)** Maximum nucleation rates as a function of the reduced glass transmission temperature $T_{gr} = T_g/T_{liquidus}$ for 51 glass compositions displaying homogeneous nucleation. **(b)** Time-lag of nucleation at T_{max} (after [4.12])

glass and its isochemical crystal phases in the case of heterogeneous nucleation. The connectivity of the silicate network, particularly the Q^n species distribution, also correlates with the nucleation mechanisms [4.16]. Recently, investigation at medium-range distance revealed the importance of this scale. In lithium borate and silicate glasses [4.18–20], the medium-range order for the borate network and Li distribution is similar in the glass and the crystal and homogeneous nucleation is favored. Conversely, for sodium borate and silicate glasses displaying heterogeneous nucleation, topological differences can exist, such as a more three-dimensional structure for the sodium diborate glass as opposed to a layered structure for the isochemical crystal. The network topology can influence nucleation as a structure of low dimensionality is expected to reorganize more easily than a three-dimensional structure in which the degrees of freedom are reduced.

Induction Time

Equation (4.9), describing the nucleation rate is based on a stationary (steady-state) regime for nucleation. However, this steady state may not occur immediately after changing the experimental conditions (for instance following temperature variation) and, at the very beginning of the transformation, a transient regime exists, corresponding to the period required to achieve a quasisteady state distribution of embryos. This non-stationary regime is characterized by a time-lag, or an incubation time, τ.

The transient nucleation rate was described by *Kashchiev* who performed a numerical integration of the kinetics equation describing nucleation [4.21]

$$I(t) = I_{st}\left[1 + 2\sum_{m=1}^{\infty}(-1)^m \exp\left(-m^2\frac{t}{\tau}\right)\right]. \quad (4.11)$$

By integrating this equation, the time dependence of the number of supercritical nuclei per unit volume can be calculated

$$\frac{N_V(t)}{I_{st}\tau} = \left[\frac{t}{\tau} - \frac{\pi^2}{6} - 2\sum_{m=1}^{\infty}\frac{(-1)^m}{m^2}\exp\left(-m^2\frac{t}{\tau}\right)\right], \quad (4.12)$$

with I_{st} the steady state nucleation rate defined in (4.9).

For a sufficiently long time ($t \gg \tau$), the approximate expression in which $N_V(t)$ is linear with time can be obtained

$$N_V(t) = I_{st}\left(t - \frac{\pi^2}{6}\tau\right). \quad (4.13)$$

It is then possible to experimentally determine τ as the intercept with the time axis of the tangent to the

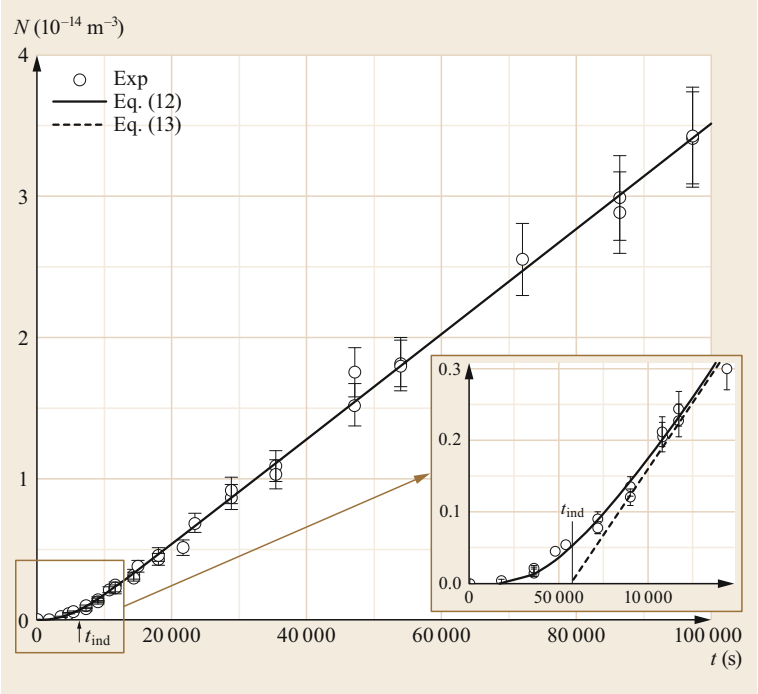

Fig. 4.4 Variation of the density of crystal, N, with time at a temperature of 610 °C for a Na_2O-CaO-SiO_2 glass. The induction time is obtained from *solid* and *dashed curves* using (4.12) and (4.13), respectively (after [4.22])

$N_V(t)$ curve (dashed line in Fig. 4.4). A more rigorous determination of τ can be performed by fitting the experimental values of $N_V(t)$ with (4.12) (continuous line in Fig. 4.4).

Heterogeneous Nucleation

In glass-ceramics, heterogeneous nucleation is a much more common phenomenon than homogeneous nucleation. Specific sites such as interfaces with surfaces, inclusions, impurities, and bubbles can trigger nucleation. Heterogeneous nucleation can correspond either to a volume (especially with the use of nucleating agents or for glasses showing propensity to phase separation) or a surface mechanism. The effective interfacial energy is lower on these *catalysts* resulting in a lower energy barrier (Fig. 4.1). Therefore, heterogeneous nucleation will be faster than homogeneous nucleation.

CNT can also be used to model heterogeneous nucleation using simple adaptations of the homogeneous model. Two changes are involved:

- A geometric change: nuclei no longer have the form of complete spheres, but correspond to spherical caps (Fig. 4.5) defined by a contact angle θ ($\theta = 0$ for a perfect wetting contact and $\theta = 180°$ for point contact with the flat surface). The interfacial energy decreases with the contact angle, which increases the nucleation rate.

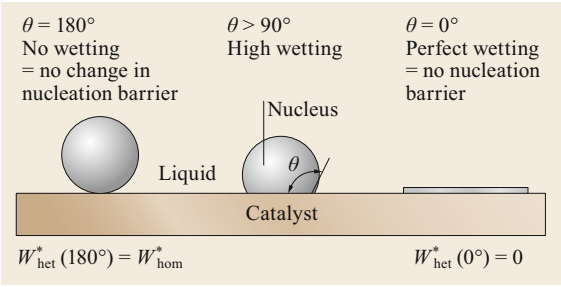

Fig. 4.5 Scheme of three cases of contact angle, θ between the catalyst/nucleus interface and the nucleus/liquid interface. No wetting corresponds to homogeneous nucleation. As θ decreases, heterogeneous nucleation is favored and increases

- An energy amendment: the thermodynamic diagram is similar to that of the homogeneous nucleation, but the interfacial energy must take into account all interfaces (solid–liquid, solid–substrate, substrate–liquid).

These changes reduce the heterogeneous work of formation (W_{het}) by a factor $f(\theta)$ compared to the homogeneous nucleation (W_{hom})

$$W_{het} = W_{hom} f(\theta)$$
$$\text{with} \quad f(\theta) = \frac{(2+\cos\theta)(1-\cos\theta)^2}{4} . \qquad (4.14)$$

The kinetic contribution is not modified. Since $f(\theta) \leq 1$, the heterogeneous nucleation rate is always higher than the homogeneous nucleation rate. Conversely, the critical nucleus radius r^* remains identical to that obtained by homogeneous nucleation. Therefore, the contact angle, θ, is the key parameter to determine the energy benefit brought by heterogeneous nucleation. To favor nucleation, the contact angle has to be minimized.

Comparison of CNT Theory and Experiment

The comparison between the predictions of the CNT and the experimental data shows important quantitative disagreements. A typical example (Fig. 4.6) is the CNT predictions and experimental nucleation rates obtained on several silicate binary systems [4.23]. Although the temperature dependence is well described by the CNT, large discrepancies exist in the magnitude between the predicted and experimental nucleation rates. The CNT largely underestimates the nucleation rate by over 30–55 orders of magnitude!

The explanations of the CNT failure are numerous and mainly related to the approximations used at the basis of the theory:

- The macroscopic thermodynamic properties are used to describe the crystalline nuclei. This approximation (thermodynamic hypothesis, capillary approximation) is challenged by experimental observations showing that metastable phases may precipitate in the first nucleation steps and compositional change can occur during crystallization (mutant crystals) [4.15, 24, 25].
- The finite nucleus/liquid interface implies that the macroscopic surface tension is independent of the nucleus size (curvature) and the temperature (thermodynamic hypothesis, capillary approximation).
- The attachment of species at the nucleus/liquid interface is often approximated with the relaxation shear or the viscous flow of the liquid (kinetic hypothesis, Stokes–Einstein relation). A possible decoupling between the diffusion and relaxation phenomena usually prevents the use of viscosity to describe the diffusion processes, especially near T_g [4.26].
- The assumption that the supercooled liquid is homogeneous is challenged by recent experimental and theoretical works, revealing static heterogeneities [4.27–30].

Ostwald's Rule

The CNT is also unable to predict the qualitative pathways for nucleation, particularly in complex systems. Indeed, CNT describes the nucleation by using just one order parameter: the nuclei are simply considered as small clusters cut out of the macroscopic crystal, as-

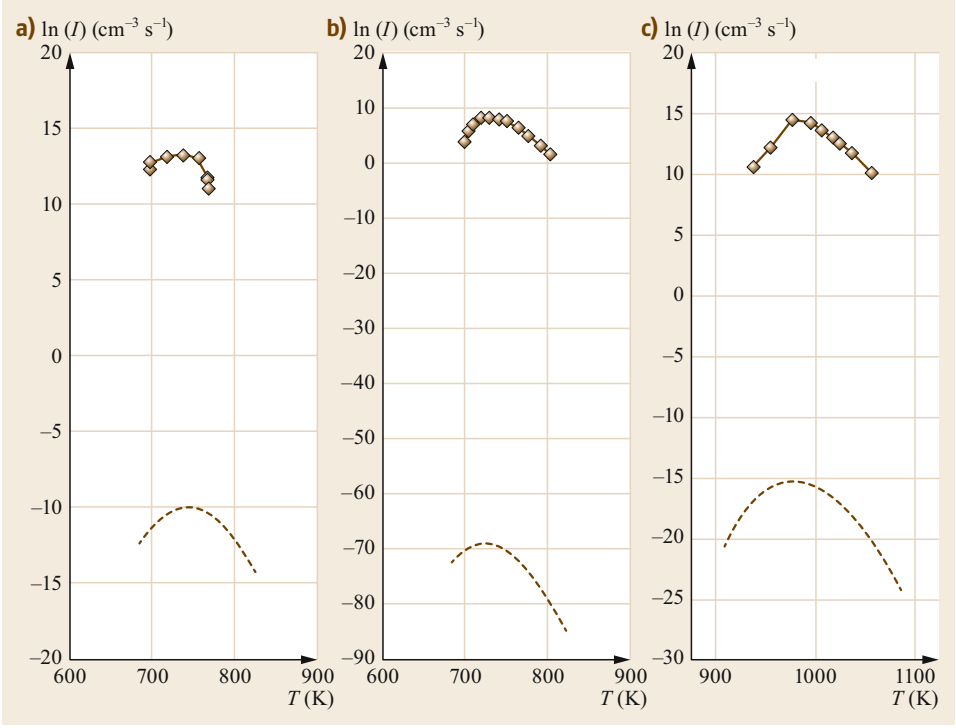

Fig. 4.6a–c Nucleation rates $I(T)$ obtained from experiments (*symbols*) and predicted by the CNT (*dashed lines*) for **(a)** Na_2SiO_3, **(b)** $Li_2Si_2O_5$, and **(c)** $BaSi_2O_5$ systems, showing large-magnitude discrepancies (after [4.23])

sumed to have the same composition, structure, and properties of the bulk solid. Recent alternative nonclassical theories consider different pathways, enabling the subcritical nuclei (or embryos) to evolve during the crystallization process [4.31].

Such pathways are consistent with the step rule proposed by *Ostwald* in 1897 [4.32]:

> in the course of transformation of an unstable (or metastable) state into a stable one, the system does not go directly to the most stable conformation (corresponding to the modification with the lowest free energy) but prefers to reach intermediate stages (corresponding to other metastable modifications) having the closest free energy to the initial state.

In accordance with this rule, every system prefers to evolve into ephemeral metastable phases with increasing stability (lower free energy) rather than directly reaching the final stable state (Fig. 4.7). The consequence is the possibility of formation of one or more intermediate metastable phases before equilibrium is reached.

Although this rule has no theoretical foundation, there is much experimental evidence that one or more metastable phases are formed before the stable one. A striking experiment has been performed recently using high-resolution electron microscopy allowing direct visualization of the successive intermediate phases during the nucleation of amorphous $LiFePO_4$ [4.33].

4.2.2 Theory of Crystal Growth

After nucleation, when the nucleus has reached the critical size r^*, crystal growth is the main process occurring. The growth rate is controlled by three factors:

- The rate of diffusion of atoms (or structural units) from the liquid to the interface with the nucleus.
- The rate of reaction between atoms and the surface of the crystal. The nature of the interface is therefore essential regarding the kinetic growth and future crystal morphology.
- The rate at which the thermal energy release is extracted (latent heat).

The growth rate, $U(T)$, takes into account the rates at which an atom or structural unit is attached or detached from the crystal surface and the thermodynamic driving force ΔG_V

$$U(T) = Ad\nu \exp\left(-\frac{\Delta G_D}{k_B T}\right)\left[1 - \exp\left(\frac{\Delta G_V}{k_B T}\right)\right], \tag{4.15}$$

with A the fraction of sites available for attachment at the crystal surface, d the jump distance (interatomic distance), and ν the frequency of the atomic vibration. ΔG_D is related to the effective diffusion coefficient of the atom or unit species that control attachment at the liquid/crystal interface. Just below $T_{liquidus}$, the diffusion coefficients can be deduced from the macroscopic viscosity via the Stokes–Einstein relation (4.8). This approximation is not necessarily valid at large degrees of supercooling, near T_g, and must thus be used carefully in the CNT. In practice, a linear growth rate ($m\,s^{-1}$), derived from the measurement of the crystal size at different times, is usually measured experimentally [4.34].

Figure 4.8 shows an example of the nucleation and growth rate curves. One can note that the low temperature part is dominated by the kinetic component whereas the high temperature part is controlled by the energy balance.

T_N is the temperature at the maximum of nucleation rate when the number of nuclei is maximized and T_C

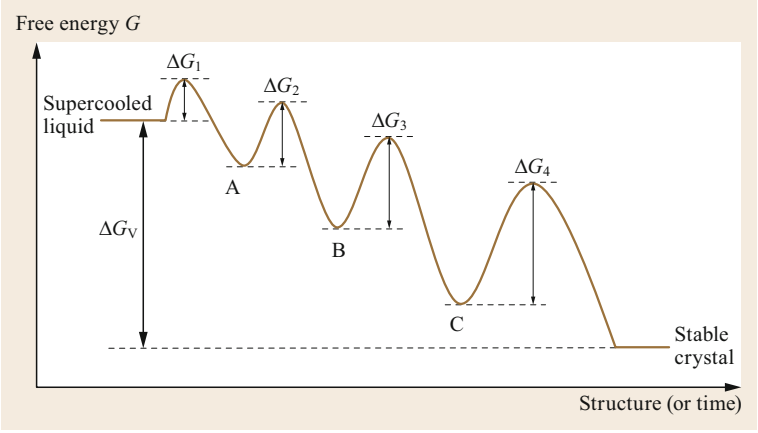

Fig. 4.7 Diagram representing the nucleation pathway through different intermediate metastable phases of increasing stability (A, B, C) before finally obtaining the stable equilibrium phase (according to [4.33])

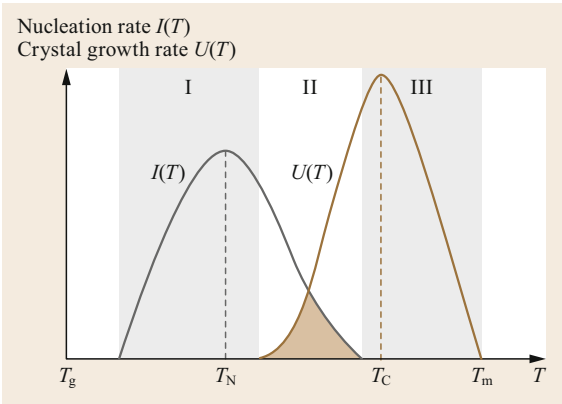

Fig. 4.8 Variation of the nucleation rate $I(T)$ and crystal growth rate $U(T)$ with temperature

is the temperature at the maximum of growth rate. It is important to note that the two rates do not have the same units and therefore have very different values. For example, for Li_2O-$2SiO_2$, the maximum nucleation rate is $\approx 4\times10^9\,m^{-3}\,s^{-1}$ and the maximum growth rate $7\times10^{-5}\,m\,s^{-1}$.

From Fig. 4.8, the crystallization rate can be divided into three parts. In region I, nuclei are formed but cannot grow. Region II shows an overlap of $I(T)$ and $U(T)$ curves and thus correspond to the area of crystallization. The width of this area may vary strongly depending on the type of glass. Lastly, region III indicates no nucleation so that no crystallization can occur.

The progress of the crystallization front can be homogeneous or well located on the nucleus/crystal interface, inducing a strong anisotropic growth leading for example to dendritic crystals (Sect. 4.4.2, *Microstructures from Surface Crystallization*) [4.35]. Crystal morphology is therefore highly dependent on the type of growth mechanism in play.

4.2.3 Transformation Kinetics

Crystal growth kinetics can be controlled by heat flow, mass transfer, and intrinsic reactions at the liquid/crystal interface. The latent heat of crystallization results from the formation of the crystal ($\Delta H_V < 0$) and must be removed into the surroundings. If removal of ΔH_V is lower than its production, the temperature near the liquid/crystal interface rises and the growth rate decreases. Diffusion (atomic or structural species) is needed to feed the growing crystal, particularly if the crystal composition differs from the liquid one. The heat and mass transfers imply temperature and compositional gradients near the interface. Another major rate-limiting process of crystal growth can be the interface reaction mechanism which describes the probability of attachment of an atom or a structural unit to the crystalline surface.

In the case of long-range diffusion, the growth rate, U, of a flat interface can be measured with the crystal size, which exhibits a square root of time dependence [4.36]

$$U = k\left(\frac{D}{t}\right)^{1/2}, \tag{4.16}$$

with k a constant involving concentration terms and D the diffusion coefficient of the rate-controlling species in the liquid. In the case of short-range diffusion, the growth rate is independent of time (linear relationship between crystal size and t). However, this behavior is also encountered if the rate-controlling process is removal of latent heat or reaction at the liquid/crystal interface.

Johnson, *Mehl*, *Avrami*, and *Kolmogorov* proposed a model (JMAK) to describe phenomenologically the kinetics of isothermal crystallization [4.37–39]. The crystallinity of a glass-ceramic corresponds to the ratio $\alpha = V_\beta/V$, where V_β is the transformed (crystallized) volume and V the total volume of the material. During a homogeneous transformation leading to the phase β, α can be written as a function of the crystallization time t by the formula

$$\alpha = \frac{V_\beta}{V} = 1 - \exp(-kt^n)\,, \tag{4.17}$$

k the reaction rate constant and n the Avrami exponent ($3 \le n \le 4$) can provide information on the crystallization mechanism [4.36, 40] such as the nucleation type (homogeneous versus heterogeneous) or the crystal growth geometry (spherulite, disc, rod). These values can be experimentally determined by measuring the volume fraction converted versus time, for instance by differential scanning calorimetry (DSC); see Chap. 24 for more information.

Moreover, obtaining the transformed fraction at different temperatures allows a time-temperature-transformation diagram (TTT) to be constructed, leading to the kinetics of isothermal transformation [4.2].

However, the real crystallization process often deviates from simple interpretation of k and n and it is recommended that additional characterizations be carried out by an experimental technique such as optical and/or electron microscopy to reinforce the determination of the type of mechanism involved.

4.2.4 Nonclassical Pathways of Nucleation

Although the classical nucleation theory describes correctly and qualitatively the physical phenomena ob-

served during the crystallization process, it fails over many orders of magnitude to show quantitative agreement. This mismatch can be mostly explained by the initial assumptions of the CNT (Sect. 4.2.1, *Comparison of CNT Theory and Experiment*) [4.41, 42].

To overcome these limitations, new theories have emerged, either supplementing the classical view or proposing innovative approaches [4.23, 42, 43]. A more general approach than CNT is the cluster dynamics (or kinetic approach) [4.44, 45] that considers the temporal evolution of a population of clusters, without considering their size. Many approximations are required in practice and this theory has only been sparsely applied to oxide systems [4.44, 46, 47].

The thermodynamic density functional theory (DFT), or phase-field method, is used to describe the spatiotemporal evolution of certain quantities (fields) such as concentration. As shown in *Cahn* and *Hilliard's* works [4.48–50], important results were derived from this approach: a diffuse interface is predicted and metastable and unstable phases can be separated, at the heart of the notion of spinodal decomposition. Spinodal decomposition is a phase separation mechanism between two coexisting liquids (or glasses) and it occurs when there is no barrier for nucleation. However, initiating stochastic nucleation is prohibitively time consuming and requires introduction of a complex Langevin noise term or supercritical nuclei into the simulation.

Pathway for Nucleation and Order Parameter

One shortcoming of the CNT is that the nucleus has the same thermodynamic surface and volume properties as those of the macroscopic crystal. A direct consequence of this condition is that the nucleus properties do not depend on its size (Fig. 4.9), which can be written as

$$\Delta G_V = \Delta G_{V\infty} \tag{4.18}$$

with ΔG_V and $\Delta G_{V\infty}$ the thermodynamic driving force for a nucleus and for the macroscopic crystal, respectively.

The CNT nucleus emerges due to density (or concentration) fluctuations, whose free energy depends on its spatial extension (large extension for a spinodal decomposition, for instance) and its amplitude $\Delta\rho$ (lower free volume compared to the initial glass as the disorder is reduced in the newly formed phase). The CNT condition to form a nucleus can be written as $\rho_{glass} + \Delta\rho \geq \rho_{new}$, with ρ_{new} the density of the macroscopic phase. There is thus a single order parameter (the density) implied in the CNT or, alternatively, we must consider that all parameters evolve simultaneously [4.52].

However, in reality, the nucleus can undergo changes in composition and/or structure before reaching the final macroscopic phase. This implies possible intermediate phases, as proposed by Ostwald's rule of stages (Sect. 4.2.1, *Ostwald's Rule*), and also implies consideration of at least two order parameters to be able to distinguish two phases, e. g., density and structure. If the two order parameters are not evolving simultaneously, a correct evolution of the system cannot be obtained by the CNT. Therefore, the theory fails to capture the dynamics of the nucleation process [4.31]. It is thus essential to take into account within the theory the pathways leading to the nucleation of the final phase, which are not always easily accessible by experimental observation. Recently, two theories have emerged extending the concepts involved in the CNT and con-

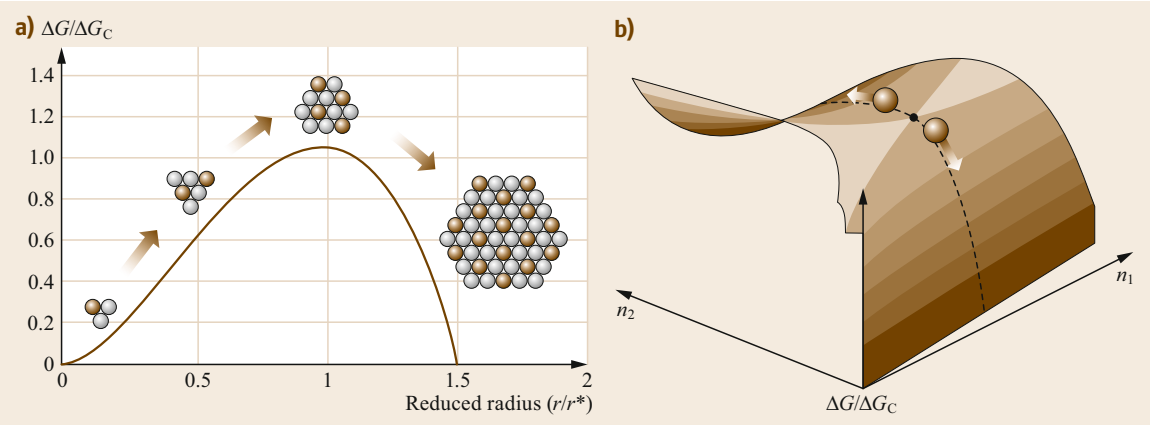

Fig. 4.9 **(a)** Schematic representation of the evolution of a CNT cluster. The critical radius r^* is obtained with (4.6) and the energy barrier is overcome by fluctuations. **(b)** An alternative illustration is that the nucleus passes through the ridge in a thermodynamic potential surface. After [4.51]. © 2008, with permission from Elsevier

sidering the evolution of the nucleus in more than one dimension (not only its size): the generalized Gibbs approach and the two-step model.

The Generalized Gibbs Approach (GGA)

In this theoretical approach which was developed in several papers [4.42, 53, 54], the evolution of the nucleus during the crystallization process is taken into account, as the nucleus properties can change with its size, by introducing the dependence of the thermodynamic and kinetic parameters determining the nucleus growth. In the GGA, the critical parameters (radius, work of formation) depend on nucleus composition. A critical nucleus is then specified by the maximum of W with respect to the cluster size and by the minimum of W with respect to variations of the cluster composition. Therefore, W can be represented in a 2-D-plot depending on two variables n_1 and n_2 representing the size and the composition, which are required to specify the state of the nucleus (Fig. 4.9b). In this thermodynamic potential surface representation, the evolution of the nucleus can be followed and it is then possible to identify the most probable pathways for nucleation.

Because of its composition dependence, the critical work of formation determined by the GGA is reduced compared to that predicted by the CNT (Fig. 4.10). The nucleation rate is also lower than CNT, improving some shortcomings from the classical theory. Indeed, the nucleus follows a path through the point of lowest energy in the GGA (saddle point, black curve in Fig. 4.10b), which is usually not the case in the CNT (white curve in Fig. 4.10b).

As the state of the evolving nucleus can be followed as a function of size and composition, a better understanding of the nucleation mechanism can be proposed. The nucleus first evolves in size, retaining a composition close to that of the initial liquid (Fig.4.10a). Once the characteristic size r^* is achieved, the composition changes significantly, whilst size is kept almost constant. Finally, when the composition of the macroscopic phase is reached, the nucleus grows in size with constant composition. Major differences are present in this scenario compared to the CNT. In this latter case, there is a continuous increase in nucleus size with essentially the same composition and structure as the macroscopic final phase (Fig. 4.9a). The thermodynamic barrier is overcome by a change in size. Conversely, in the GGA, a change in composition is required to surmount the energy barrier. The critical size is close to the characteristic size r^* but not necessarily equal.

Another important aspect of this theory, and in agreement with van der Waals–Cahn and Hilliard and alternative DFT approaches, is that the spinodal decomposition can be taken into account and, for instance, the work of formation tends to zero for values of the initial supersaturation approaching the spinodal curve [4.55].

The diffusion coefficients can also affect the pathways for the formation of clusters of the new phase (kinetic assumptions of the CNT). This has been studied in a binary system by varying the partial diffusion coefficients [4.56]. In all cases, the evolution proceeds via the saddle point, but the trajectory can be significantly different, with an increase or decrease of the size of the nucleus during the compositional change (Fig. 4.11).

Such a model has limited applications for glass-ceramics used in industry, which are often chemically and structurally complex and for which the required param-

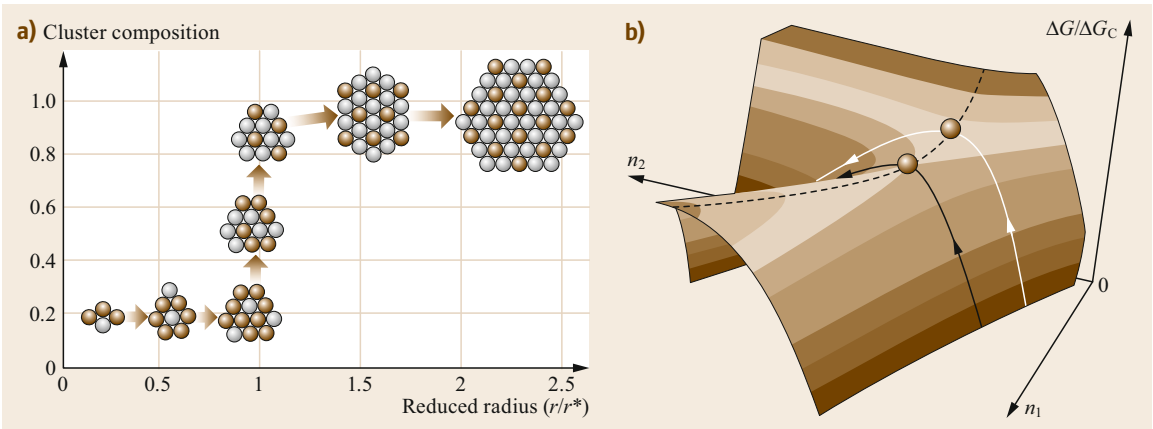

Fig. 4.10 **(a)** Schematic representation of the evolution of a cluster as predicted by the GGA resulting from a change in size and composition. **(b)** Work of formation of the critical nucleus. In the CNT, the pathway goes through a ridge (*white*) for which W^* is overestimated compared with the pathway via a saddle point (*black*) as predicted by the GGA. After [4.51]. © 2008, with permission from Elsevier

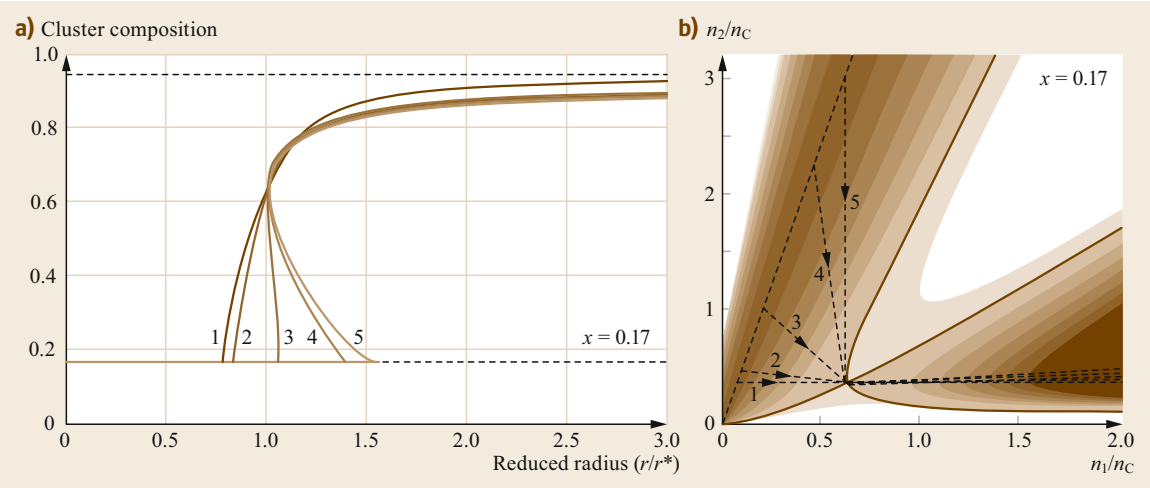

Fig. 4.11a,b Different trajectories for cluster evolution as a function of the ratio of the diffusion coefficients in a binary system: $D_1/D_2 : D_1/D_2 \to 0$ (1), $D_1/D_2 = 0.1$ (2), $D_1/D_2 = 1$ (3), $D_1/D_2 = 10$ (4), $D_1/D_2 \to \infty$ (5). **(a)** Evolution of the cluster as a function of its size and composition. **(b)** Alternative representation in the thermodynamic potential surface projection. Reprinted from [4.56] with the permission of AIP Publishing

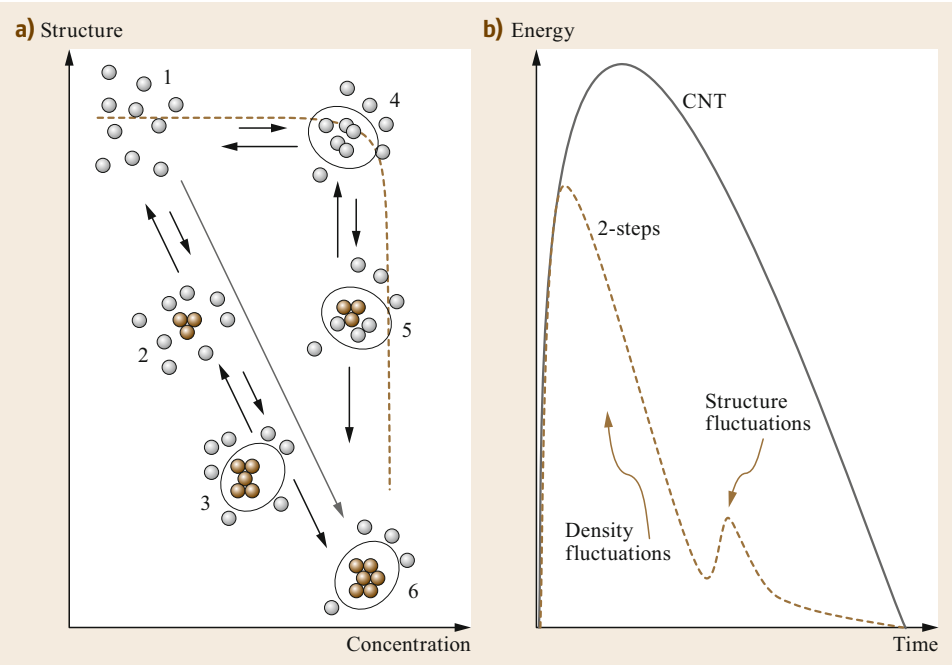

Fig. 4.12 **(a)** Nucleation scenarios for the CNT and two-step model (after [4.43]). **(b)** Two free-energy barriers in the two-stage model which are both lower and easier to cross than the single barrier in the CNT (after [4.57])

eters (diffusion coefficients, surface energy, etc.) are not available.

The Two-Step Model

Contrary to the GGA model which has a strong theoretical basis, the two-step model reflects mainly experimental observations and simulations, especially on colloidal or molecular systems where in situ characterization techniques are possible [4.43, 52, 57–63]. In the case of CNT, from an initial homogeneous liquid (step 1 in Fig. 4.12), a subcritical nucleus (step 2 in Fig. 4.12) is formed by aggregation of structural entities until the size of a critical nucleus is reached (step 3 in Fig. 4.12). Both subcritical and critical nuclei have exactly the structure of the final crystal (step 6 in Fig. 4.12). In the two-step model, the first step corresponds to the forma-

tion, in the supercooled liquid, of a denser disordered phase (step 4 in Fig. 4.12), either by liquid–liquid separation or by critical density fluctuations. In the second step, the high density in the droplets favors structural ordering (step 5 in Fig. 4.12) and crystals are formed. There is thus a temporal decoupling between the two order parameters that describe nucleation, density, and structure.

The liquid–liquid (L–L) separation curve has a strong influence on the nucleation pathways and on the decorrelation between density and structure fluctuations [4.62]. When the free energy of the system is greater than that of the dense liquid phase (below the L–L curve, Fig. 4.13), the latter is stable relative to the initial liquid but metastable in comparison with the crystal. Close to the maximum temperature of the liquid–liquid (L–L) phase separation (highest temperature in the immiscible region), the decorrelation between the two order parameters is at maximum and density fluctuations with large amplitude are favored. Conversely, when the free energy of the initial liquid is less than that of the dense liquid (above the L–L curve, Fig. 4.13), the dense phase is metastable relative to both the initial liquid phase and the final crystalline phase. Above the L–L curve, the two fluctuations occur almost simultaneously, following CNT, since the lifetime of the dense phase is limited.

The experimental observations at the basis of this two-step model have been strengthened by numerical calculations based on DFT [4.57]. Different stages corresponding to densifying and structuring are shown to be free-energetically easier than crossing a single barrier as assumed by the CNT (Fig. 4.12b). Each step in the two-step mechanisms has a low energy barrier so that this process is favored compared to CNT and gives a larger nucleation rate, in agreement with experiments.

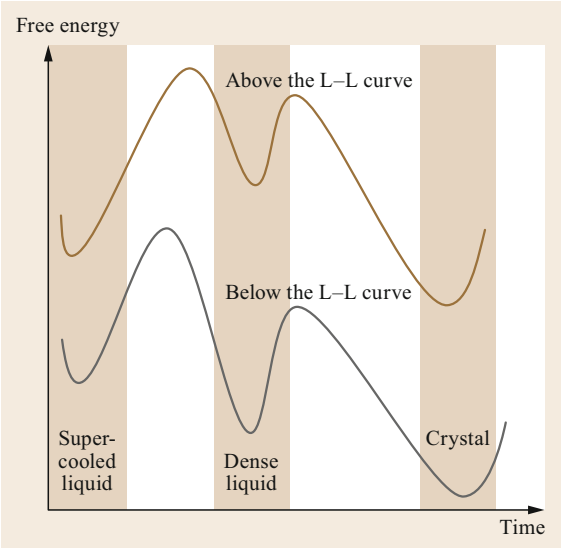

Fig. 4.13 Diagram representing the free energy according to two different scenarios of nucleation considering that the initial liquid phase is above or below the liquid–liquid separation curve. The crystal appears after structural reorganization following these density fluctuations (after [4.52])

It should be noted that all these nonclassical scenarios (especially two-step model, GGA) are based on the consideration of an intermediate metastable phase, consistent with Ostwald's rule of stages and they support the fact that a detailed understanding of nucleation mechanisms requires following the possible pathways of nucleation. Such observations, using advanced experimental and computational tools, are becoming increasingly available, even for multicomponent glass-ceramics [4.32].

4.3 Design of Glass-Ceramics

The specific physical properties of a glass-ceramic material are usually dominated by the composition and the microstructure of the crystalline phases embedded in the glass matrix. It is thus of primary importance to understand the nucleation and growth processes taking place during crystallization in order to further control the size, morphology, distribution, and nature of the present crystalline phases. Therefore, designing mechanical, thermal, optical, esthetic, medical, and/or bioactive properties in a glass-ceramic material requires precise control of the elaboration process to develop the desired microstructure.

Usually, a glass-ceramic material is elaborated following a three-step process:

- Choice of the parent glass composition, in order to obtain the desired crystalline phase.
- Synthesis of the glass via a melting process (possibly followed by quenching) and shaping (molding).
- Controlled crystallization of the glass. The crystallization heat treatment is determined depending on the crystallization mechanism taking place and the desired microstructure.

4.3.1 Composition of Glass-Ceramic Systems

Choice of the Parent Glass Composition

The choice of the parent glass composition is an important step in the design of a glass-ceramic material. The composition must first undergo glass formation, and thus contain glass-forming elements. Moreover, the composition will also determine the nature of the future crystalline phase(s), of the nucleation and growth mechanism that will be taking place, and of both the thermodynamic and the kinetics, of the studied system. With each composition leading to different specificities and physical properties (Sect. 4.5), it is currently very complex to predict a priori the physical properties associated with a given composition.

The extent of possible composition domains for glass-ceramic materials is very large. With the most significant constraint being the ability to first form a glass, conceivable glass-ceramic compositions therefore correspond to the almost-infinite number of glass-forming compositions. Although the first-reported glass-ceramic materials were based on (alkaline and alkaline-earth) silicate or aluminosilicate compositions, these have progressively become more diverse and complex and have now been extended to different glass-forming compositions (phosphates, germanates) and incorporate increasing contents of numerous glass modifiers (metals, transition metals, lanthanides, ...) thanks to the improvement of glass elaboration processes and to the need to develop specific properties. For example, fluoride and chalcogenide compositions have been developed in order to obtain materials exhibiting transparency within the infrared range (Sect. 4.5.3, *Non-Oxide Transparent Glass-Ceramics*).

Nucleating Agents

The use of nucleating agents is an interesting approach largely employed by the industry to initiate heterogeneous nucleation within the whole glass volume, so as to induce a crystallization process that can be more easily controlled compared to a homogenous crystallization or a surface crystallization mechanism [4.64–66]. Nucleating agents, first employed by S.D. Stookey when he performed crystallization of lithium silicate glass using silver particles, are most often composed of either metal elements dispersed as colloids (Au, Ag, Pt, Pd, etc.) or simple oxides (TiO_2, ZrO_2, P_2O_5, Ta_2O_5, WO_3, MoO_3, etc.) which are added to the original glass composition. The amount of nucleating agents required to perform efficient volume crystallization can vary widely from one system to another. It is typically from 2 to 8 mol% for oxides and below 1 mol% for colloids. This addition enables a strong nucleation rate to take place (up to $10^6\,\mu m^{-3}$), which can subsequently be coupled to controlled crystal growth in order to develop innovative or enhanced optical and mechanical properties. For example, in the case of the low thermal expansion coefficient LAS glass-ceramics widely used in cooktops, homogeneous nucleation is not sufficient to generate the strong nanocrystallization required for the desired thermomechanical and transparency properties of the final product [4.67]. To achieve such prerequisites, heterogeneous nucleation is used via enrichment of the initial glass compositions with $ZrTiO_4$ [4.68–70]. An optimized two-step crystallization process then allows numerous β-quartz nanocrystals to be obtained, ensuring the thermomechanical properties as well as transparency of the LAS glass-ceramics (Sect. 4.5.1). The crystallization process induced by the use of nucleating agents is relatively complex. Two recent studies by T. Höche and C. Patzig, relying on advanced transmission electron microscopy experiments, enabled light to be shed on these complex mechanisms.

In their first study, the authors reported the crystallization of a quartz solid solution from a $51.9SiO_2$-$21.2MgO$-$21.2Al_2O_3$-$5.7ZrO_2$ (in mol%) parent glass and revealed the temporal evolution of the volume crystallization [4.71]. Upon analyses of samples heat-treated for different soaking times, different steps of crystallization were observed. Using electron diffraction, a growth model with special emphasis on the early stages of volume crystallization was developed (Fig. 4.14).

From their observations, the authors could propose that starting from the base glass with homogeneous distribution of the raw material, star-shaped single-crystalline ZrO_2 is precipitated (Fig. 4.14a,e). With ongoing dwell time during annealing, those ZrO_2 crystals increase in size, thereby soaking up zirconium from the surrounding glass matrix, forming a zirconium depletion zone around the crystals (Fig. 4.14b,f). This local change in elemental distribution is believed to foster the crystallization of the surrounding glass matrix. Starting at either the star-shaped ZrO_2 crystal itself or within the surrounding, Zr-depleted zone, a high-quartz solid solution starts to expand isotropically into the sample volume (Fig. 4.14c,g). Both the decrease of the Zr concentration in the vicinity of the star-shaped ZrO_2 crystal with ongoing annealing time and the crystallization of the high-quartz solid solution around it constrain and stop the growth of the star-shaped ZrO_2 crystals after a certain progression of the overall crystallization process. Meanwhile, the expanding solid solution domain expels Zr in the form of small, circular ZrO_2 precipitates that become embedded in the solid-solution domains (Fig. 4.14d,f). The domain expansion progresses until the growth fronts of adjacent domains touch each

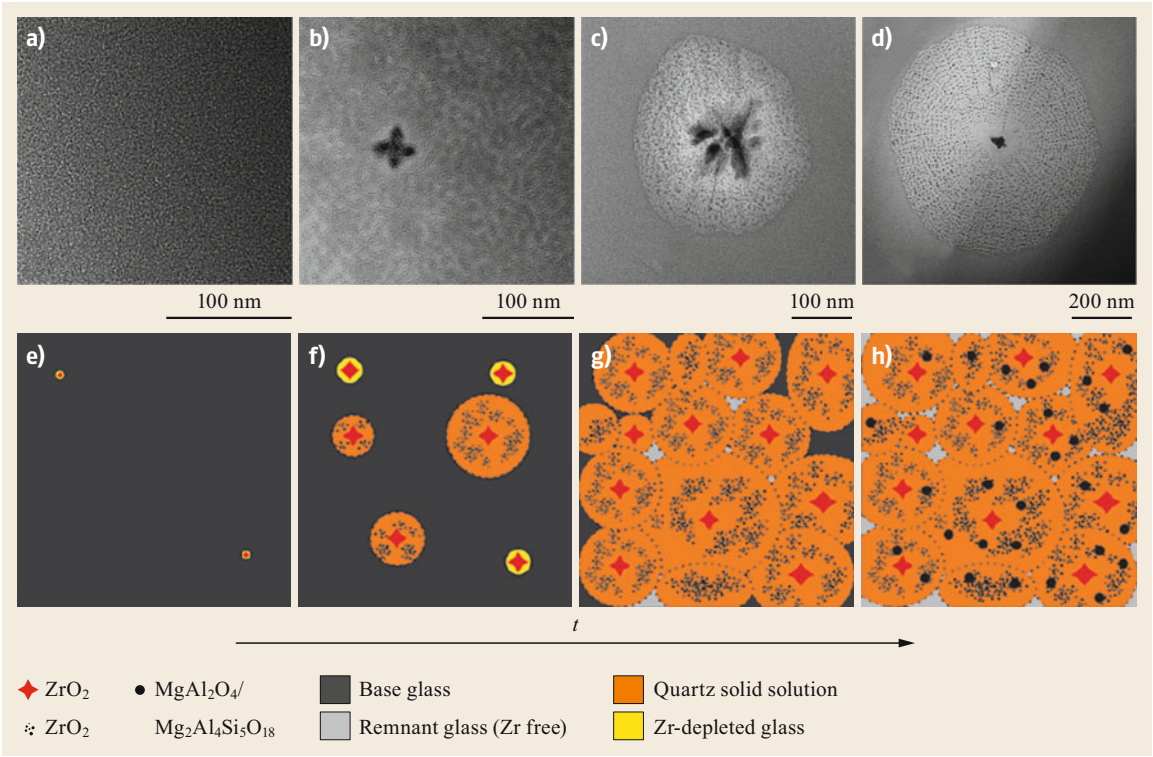

Fig. 4.14a–h Quartz crystallization from a $51.9SiO_2$-$21.2MgO$-$21.2Al_2O_3$-$5.7ZrO_2$ glass (in mol%). (*Top*) Bright-field transmission electron microscopy (TEM) micrographs of samples at different annealing stages: **(a)** base glass, **(b)** 0 h (ramp-up only), **(c)** 15 min, **(d)** 30 min. (*Bottom*) Proposed model of the temporal evolution of volume crystallization with increasing dwell time **(e–h)**. Reprinted with permission from [4.70]. © 2012 American Chemical Society [4.71]

other, thus forming domain boundaries where again ZrO_2 is expelled. In-between the domain boundaries, remnant, noncrystallized glass might persist. From the latter, Zr is probably diffusing to the already existing ZrO_2 crystals at the domain boundaries, giving them an elongated shape, and gradually turning the remnant glass Zr-free. With increasing dwell time, Mg and Al are depleted from the high-quartz solid solution and initially form indialite ($Mg_2Al_4Si_5O_{18}$) and later spinel ($MgAl_2O_4$). This process destabilizes the high-quartz solid solution by discharging MgO and Al_2O_3, thus enabling the phase transformation into the low-temperature quartz modification to occur upon cooling [4.71].

In subsequent studies, the same authors investigated the role of zirconia and titania used as nucleation agents in a lithia aluminosilicate glass (Fig. 4.15) [4.72, 73]. They first reported the precipitation of $ZrTiO_4$ nanocrystals accompanied by the formation of a circumjacent diffusion barrier consisting of alumina. Then they studied the temporal evolution of the alumina barrier and the size distributions of $ZrTiO_4$ nanocrystals and lithia aluminosilicate high-quartz solid solution crystals promoted by the nucleation agent. They reported that alumina gets expelled from former amorphous, titania, zirconia, and alumina containing phase separation droplets. Consequently, an alumina-enriched layer is formed around the $ZrTiO_4$ nanocrystals crystallized from the droplets. Monitoring the temporal evolution of alumina-enriched diffusion barriers shows first an increase in alumina concentrations within the first few hours of heat treatment and then a drop down for longer heat-treatment times when growth of the $Li_2Al_2Si_3O_{10}$ solid-solution crystals is completed. On the basis of these experimental results, a novel nucleation mechanism, namely diffusive nucleation (nucleation in the decomposing alumina gradient around former phase-separation droplets, perhaps supported by internal strain) was proposed (Fig. 4.15).

These detailed examples demonstrate the complexity of the crystallization mechanisms involving nucleating agents. Their use is far from being predictable and universal. In fact, crystallization induced by nucleating agents has only been developed in a few limited examples. Therefore, different crystallization mecha-

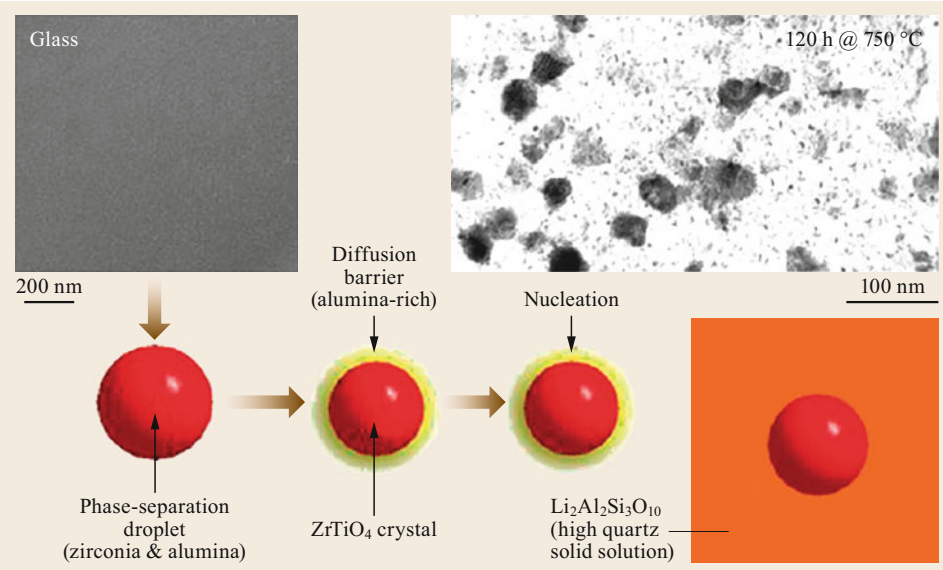

Fig. 4.15 Schematic representation of the microstructure evolution in Li-Al-Si glass-ceramics illustrating the action of nucleating agents. Adapted with permission from [4.73]. © 2012 American Chemical Society

nisms have to be taken into account to perform volume nucleation.

Phase-Separated Glasses

Crystallization from a phase-separated glass is the other major crystallization mechanism inducing volume crystallization from nonhomogeneous nucleation. The choice of an adequate nominal glass composition [4.65, 66, 74] or a glass composition modified by the addition of a phase-separation-initiating agent (fluoride [4.75], phosphate [4.76], etc.) can lead to a phase-separated glass that will favor an important heterogeneous but volume nucleation. A famous example of this mechanism is the elaboration of transparent mullite glass-ceramics obtained from Al_2O_3-SiO_2 glass crystallization [4.77]. The phase-separation type can either be nucleation/growth or spinodal (Fig. 4.16). During the crystallization process, the size of the crystals will be limited by the size of the phase-separated domains (at least until a coalescence effect takes place). As the size of the phase-separated domains depend on both glass composition and glass synthesis conditions, the size of the crystals in the subsequent glass-ceramics can be controlled.

Phase-separated zinc gallogermanate and zinc gallosilicate glasses provide a clear illustration of this ability. ZnO-Ga_2O_3-GeO_2-Na_2O glasses exhibit nucleation/growth nanoscale phase separation, in the form of droplets well separated from the germanate matrix. The size of the nanostructures can be tailored depending on the nominal glass composition (Fig. 4.17). A single heat treatment then allows se-

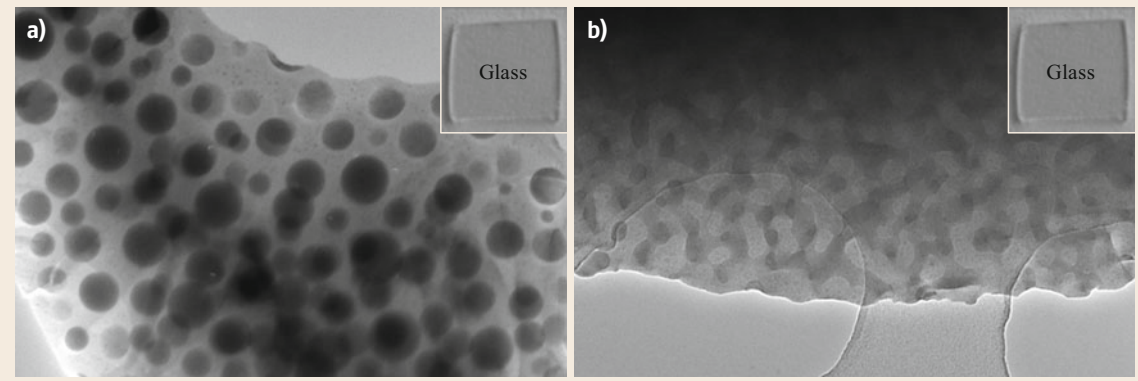

Fig. 4.16a,b TEM patterns of nanoscale phase-separated glasses: **(a)** nucleation and growth phase separation type and **(b)** spinodal phase separation type

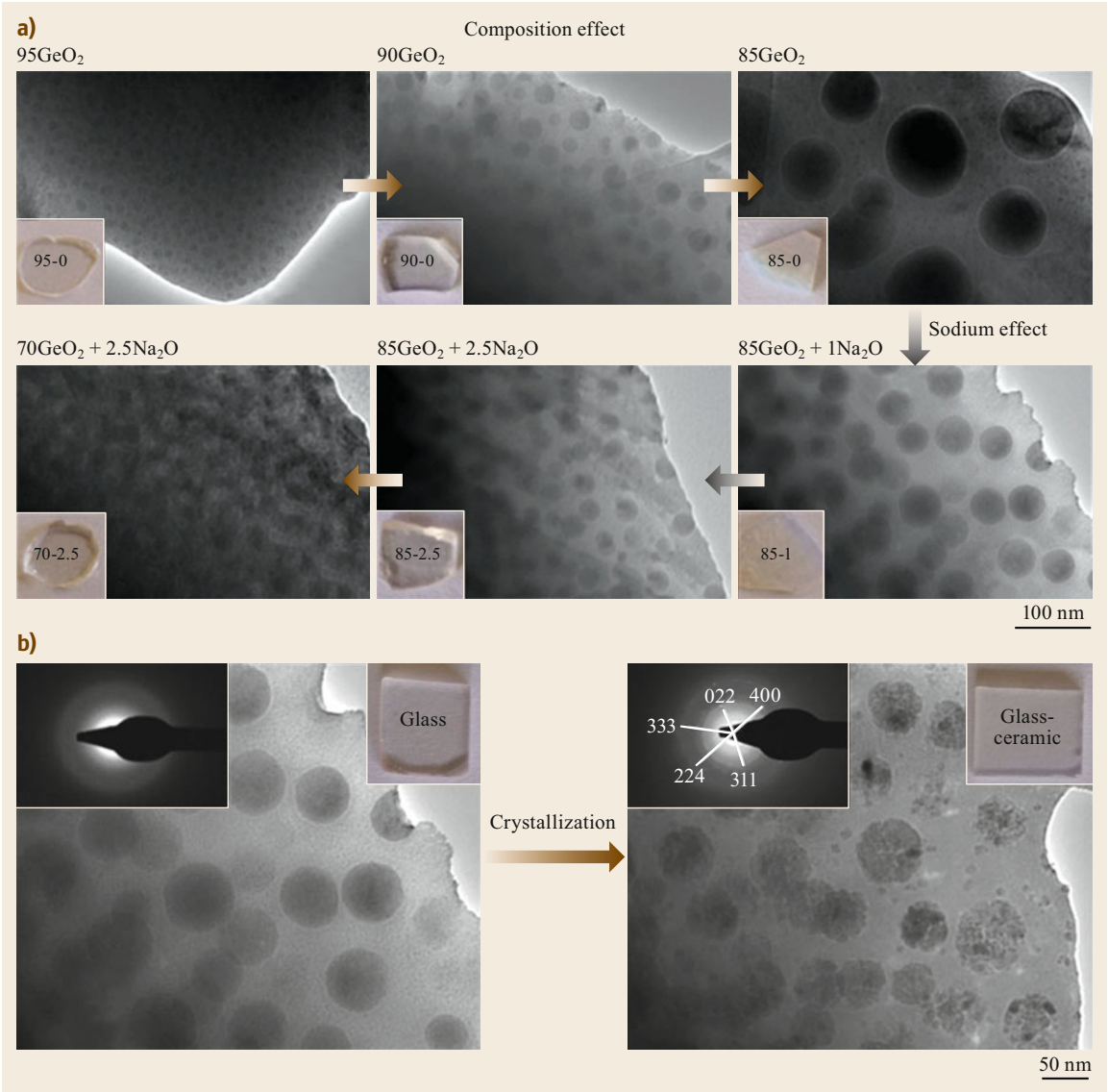

Fig. 4.17 (**a**) TEM patterns of representative samples of the $(100-x)GeO_2$-$xZnO$-xGa_2O_3 $(+zNa_2O)$ glass series with their corresponding photograph presented in the *inset*. (**b**) TEM patterns showing the nanostructure evolution during crystallization. Reprinted with permission from [4.78]

lective crystallization of the sole glass phase corresponding to the droplets. As the crystal growth is limited by the size of the initial phase separation, the resulting glass-ceramic materials exhibit nanostructures and transparency properties similar to the parent glass.

ZnO-Ga_2O_3-SiO_2-Na_2O glass compositions exhibit nanoscale spinodal phase separation. An original mechanism relying on cationic diffusion has been proposed to explain the crystallization process occurring in a spinodal phase-separated glass (Fig. 4.18) [4.79]. To summarize, the crystallizing phase initially rich in Ga and Zn releases Ga and Si during spinel crystallization in order to reach the $ZnGa_2O_4$ composition ($Ga/Zn = 2$). As a consequence, the glass matrix is enriched in Si, whereas the Ga excess leads to the formation of glassy Ga-Si droplets. At high temperature, coalescence of the crystals occurs, leading to transparency loss when the crystals reach a critical size (above 70 nm for the largest ones).

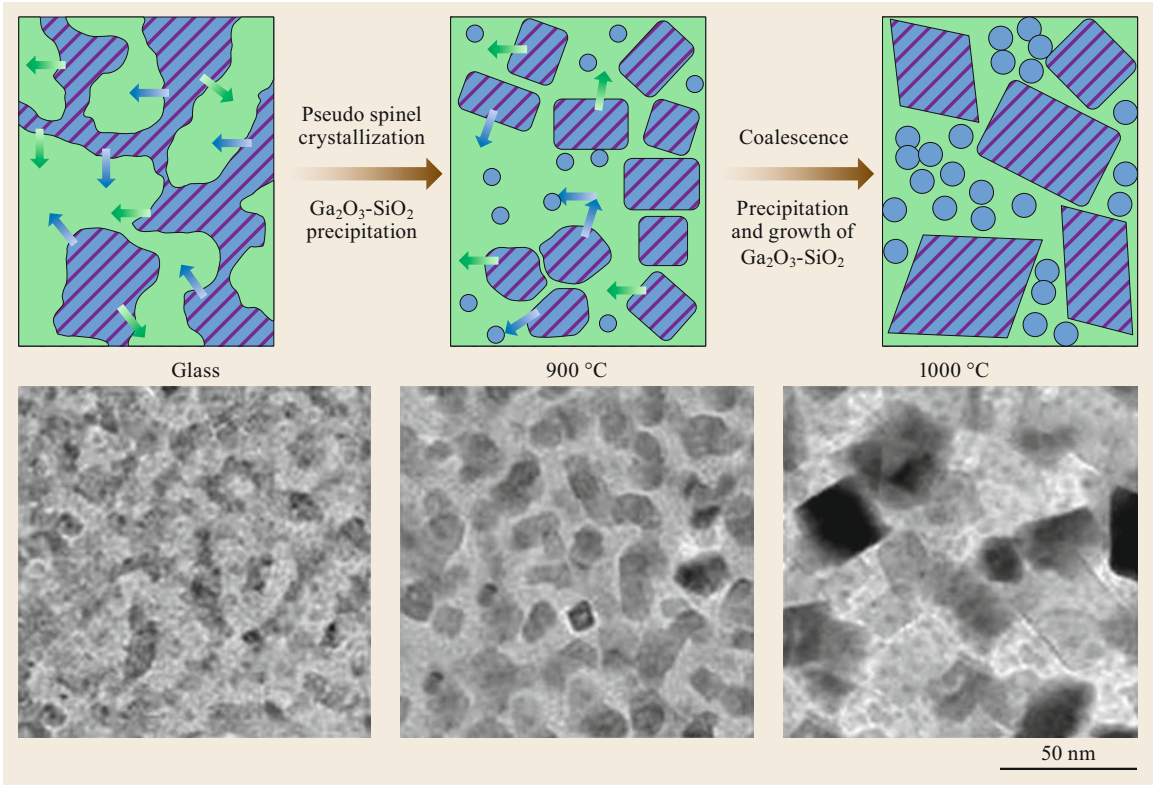

Fig. 4.18 Scheme of the $ZnGa_2O_4$ nanocrystallization mechanisms in a phase-separated silicate glass during heat treatment (the *green area* represents the glassy matrix and the *blue/red striped area* the crystallizing phase). *Arrows* represent diffusion mechanisms (*green* for Si and *blue* for Ga). The experimental TEM images corresponding to each scheme are presented below. Adapted from [4.79] with permission of The Royal Society of Chemistry

4.3.2 Glass-Ceramic Elaboration Processes

Glass Synthesis

The classic glass synthesis process is based on a melt-quenching process of powder precursors. The choice of precursors can be of great importance in order to tightly control the quality of the glass to be formed. For example, oxide, carbonate, or nitrate precursors will each have a different influence on the decomposition rate and process when heating up to the melt. Fining agents such as alkaline oxides can be used too, especially in order to lower viscosity and avoid the presence of bubbles in the final glass (see Chaps. 34 and 35). Nucleating agents or phase-separation-initiating agents can also be used in order to favor volume nucleation (Sect. 4.3.1). Thus, the precursors are weighted in appropriate amounts and mixed together before being heated up to the melting temperature of the mixture. The temperature and the duration of the fining step are also key parameters in order to optimize the homogeneity of the glass and to avoid volatilization effects and eliminate any remaining bubbles. Depending on the composition, the melt is then either slowly cooled down to room temperature or quickly quenched by pouring the crucible in water for example. In this last case, a subsequent annealing treatment performed at a temperature slightly below T_g will be necessary in order to relax internal constraints and improve mechanical properties.

Glass formation of refractory compositions is not feasible via a classic melting process because of the high temperature that must be accessed to homogeneously melt the precursors and/or the high quenching rate required to avoid unwanted crystallization during cooling (devitrification). Different specific glass synthesis processes have been developed to overcome these limitations. A few examples are given below to illustrate these possibilities:

- The sol–gel method is an alternative amorphous material preparation method which enables powder or bulk glassy precursors to be elaborated [4.80–82]. This synthesis process is especially interesting for refractory compositions for which glass formation

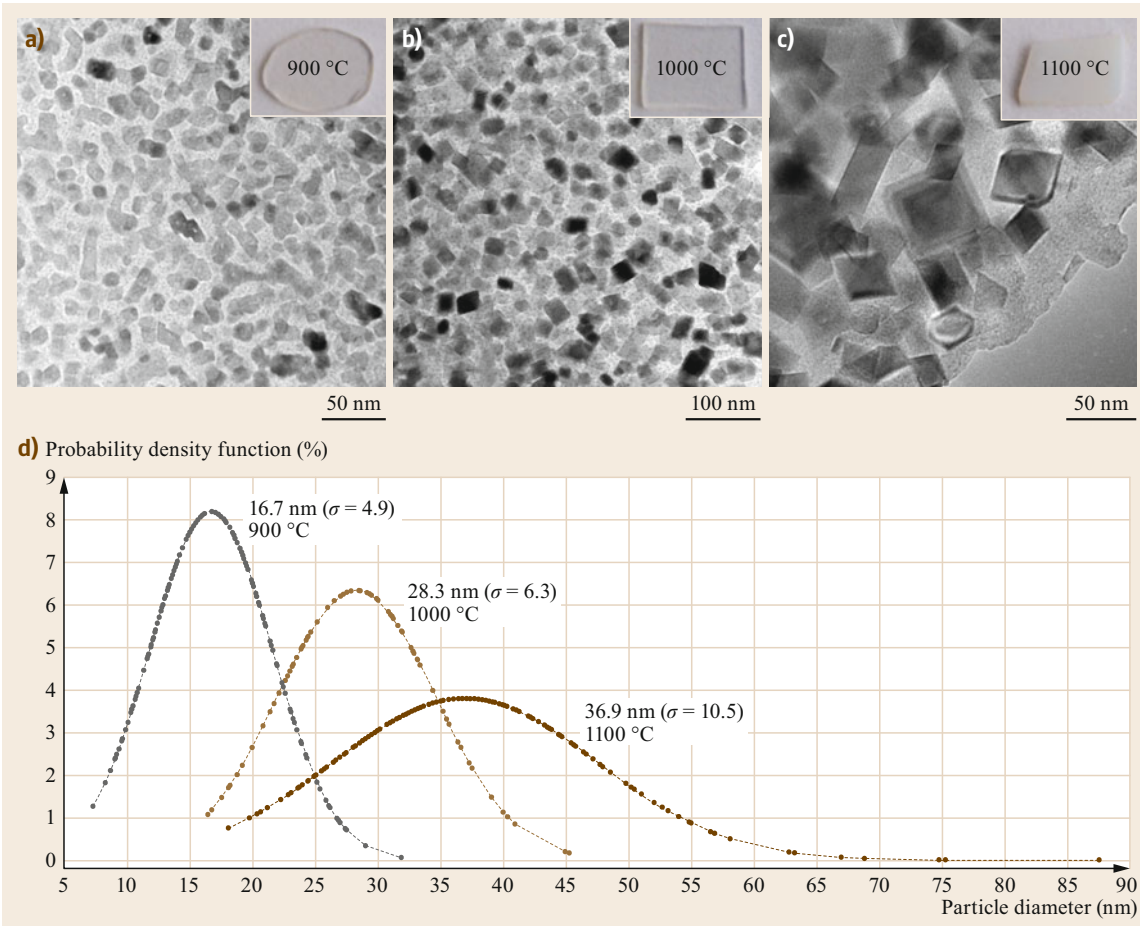

Fig. 4.19a–d Bright-field TEM images of the $55SiO_2$-$5Na_2O$-$17ZnO$-$23Ga_2O_3$ glass-ceramic materials heated via a single heat treatment at **(a)** 900 °C, **(b)** 1000 °C, and **(c)** 1100 °C. **(d)** Evolution of the size distribution with standard deviation(s) of the corresponding $ZnGa_2O_4$ crystals. The presence of nanoparticles larger than about 70 nm leads to transparency loss. Adapted from [4.79] with permission of The Royal Society of Chemistry

is hardly achievable using a classic method. However, the costly raw materials and slow synthesis process restrain the use of this technique.

- The plasma spraying elaboration process consists in introducing raw powder precursors into a very-high-temperature ionized gas flux. The resulting melted particles are then projected onto a recovery substrate. This technique can be applied to a large panel of materials, in particular refractory compositions. However, although it is possible to obtain a bulk material by sintering the powder obtained [4.83], most of the applications are limited to coating processes [4.84].
- The spray pyrolysis method is relatively similar to the previous process. The precursors are first dispersed in a liquid before being sprayed into a high temperature gas flux. After quenching, the glass powder sample is then recovered. However, the small synthesized volume of this process often restrains the number of applications.

Crystallization Processes

Classic Crystallization by Thermal Treatment. Theoretical nucleation and growth processes have been detailed previously in Sect. 4.2. From a practical point of view, heterogeneous nucleation that takes place uniformly in the volume of the material is the foreseen mechanism for most commercial glass-ceramics. This is especially the case for glass compositions enriched in nucleating agents and phase-separated systems (see Sect. 4.5 for greater detail). In addition to crystallization of the intended phase, the crystallization process generally aims for strong nucleation and limited crystalline growth in order to develop a microstructure showing

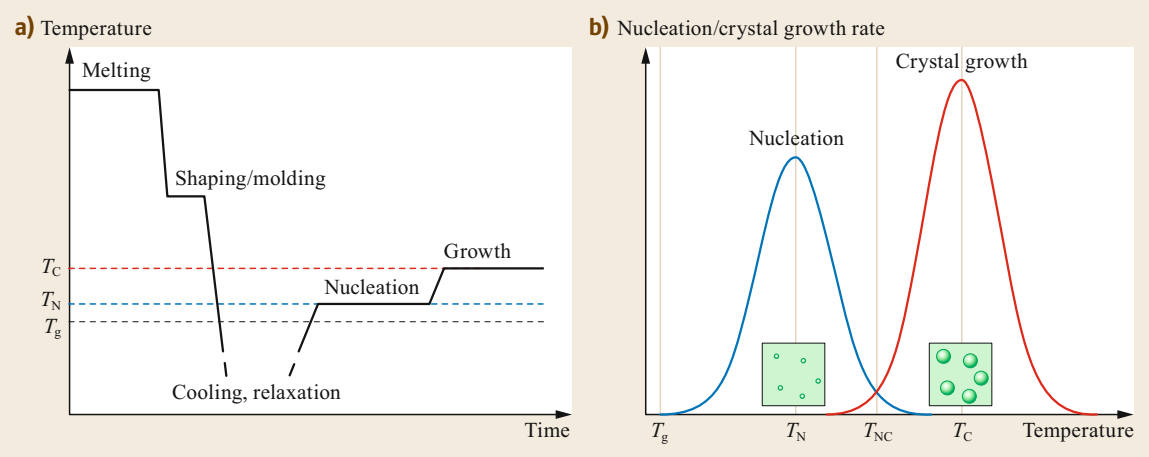

Fig. 4.20a,b Classic glass-ceramic elaboration process. **(a)** Glass crystallization is composed of two steps in which characteristic temperatures are determined from **(b)**. **(b)** Classic evolution of nucleation and crystal growth rates as a function of temperature

numerous small-size crystals, so as to develop glass-ceramic materials with targeted optical or mechanical properties. The choice of both the temperature and the duration of the crystallization step is then of primary importance (Fig. 4.19).

In regard to the information obtained from thermal analysis (Sect. 4.4.1, *Thermal Analysis*), the optimized temperature and duration of the crystallization thermal treatment may be determined, depending on the desired crystalline rate. Usually, the nucleation step determines the number of nucleation centers whereas the crystal growth step governs the size of the crystals embedded in the glass matrix (Sect. 4.2.2). The crystallization rate of the final glass-ceramic thus depends on the coupled effect of nucleation and crystalline growth steps.

A classic crystallization treatment is composed of two steps (Fig. 4.20):

- The first step corresponds to nucleation and is performed around T_N, corresponding to the maximum nucleation rate (T_N is usually slightly above T_g).
- The second step, the crystal growth step, is performed at higher temperature, around T_C which corresponds to the maximum crystal growth rate.

This two-step process is especially interesting when a strong crystallization rate is foreseen (numerous and large crystals). Conversely, if a maximum of nanometer-scale crystals is desired, for example in order to obtain glass-ceramics with optical (i. e., transparency) and/or mechanical properties, the crystal growth step is then strongly restrained or even skipped.

In the particular case where the nucleation rate and crystal growth rate curves show a strong overlap in the temperature space, the crystallization process can be simplified into a unique thermal treatment then realized at T_{NC}, corresponding to the optimal nucleation/growth rate temperature.

Crystallization from Glass Powder Sintering. Crystallization from glass powder sintering, when performed in order to obtain a dense glass-ceramic, is mostly used in two cases. First, this is an interesting elaboration method when glass processing cannot provide a dense bulk material (for example glass obtained as a powder by spray or pyrolysis or as a gel by sol–gel synthesis). Second, powder sintering is often used to induce a pseudovolume crystallization process for systems showing heterogeneous surface nucleation. Actually, although many developed glass-ceramic materials rely on a volume nucleation process (which can be induced by heterogeneous nucleation from nucleating agents or phase-separation processes), some glass compositions only undergo surface crystallization. Famous examples are fresnoite ($Ba/Sr_2TiSi_2O_8$, see Fig. 4.21a,b) or the famous leucite ($KAlSi_2O_6$) glass-ceramic material exhibiting a high coefficient of thermal expansion coupled to mechanical and machinability properties adapted for biomedical applications (dentures) [4.85–88]. The surface crystallization mechanism is often the consequence of a large density difference between the glass and crystalline phases [4.89]. It has also been linked to glass compositions showing a reduced glass transition temperature ($T_{gr} = T_g/T_m$) higher than 0.58–0.60 (Sect. 4.2.1, *Examples of Homogeneous Nucleation*) [4.12].

To produce crystallization in a glass powder sintering process, the parent glass is first finely ground and

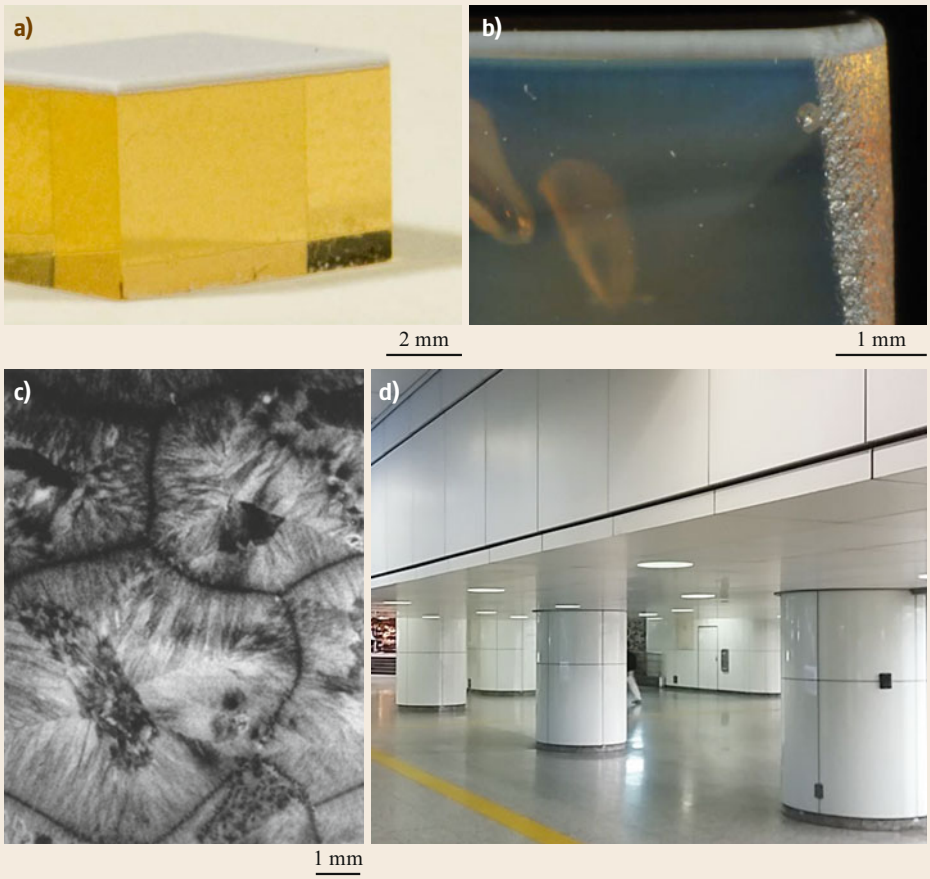

Fig. 4.21 (a,b) Photograph of dendritic growth of surface-crystallized $Sr_2TiSi_2O_8$ fresnoite. Reprinted from [4.92]. (c) Wollastonite ($CaSiO_3$) glass-ceramic microstructure obtained after glass powder sintering. Reprinted with permission from [4.93]. (d) Example of application of glass-ceramic as a building material

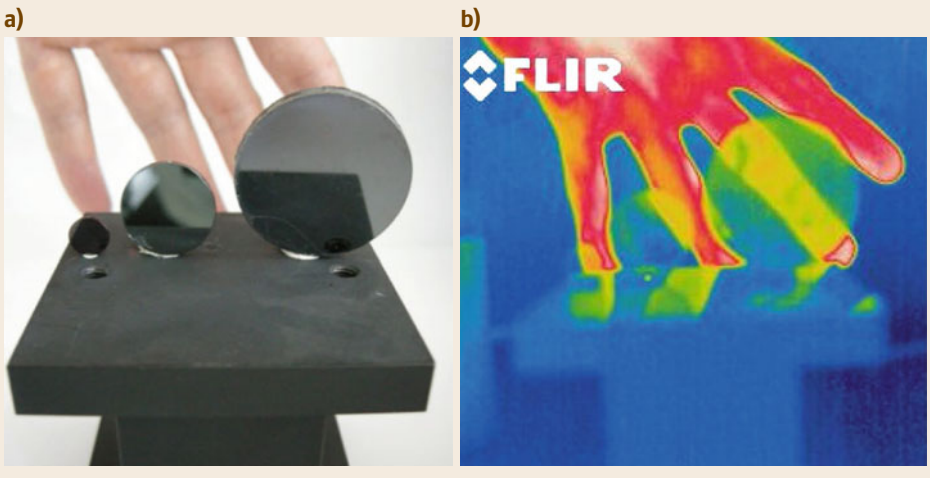

Fig. 4.22 (a) Visible and (b) infrared images showing infrared transmission of $80GeSe_2$-$20Ga_2Se_3$ glass-ceramics prepared by mechanosynthesis and spark plasma sintering, reprinted with permission from [4.94]

compacted by pressing. This step will enable a strong nucleation to take place during sintering as the numerous interfaces will act as nucleation centers. Surface crystallization is thus artificially transformed into volume crystallization. Glass powder sintering can require high pressure and high temperature conditions, in order to remove most of the porosity for mechanical or optical property purposes [4.90, 91]. A famous glass-

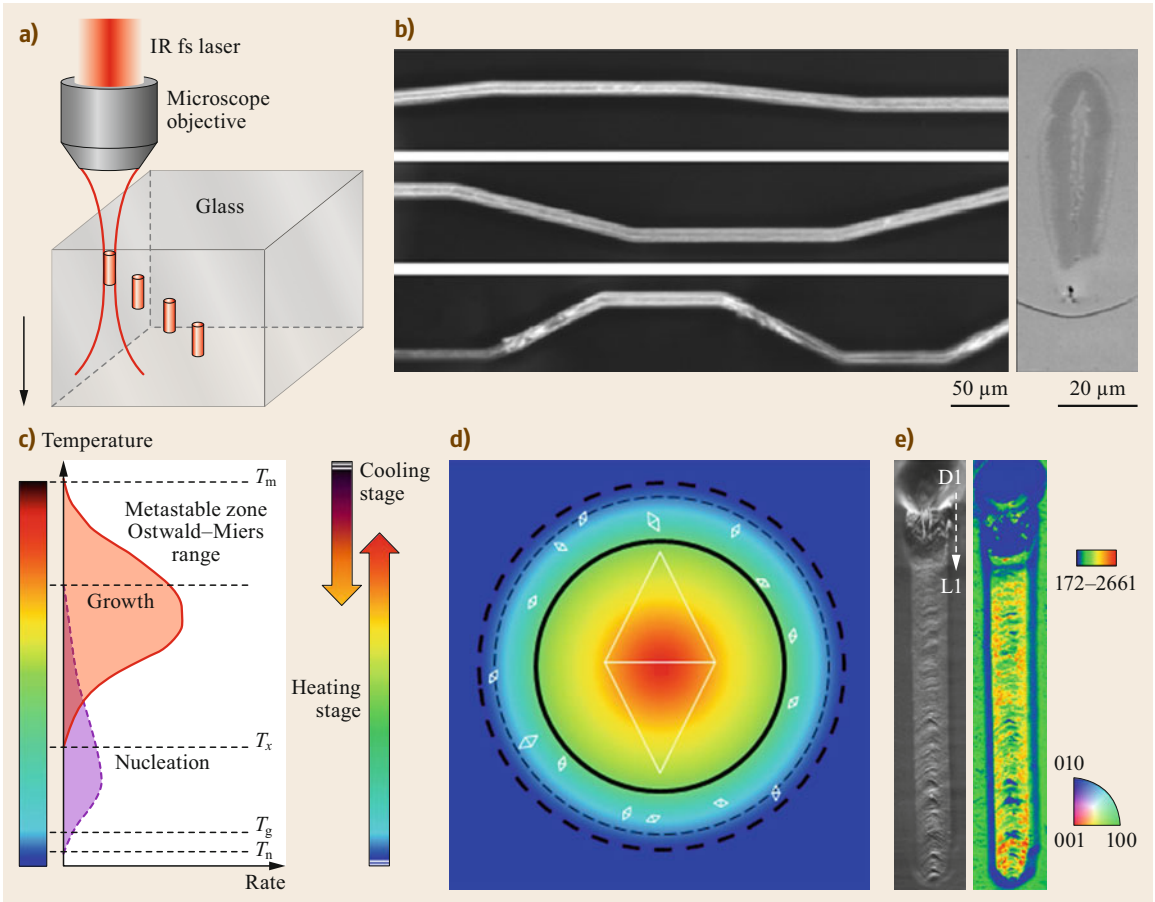

Fig. 4.23 **(a)** Scheme for the laser-induced crystallization process. **(b)** Optical microscopy image of crystalline lines of $LaBGeO_5$ induced by femtosecond laser irradiation in the same glass composition. **(c–e)** Sb_2S_3 single crystal growth in a Sb-S-I glass [4.95]. **(c)** Prototypical temperature dependence versus nucleation and growth rate curves. **(d)** Schematic of the CW-laser-induced temperature fields in the focal spot at the glass surface, with the temperature lines from **(c)** representing the lower limits of nucleation and crystal growth temperature range. **(e)** SEM (scanning electron microscopy) image and colored orientation inverse pole figure maps with reference vectors. Reprinted from [4.96]

ceramic material prepared from glass frit and nucleation occurring from the surface of the grains is Neoparies® manufactured by NEG. The main crystal phase is wollastonite and the mixture of frits of different colors enables a marbled appearance to be obtained for flat or curved panels (Fig. 4.21c,d).

It should also be noted that there are complex systems in which two distinct nucleation processes coexist, leading to the precipitation of two crystalline phases within the same glass-ceramic material [4.64]. For example, the elaboration of glass-ceramics by glass powder sintering with a microstructure imitating that of a natural tooth requires a double nucleation process: a leucite surface crystallization at the grain boundaries (on a powder sintered sample) and a volume apatite crystallization, initiated by a nanometer-scale phase separation. The controlled crystallization from the SiO_2-Al_2O_3-CaO-Na_2O-K_2O-P_2O_5-F glass powder thus enables one to obtain this excellent example of biomimicry (IPS d.sign®, Sect. 4.5.4).

Recently, an innovative approach to developing high-performing chalcogenide glasses and glass-ceramics transparent in the infrared range was reported by *Calvez* et al. (80$GeSe_2$-20Ga_2Se_3 system) [4.94]. The authors used precursor powder amorphization by mechanical grinding, so called mechanosynthesis, subsequently followed by spark plasma sintering (SPS) to prepare large bulk glass pieces unstable in terms of crystallization. These glasses can be crystallized to prepare dense bulk glass-ceramics without using a high-temperature melting step, which is a great achievement for chalcogenide compositions (Fig. 4.22).

Crystallization Induced by Laser Irradiation. Considerable efforts have been dedicated to the fabrication of glass-ceramic materials with oriented crystals which can exhibit anisotropic properties that are of interest for diverse dielectric, mechanical, or nonlinear optical applications (Sect. 4.5) [4.97–102]. It is usually necessary to apply external anisotropic constraints to induce oriented nucleation and growth processes. Several methods based on mechanical, kinetic, and thermodynamic effects as a function of an anisotropic external field have been applied with success, such as thermal gradient constraint, ultrasonic surface modification, thermal polarization (application of an electric field along with temperature treatment), electrochemically induced nucleation, laser irradiation, crystallization under a magnetic field, and even a combination of several of these methods [4.103].

Among these methods, crystallization induced by laser irradiation is a very promising approach. Even though the first reports on photoassisted nucleation were reported by *Stookey* in 1949 [4.104] (in such an approach crystal growth is often performed during annealing above T_g), [4.105, 106], proper laser crystallization is a very recent technique. It has seen tremendous development with the occurrence of new pulsed lasers delivering local electric fields in the range of those involved between nucleus and electrons in ions or atoms ($10^{10}\,\mathrm{V\,m^{-1}}$). Lasers with very short pulses (femtosecond lasers) induce multiphotonic localized absorptions, which initiate crystallization through thermal effects (Fig. 4.23a,b). Precise control of this deposited energy versus time and space enables one to control both the size and the localization of crystallization in glass (crystallization may occur during a further annealing process but can also take place during the irradiation process, without requiring further annealing) [4.107]. These possibilities open the way to the design of 3-D microstructured glass-ceramics [4.95, 108]. Among different nonlinear optical applications, frequency doubling is the main foreseen property. Nevertheless, these applications are currently limited by the crystal growth rate ($\approx 0.1\,\mathrm{mm\,s^{-1}}$). Recently, the possibility to grow single crystals via solid–solid transformation of a glass was reported by *Jain* et al. (Fig. 4.23c–e) [4.96]. The authors reported the crystallization of Sb_2S_3 single crystals in Sb-S-I glasses via an *all-solid-state glass into crystal* transformation. Extraneous nucleation is avoided relative to crystal growth via spatially localized laser heating and inclusion of a suitable glass former in the composition.

4.4 Structural Characterizations and Microstructures

4.4.1 Structural Characterization Techniques

Fine observation, quantification, and analysis of glass-ceramic formation and development require the use of a large range of complementary techniques at the interface between glass science and crystallography. Among these, thermal analysis, powder diffraction, optical and electron microscopies, and spectroscopic techniques are most commonly used. Depending on the nature of the required information (morphology, chemical composition, phase identification, qualitative or quantitative analysis, etc.) and the different constraints of the study (destructive or nondestructive analysis, cost and duration of the measurement, spatial resolution required, representativeness, etc.), specific analysis techniques may be chosen. However, an efficient and comprehensive understanding of the crystallization mechanisms leading to glass-ceramics generally requires a combination of these different techniques in order to obtain a multiscale description of the evolution of the organization within the disordered environments. As several characterization techniques in glass science are presented in more detail in other chapters of this book (Part C), only a succinct description of the main characterization techniques used specifically for glass-ceramics is provided here. This section will focus on microstructural characterization techniques, which are strongly related to the macroscopic properties of glass-ceramics. Mechanical, optical, and thermal glass-ceramic properties will not be detailed here.

Thermal Analysis

Among the different calorimetric methods allowing a precise measurement of the thermal evolution of a material, the differential scanning calorimetry (DSC) and differential thermal analysis (DTA) methods are the most used. The transformation of a glass into a glass-ceramic material can be characterized by the acquisition of a thermogram (Fig. 4.24a), which enables determination of the glass transition (T_g) and glass crystallization (T_c) temperatures as well as the melting temperature (T_m). This information is then used to limit the temperature working range for appropriate crystallization thermal treatment. Numerous theoretical works have also demonstrated the possibility of using these analytical methods to better describe the

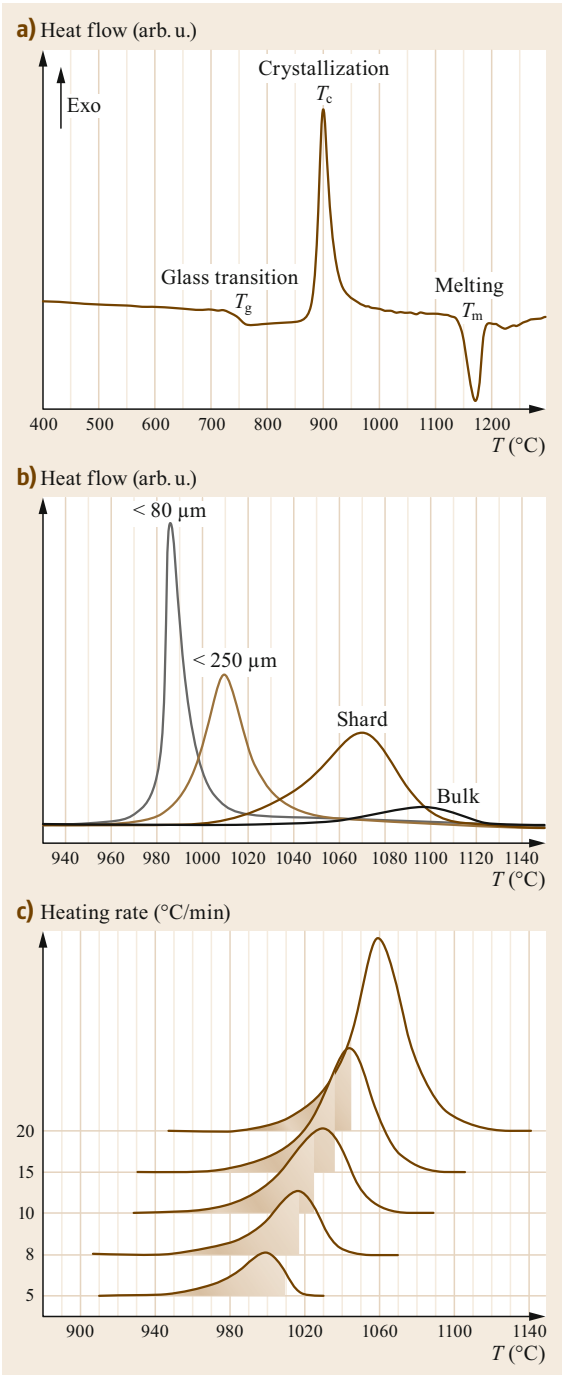

Fig. 4.24 **(a)** Thermogram of a gehlenite ($Ca_2Al_2SiO_7$) glass showing the glass transition (T_g), the crystallization (exothermic peak, T_c), and melting (endothermic peak, T_m) during heating at 10 °C/min. **(b)** Evolution of the crystallization peak of the same glass for different glass grain sizes. **(c)** Evolution of the crystallization rate (hatched area/total peak area ratio) as a function of the heating rate for the same glass at $T = 1010$ °C. After [4.109] ►

crystallization mechanisms. Several pieces of information may be obtained by using thermal analysis measurements:

1. The nature of the nucleation and growth process via measurements using different glass powder grain sizes (Fig. 4.24b) or via the interpretation of the T_g/T_m ratio [4.110, 111]
2. The maximum nucleation and growth temperatures [4.112, 113]
3. The estimation of crystallization kinetics by exothermal series realized at different heating rates (Fig. 4.24c).

The nature of the crystallization process can be obtained from the JMAK model (Sect. 4.2.3). As the glass is thermodynamically metastable, the results of the thermal analysis experiment depend not only on the thermal history of the material (melting temperature, cooling rate, conditions of the thermal annealing treatment...), but also on the experimental conditions (heating rate, sample granularity). It is thus advisable to couple thermal analysis measurements with other characterization methods, especially in situ techniques (x-ray or neutron powder diffraction, Raman spectroscopy, electron microscopy, etc.). For a more detailed discussion please refer to Chap. 24.

Powder Diffraction

The powder diffraction method, mainly carried out by x-ray irradiation in the laboratory (synchrotron and neutron sources can be accessed for specific requirements), enables the identification of the crystalline phases and provides a precise characterization of the average crystallographic structure via the Rietveld analysis [4.114]. Powder diffraction can also provide key information for glass-ceramic characterizations such as the quantification of the crystalline and amorphous phases [4.115]. In this case, the absorption of each crystalline phase has to be properly estimated (possible use of the Brindley correction [4.116]) and the preferred orientation of anisotropic crystallites has to be minimized during data collection. A determination of crystallite size, especially using the Scherrer equation [4.117] or more accurately using the fundamental parameters approach [4.118, 119], can also be acquired as well as the shape and texture of the crystallites [4.120]. Moreover, in situ high-temperature experiments may provide information on crystallization sequence and kinetics (Fig. 4.25). These latter can thus provide time and temperature parameters of the ther-

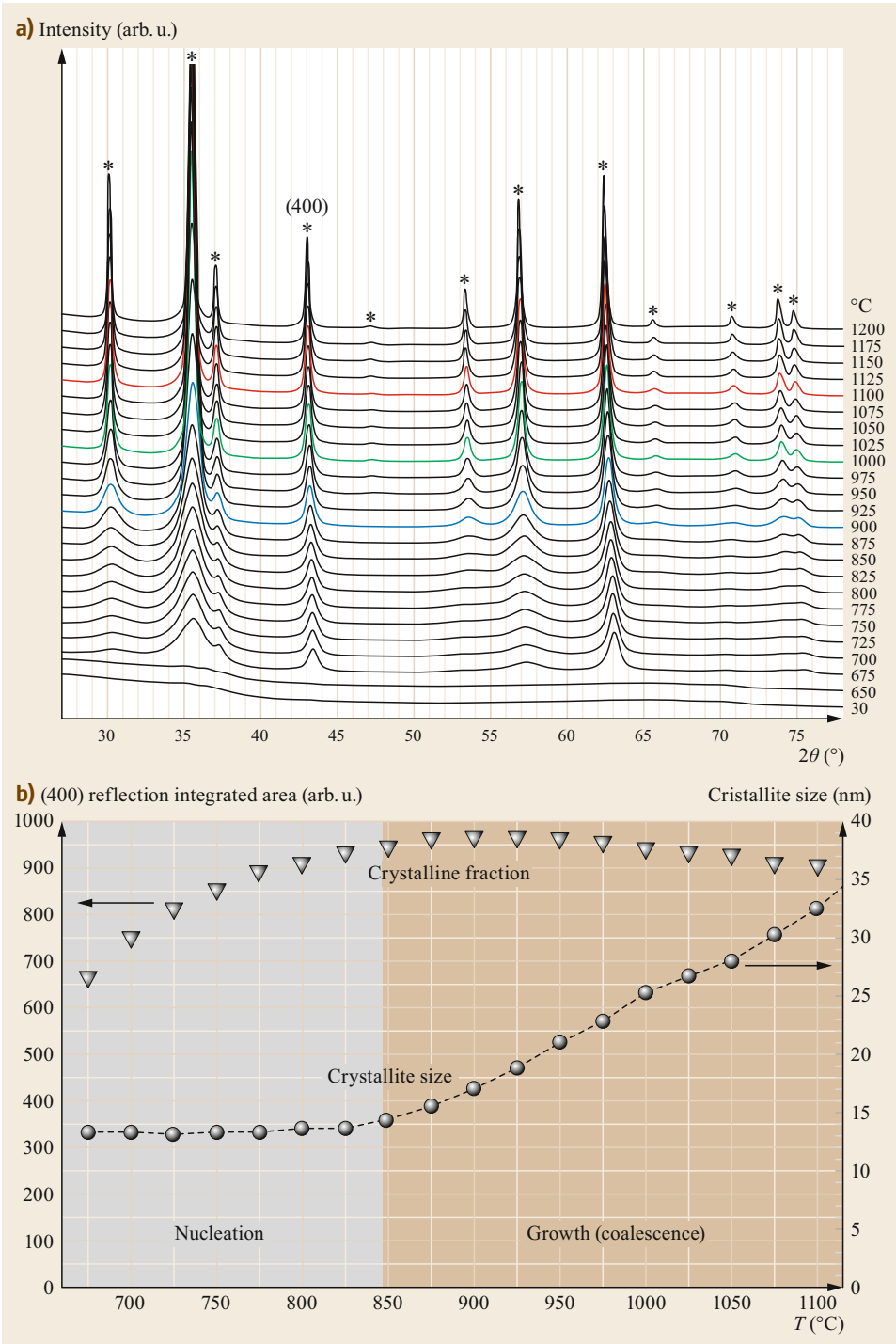

Fig. 4.25 **(a)** In situ x-ray diffractograms collected upon heating from a $55SiO_2$-$5Na_2O$-$17ZnO$-$23Ga_2O_3$ glass powder sample. The diffraction peaks of $ZnGa_2O_4$ according to JCPDS 71-0843 are indicated by *asterisks*. **(b)** Evolution of the (400) reflection integrated area (*left vertical axis*) and of crystallite size (*right vertical axis*) versus temperature. The nucleation and growth regimes are clearly evidenced. Adapted from [4.79] with permission of The Royal Society of Chemistry

mal treatment to be applied to the glass for an efficient crystallization.

Recent developments also offer further possibilities for studying glass-ceramics. For example tomography (3-D imaging), PDF (pair distribution function), and small-angle x-ray (or neutron) scattering (SAXS/SANS) techniques, which rely on the analysis of total scattering data, are especially well adapted for

the study of materials showing a limited degree of crystallinity. For a more detailed discussion please refer to Chap. 30.

Electron Microscopy

The different types of microscopy, optical microscopy (OM), SEM, and TEM are important techniques for the direct observation of glass-ceramic microstructure. Key information such as morphology of both crystalline and amorphous phases, their distribution in the material, and dispersion in size and shape can be directly imaged to provide a precise and multiscale description of a glass-ceramic microstructure. Moreover, these techniques can be performed in situ as a function of temperature, which is of particular interest to determine and understand crystallization in glass processes. Optical microscopy enables the observation of the microstructure at the micrometer scale. To attain smaller scales, electronic microscopy is mandatory. In this case, analytic (chemical composition from energy-dispersive spectroscopy (EDS) measurements) and crystallographic (from diffraction) data are accessible.

Scanning electron microscopy provides imaging of the surface of bulk samples with a resolution down to 10 nm. The image contrast results either from chemical (back-scattered electrons (BSEs) mode) or topographic (secondary electron (SE) mode) differences. It can be necessary to perform a chemical or thermal etching step of the surface to be observed prior to the experiment in order to reveal or enhance the contrast, especially in the case of a congruent crystallization. As demonstrated in Sect. 4.4.2, SEM is of special interest in imaging the different microstructure of glass-ceramics. Complementary tools such as electron back-scattered diffraction (EBSD) and EDS are of special interest to respectively characterize the texture [4.86, 92, 122, 123] (Figs. 4.23, 4.26, and 4.32) and the chemical composition (with the exception of light elements) of the phases with a micrometer-scale resolution.

Transmission electron microscopy, offering access to atomic imaging resolution, is the perfect tool to observe and characterize nanometer-scale glass-ceramics and the first steps of crystallization [4.121, 124]. In addition to these imaging possibilities, electron diffraction gives access to crystallographic information and both EDS and EELS (electron energy-loss spectroscopy) techniques provide analytical information at the nanometer scale (Fig. 4.26a,b). These different TEM approaches can be realized in situ, although the effect of the electron beam irradiation on the sample should not be underestimated. Recently, considerable technological progress has been realized with the conception of a new transmission electron microscope (cold field emission gun, correction of aberration of the electromagnetic lenses) which led to the development of very-high-resolution chemical imaging via scanning transmission electron microscopy-high-angle annular dark field (STEM-HAADF) and energy-filtered transmission electron microscopy (EFTEM) modes. These major evolutions now enable the characterization of glass crystallization from its very first steps (Fig. 4.26c) [4.29, 71, 73, 121, 125–127]. Although the simple observation at the edge of a glass-ceramic grain (obtained from a powdered glass-ceramic whose grains

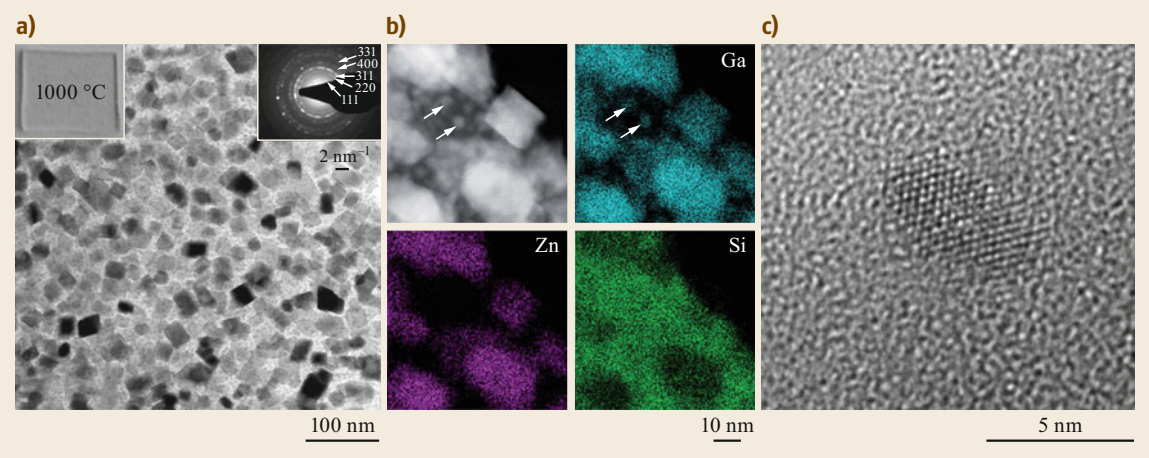

Fig. 4.26 **(a)** Bright-field TEM micrograph of a $55SiO_2$-$5Na_2O$-17ZnO-$23Ga_2O_3$ transparent glass-ceramic material. **(b)** STEM-HAADF image of the same glass-ceramic with associated STEM-EDS elemental maps showing the localization of Zn and Ga in the crystals. Reproduced from [4.79] with permission of The Royal Society of Chemistry **(c)** High-resolution TEM image of a ZrO_2 crystal embedded in a MgO-Al_2O_3-SiO_2 glass matrix. Reprinted from [4.121]. © 2010, with permission from Elsevier

were dispersed in a solution and deposited onto a TEM grid) may be possible, TEM often requires a specific preparation method in order to properly observe a sample which should clearly remain below 100 nm of thickness. For a long time, the direct or indirect replica technique has been used to reproduce accurately the microscale geometry of the original material surface [4.128]. Nowadays, sample preparation is realized either by ultramicrotomy [4.129], mechanical and ionic polishing (PIPS), or direct cutting and extraction of a thin foil by focused ion beam (FIB) [4.130]. This latter technique, although extremely fast and efficient, can induce some defects (amorphization) in the sample to be analyzed. Finally, even though TEM provides high-resolution imaging, it only provides visualization of a limited area of the sample. Therefore, accurate assessment of the sample requires coupling the TEM study with other microscopies or methods probing the whole sample volume.

Although relatively scarcely used, atomic force microscopy (AFM) is a very sensitive tool which can also reveal a glass-ceramic microstructure and especially to detect the presence of small cracks [4.131] or to analyze nucleation mechanisms [4.132]. A detailed account can be found in the Chap. 27.

Spectroscopies

Spectroscopy techniques, which probe the local structure of both crystalline and glassy phases, provide complementary information to the previously cited methods. Some of these spectroscopy techniques, of particular interest in the study of glass-ceramics, are briefly presented here: nuclear magnetic resonance (NMR), Raman, x-ray absorption (XAS), and small-angle x-ray or neutron scattering (SAXS and SANS).

High-resolution NMR enables fine characterization of ordered and disordered structures in both glass and crystalline complex materials. The range of techniques available in modern NMR is now very large (high-resolution, multidimensional NMR, correlation between nuclei, etc.) (Chap. 28) [4.133–138]. This technique is selective regarding the considered element and can provide local state information up to the nanometer scale of the coordinating sphere and the polyatomic structural motif. The recent progress achieved (sensitivity and resolution) provide evidence of different disorder features, which can be topologic, geometric, or chemical [4.139]. Regarding glass-ceramics, NMR can be used to track the evolution of the environment of the studied nucleus, in order to check its presence in the crystalline phase, its proximity to other elements (spatial or through chemical bond proximity), and to probe its coordination and possible elastic strain effects [4.18, 140, 141].

Raman spectroscopy, which is nowadays used as much in the laboratory as it is in industry, is a fast and nondestructive technique which does not require particular sample preparation [4.142]. The contribution of this vibrational spectroscopy to glass-ceramic studies mainly concerns the identification of the different phases (either crystalline or amorphous) and their mapping, possibly in situ [4.143]. By means of the confocal mode, a unique specificity offered by this technique is to probe locally, at the micrometer scale and without sample damage, crystals formed in the glass volume (not at the surface), for example during femtosecond laser writing [4.144, 145].

X-ray absorption spectroscopy (XAS) enables one to probe the specific environment of a given element, for example to understand the role of nucleating agents in a given system [4.121]. Information regarding interatomic distances, coordination, nature of bonding elements, or valence of the elements can thus be obtained [4.146]. Measurements are performed using synchrotron radiation and can also be realized in situ versus temperature with spatial resolution down to 20 nm [4.147].

Small-angle x-ray and neutron scattering (SAXS and SANS) are radiation-scattering techniques used to probe different kinds of heterogeneities ranging from 5 to 500 nm. These provide information on the size and the morphology of scattering particles [4.148, 149]. Applied to glass-ceramic materials, these enable estimation of the radius size of critical nuclei and the distance between particles [4.150–152]. If laboratory SAXS instruments are available, these techniques are mainly developed at synchrotron and neutron facilities where anomalous scattering can also be performed. In this case, it is possible to preferentially probe certain elements, which can for example enable demonstration of core-shell structuring around crystals [4.153]. The information obtained is quantitative in the case of monodisperse systems. However, in the case of polydispersity, the overlap of the different contributions strongly prevents fine information being obtained.

4.4.2 Glass-Ceramic Microstructures

Most of the remarkable properties of glass-ceramic materials are related to their microstructure, defined as the geometrical arrangement and the crystalline phase distribution within the residual glass. This microstructure can present a wide range of morphologies that are very different from one material to another, depending on the crystallization rate, the size, morphology, and distribution of the crystals in the glass. Thus, in order to create a glass-ceramic material with specific properties, it is first necessary to precisely control

its microstructure via a fine mastering of the crystallization mechanism [4.70, 154]. For example, retention of glass transparency in the visible range during crystallization requires a homogeneous distribution of nanometer-scale crystals within the glass-ceramic material (Sect. 4.5.3). Therefore, highly transparent glass-ceramic materials can be obtained in the case of a strong volume nucleation, uniformly dispersed in the material, and coupled to a controlled and limited crystal growth step.

Crystalline Morphology

As seen in Sect. 4.2.3, the crystal growth is affected by interface reactions, heat, and mass transfers. All these factors also control crystal development, form, composition, and homogeneity. The rate-limiting factor is the slowest process and can vary with the degree of supercooling.

At the atomic level, the nature of the interface is important. On a smooth surface, the atom will be loosely bonded, which can prevent crystal growth. On a rough surface, an atom has several available sites of attachment, which increases the probability of finding an energetically stable binding. Consequently, the growth rate tends to be faster for a rough surface than for a smooth surface. The roughness of the surface is preserved during growth, as atoms usually prefer edges or kinks as energetically favored sites. The attachment of the first atom on the smooth surface is the rate-limiting step. Indeed, additional atoms can easily be fixed with this atom acting as a corner and the new layer can be completed quickly, forming a new layer with high activation energy.

The roughness can be characterized by a surface entropy factor α [4.155]

$$\alpha = \frac{1}{k_B T}[2(E_{C-C} + E_{L-L}) - 4E_{C-L}] , \qquad (4.19)$$

with E_{i-j} the bond energy and the subscripts C and L corresponding to the crystal and the liquid, respectively.

The free-energy change for crystallization ΔG_S is given in Fig. 4.27 as a function of the fractional occupation of a single layer, x, and the surface entropy factor. When $\alpha < 2$, the minimum of ΔG_S occurs at $x = 0.5$ (half the available sites are filled), corresponding to a rough surface. When $\alpha > 2$, the minimum of ΔG_S occurs at $x = 0$ (nearly empty flat interface) or $x = 1$ (nearly full flat interface), representing a smooth surface. Practically, α can be estimated from growth rate measurements.

Two mechanisms of growth are generally distinguished [4.35]: (i) continuous growth when structural units attach at any crystal sites, allowing a uniform progress of the crystallization front giving usually a nonfaceted morphology, or (ii) lateral growth when the attachment is realized on preferential sites, either by surface nucleation (e. g., adsorption on an edge), or by screw dislocation, usually giving a faceted morphology. This latter case corresponds to a fraction $\alpha < 1$ in (4.19).

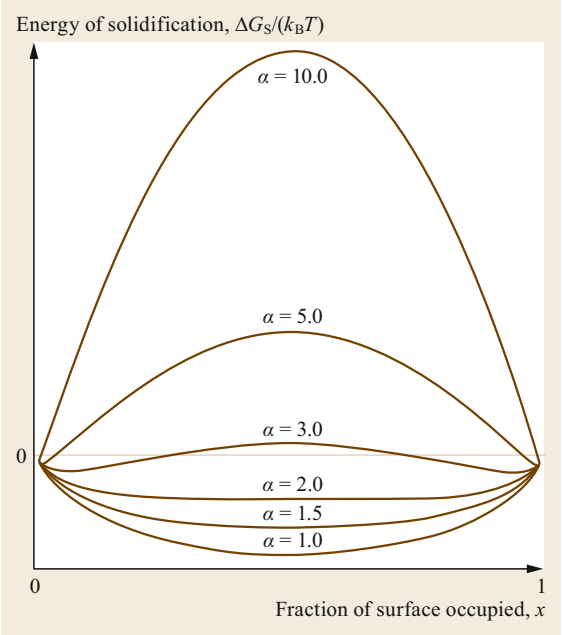

Fig. 4.27 Dependence of fraction of the surface occupied on the Gibbs free energy for various degrees of surface roughness. After [4.156]

Crystal growth and the final morphology change with an increase in the degree of supercooling (Fig. 4.28) as a result of the driving force of crystallization and mass or heat diffusion [4.157, 158]: the morphology is first euhedral, then skeletal, dendritic, and finally spherulitic or fibrillar. The origin of the morphological evolution is not understood in detail but can be ascribed to a stronger influence of diffusion as the degree of supercooling increases.

At large degrees of supercooling, short-range diffusion typically dominates, leading to a growth rate independent of time, and to the formation of spherulitic or fibrillar morphologies. Dendritic morphologies are governed by diffusion and the growing surface is unstable in a diffusion field. The mechanisms leading to these morphologies are both material and heat diffusion and a competition between the promotion and suppression of crystal growth. If the crystal growth is faster than atomic mobility, growth is delayed in certain directions to enable atoms to have time to diffuse. In addition, the heat is drained to the colder parts of the

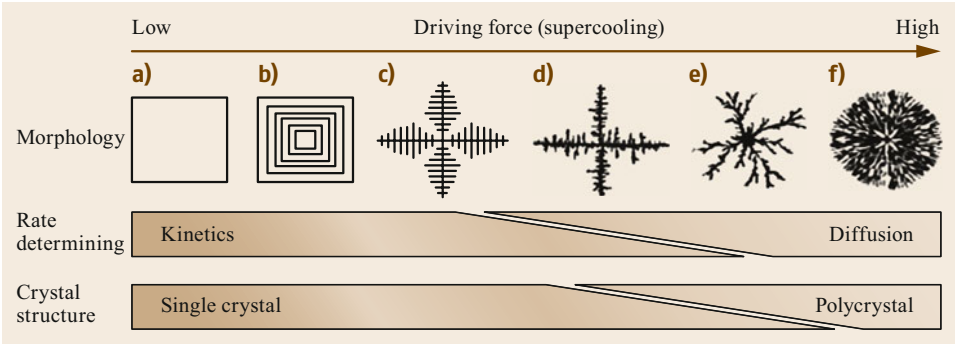

Fig. 4.28a–f Morphological variation of crystals with changes in driving force (*matrix effect*). The schematic models (*upper illustrations*) correspond to **(a)** a euhedral crystal, **(b)** a skeletal crystal, **(c)** an ordered dendrite with crystallographic symmetry, **(d)** a partially disordered dendrite with a single-crystalline ordered trunk and disordered polycrystalline side branches, **(e)** a disordered polycrystalline dendrite, and **(f)** a dense branching morphology. After [4.158]

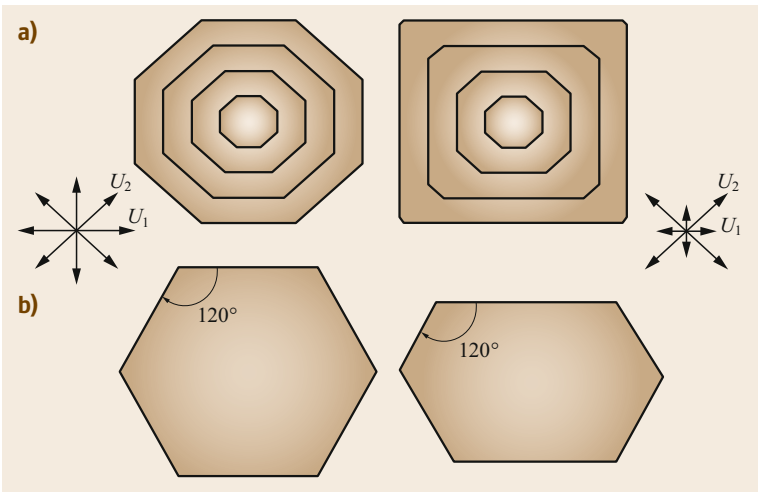

Fig. 4.29a,b Morphological evolution of crystal growth. **(a)** Evolution of the crystal faces due to different growth rate of the faces. *Left*, all faces grow at the same rate. *Right*, faces with a high growth rate (U_2) disappear and the final faces correspond to the faces with a slow growth rate (U_1). **(b)** Illustration of the law of constancy of interfacial angles. Regardless of the face extension, the angle between the faces remains constant

liquid at the front of the interface. This phenomenon can be amplified by impurities blocking growth in specific directions.

Long-range diffusion-controlled growth can generate noncongruent phase transformation. Since the crystal and the liquid have different composition, chemical transport of matter over significant distances is required.

Euhedral crystals (flat surfaces) are controlled by the solid–liquid interface reactions. The growth rate is independent of time (that is, the crystal size is proportional to time) leading to a linear growth law. Diffusion-controlled growth (short or long range, see Sect. 4.2.3) can generate noncongruent phase transformation (the crystal has a different composition to the surrounding liquid). Crystals exhibit edges and vertices but faces are incomplete.

The crystal shape (habitus) is constituted of planes, also called faces, bounding the crystal. The final polyhedral crystal faces are those with the slowest growth rate (Fig. 4.29a). Because of this growth rate anisotropy, the initial rough interfaces disappear giving large smooth faces. The habitus complies with several laws:

- Face extension is not a constant character but angles between adjacent faces or edges are constant (law of constancy of interfacial angles, by *Steno* [4.159] and *Romé of the L'isle* [4.160]). This is schematized in Fig. 4.29b where 2-D crystals show different shapes but the angles remain the same.
- Faces with the lowest Miller indices (*hkl*), i. e., the most densely populated atomic planes, grow more slowly (law of simple rational indices established by *Haüy* [4.161]).

Most Common Glass–Ceramic Microstructures

The combination of an appropriate glass composition with a controlled nucleation and growth mechanism en-

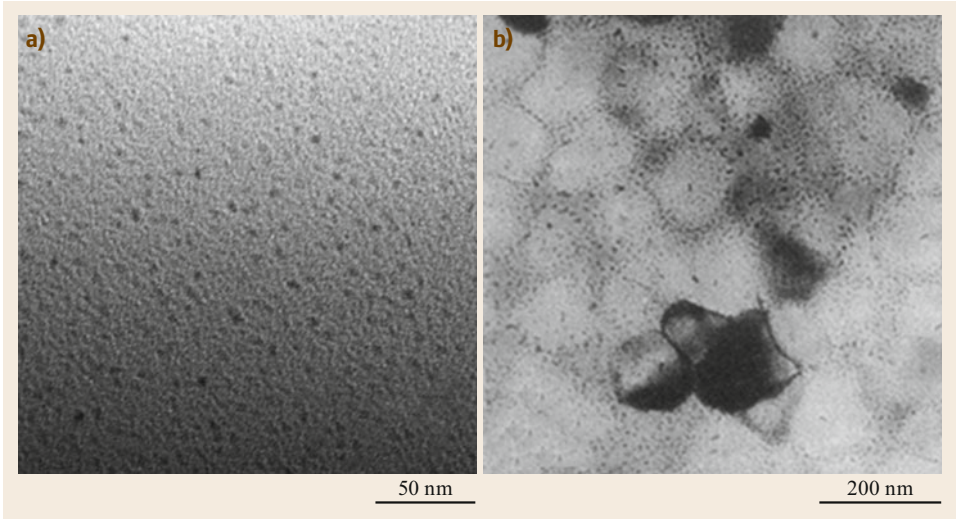

Fig. 4.30a,b TEM images of **(a)** an aluminosilicate glass-ceramic showing nanometer-scale crystallization initiated by $ZrTiO_4$ precipitation (reprinted with permission from [4.126]; © 2010 American Chemical Society) and of **(b)** a β-quartz (LAS) glass-ceramic exhibiting a cellular microstructure. Reprinted with permission from [4.162]

ables the elaboration of glass-ceramics with customized properties. In this section, an overview of the main microstructures usually encountered in glass-ceramics will be presented for each nucleation type. This presentation is inspired from the original classification proposed by *Höland* and *Beall* [4.1]. Several less common microstructures have also been reported. For a detailed description of these microstructures, the reader may refer to specific references [4.1, 124].

Microstructures from Crystallization Using Nucleating Agents. One of the most famous microstructure types is called the *nanocrystalline microstructure* (Fig. 4.30a), as developed for Li_2O-Al_2O_3-SiO_2 (LAS) cooktop glass-ceramics (Sect. 4.5.1 and Fig. 4.34); it represents one of the first examples of nanotechnology [4.163]. Nanocrystalline glass-ceramics are usually developed to achieve remarkable mechanical properties [4.164–166] or for retaining parent-glass transparency during crystallization (as demonstrated for spinel solid solutions [4.78, 167], β-quartz (Fig. 4.30a) [4.69], mullite [4.74], or oxyfluoride compositions) [4.168]. To achieve such a nanometer-scale microstructure, the nucleation step must be very strong, which is attained with the help of nucleating agents. Conversely, the growth step must remain very limited so as to retain the nanometer-scale crystals.

A particular microstructure obtained by crystallization following heterogeneous nucleation is the *cellular microstructure* (Fig. 4.30b). This kind of microstructure is generated by the crystallization of a secondary phase surrounding a first crystallizing phase. For example, still in the LAS (Li_2O-Al_2O_3-SiO_2) system, the heterogeneous nucleation is triggered by the presence of $ZrTiO_4$, first appearing as dark spots preferentially localized within the cells (β-quartz crystals) and at the grain boundaries. A very thin aluminum-rich glass matrix embeds the β-quartz or β-spodumene crystals, so that crystal growth is limited and leads to the appearance of a cellular membrane. This kind of microstructure is particularly useful for creating cooktops, especially for precisely controlling the thermomechanical (low thermal expansion coefficient) and transparency (for aesthetic) properties.

Microstructures from Phase-Separated Glass Crystallization. As detailed previously, crystallization from phase-separated glasses is a process of interest for the development of applied glass-ceramic materials as it induces volume crystallization, such as crystallization induced by nucleating agents and homogeneous crystallization processes.

Relic from phase separation is the most common microstructure type arising from phase-separated glasses. It is named after the great similarities between the microstructure of the phase-separated glass, especially in the case of nucleation and growth phase separation, and the microstructure of the final glass-ceramic. The glassy part of lower viscosity usually crystallizes at lower temperature. Therefore, it is possible to create glass-ceramics retaining the shape of the phase-separated glass (Fig. 4.17b). The resulting microstructure appears as a relic of the initial glass microstructure [4.78, 169].

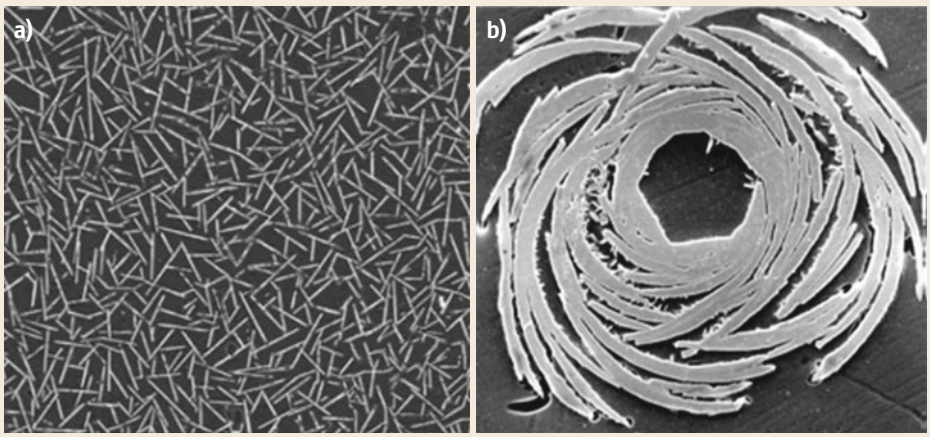

Fig. 4.31 **(a)** SEM image (BSE mode) of a commercial MACOR® glass-ceramic showing mica crystallization with a house-of-cards microstructure. Reprinted with permission from [4.170, 171]. **(b)** SEM image of aggregate of mica crystals arranged with a cabbage-head microstructure type. Reprinted from [4.172]. © 1999, with permission from Elsevier

Contrary to the previous microstructures presenting spheroid shapes, the *house-of-cards microstructure* exhibits a strong anisotropic microstructure. It is characteristic of mica crystallization, as observed in the MACOR® commercial glass-ceramic used for its machinability properties (Fig. 4.31a). This needle-like structuration is generated from the metastable crystallization of norbergite ($Mg_3SiO_4(F,OH)_2$) and fluorophlogopite ($KMg_3(AlSi_3O_{10})(FOH)_2$), further transforming into mica, from a phase-separated aluminosilicate oxyfluoride glass. The disposition of the randomly oriented crystals forms numerous barriers which prevents cracks during machining. Moreover, the interlocked architecture is at the root of the strong dielectric properties measured in this glass-ceramic [4.170, 171].

Mica glass-ceramics exhibit remarkable machinability properties which originate from their strongly anisotropic microstructure. In the case of the house-of-cards microstructure, the spreading of a possible crack is rapidly prevented by a perpendicular needle-like crystal. This feature is also demonstrated for the original cabbage-type microstructure observed during mica crystallization in a Na_2O-K_2O-MgO-Al_2O_3-SiO_2 oxyfluoride matrix (Fig. 4.31b). This microstructure can be explained by a nucleation/growth mechanism originating from a phase separation taking place along isocompositional lines [4.172].

Microstructures from Surface Crystallization. Although surface crystallization is often associated with unwanted surface devitrification, several examples of materials exhibiting surface crystallization with specific microstructures have been developed. The anisotropy of the crystal growth rates favors orientations perpendicular to the surface of the material (Fig. 4.32a,b), and thus increases the mechanical strength in the direction perpendicular to this crystal growth.

The formation of dendritic microstructures can be observed during an internal crystallization process, for example in the cases of the commercial Fotoform® glass-ceramic [4.105], leucite crystallization in the SiO_2-Al_2O_3-Na_2O-K_2O-P_2O_5-F system studied for dental restoration [4.70] (Fig. 4.32a), and PbF_3 crystallization in an aluminosilicate glass [4.124]. Dendritic crystallization is often characterized by a preferred growth direction with occasionally a splitting in parallel branches (Fig. 4.32b).

Recently, advanced SEM characterizations, especially via EBSD, have enabled study of precise surface crystallization mechanisms. For example, crystallization of fresnoite shows oriented nucleation with the *c*-axes preferentially perpendicular to the surface. A very strong 001-texture is observed after only 10 µm of growth into the bulk, making fresnoite a piezoelectric system, in which an orientation preferred during nucleation prevails during growth into the bulk in glass-ceramics (Fig. 4.32d) [4.86, 92, 123].

As previously detailed in Sect. 4.3.2, *Crystallization Processes*, surface crystallization can be used for *pseudovolume* crystallization, especially in the case of glass powder sintering. The common microstructure type obtained from such a process is called *coast and island*. It was first observed by *Beall* et al. in the case of cordierite ($Mg_2Al_4Si_5O_{18}$), pollucite ($(Cs,Na)_2Al_2Si_4O_{12}\cdot 2H_2O$), and leucite ($KAlSi_2O_6$) crystallizations [4.70]. It results from controlled crystallization at the grain boundaries (surface crystallization) observed during glass powder sintering. The crystals appear as a *coast* while the residual glass constitutes the *islands* (Fig. 4.32c). This kind of microstructure is also characteristic of the opals used in dental glass-ceramics [4.88, 173, 174].

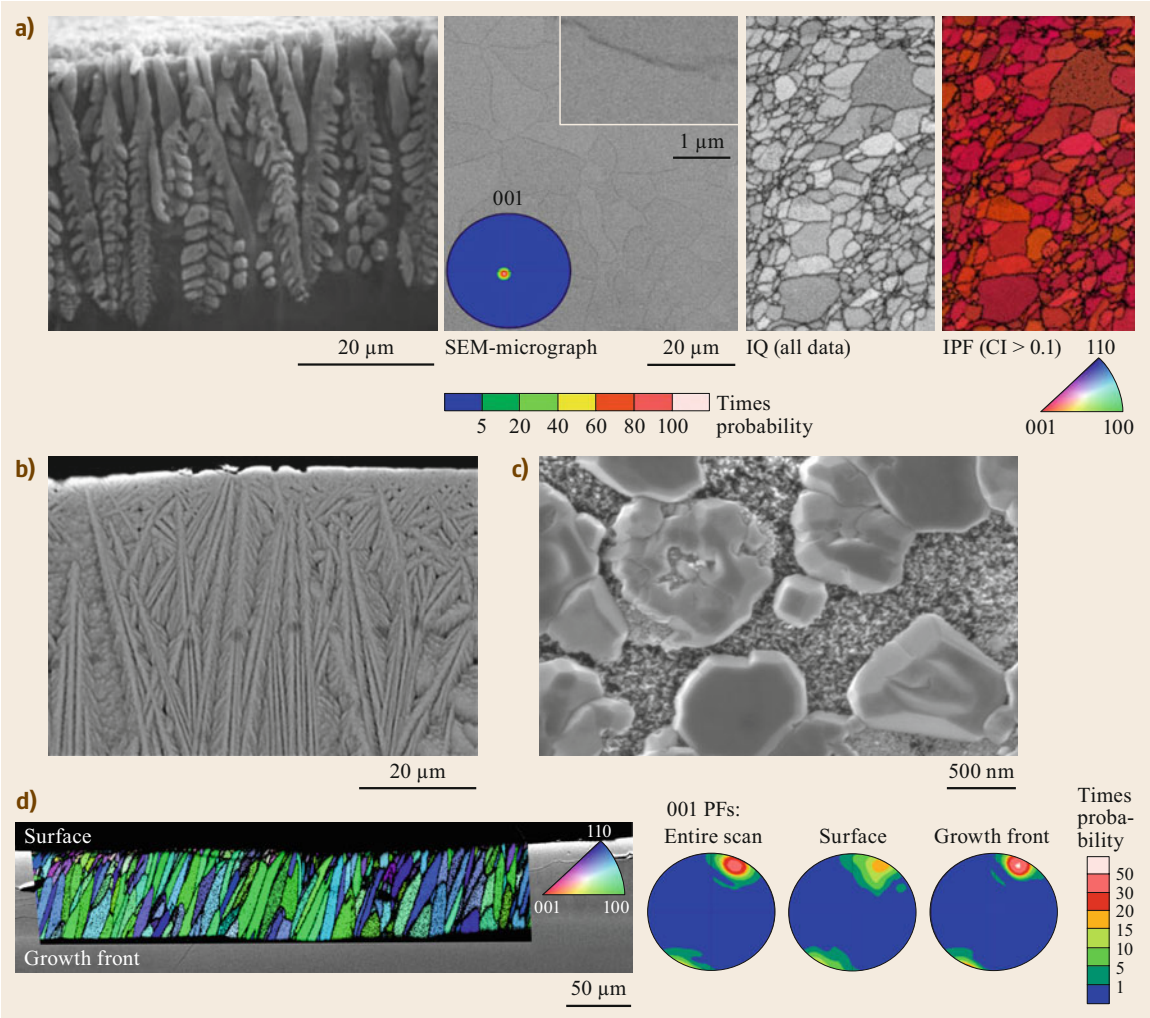

Fig. 4.32 **(a)** SEM image of surface leucite crystallization. Reprinted from [4.174]. **(b)** Bi_2GeO_5 crystals oriented perpendicular to the surface. Reprinted from [4.175]. © 2003 with permission from Elsevier. **(c)** Coast and island microstructure observed from the crystallization of $Bi_2Ru_2O_7$ deposited as a thin film by spray pyrolysis. Reproduced from [4.176] with permission of The Royal Society of Chemistry. **(d)** EBSD-SEM micrographs (surface and section) of the microstructure of a transparent $Sr_2TiSi_{2.45}O_{8.9}$ fresnoite glass-ceramic surface showing the very strong crystallite orientation along the [001] direction. Reprinted from [4.123]

Microstructures from Complex Crystallization Mechanisms. There are complex crystallization mechanisms, either combining different crystallization mechanisms or requiring the use of a specific elaboration setup, which can lead to original microstructures.

For example, in the case of a classic volume crystallization, (homogeneous or heterogeneous nucleation), the orientation of the crystals within the glass matrix is usually random. However, if the crystalline phase is asymmetric, a degree of alignment can be induced during crystal growth using, for example, high-temperature extrusion [4.177], laser-, magnetic- or electric-field-induced crystallization [4.101]. Such an oriented crystallization microstructure is sought after for many properties such as mechanics, resistivity, etc.

Glass-ceramics with an acicular microstructure are usually elaborated to obtain improved mechanical properties, especially for limiting crack propagation [4.179]. In the case of canasite ($Na_4K_2Ca_5Si_{12}O_{30}F_4$), nucleation is realized via the precipitation of CaF_2 which initiates canasite crystal growth with an acicular microstructure (Fig. 4.33a). Further crystallization leads to strong interlocking of the crystals, explaining the remarkable mechanical properties of this material:

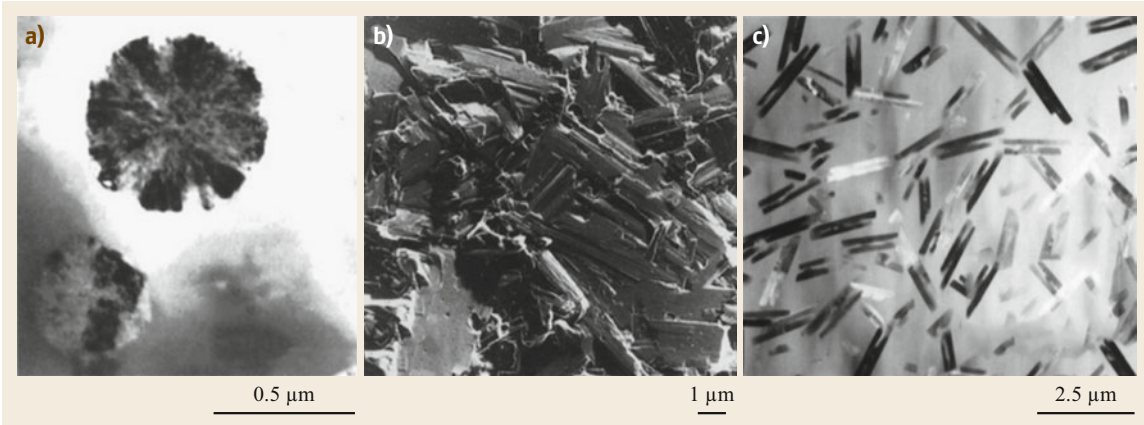

Fig. 4.33a–c TEM images of **(a)** canasite glass-ceramic microstructure with spherulitic growth; **(b)** final acicular glass-ceramic, with high crystallization rate and interlocking, which leads to the reinforced mechanical properties. **(a)** and **(b)** reprinted with permission from [4.65]. **(c)** Mica yo-yo-shaped crystals obtained from extrusion at 820 °C. Reprinted from [4.178]. © 2008, with permission from Elsevier

if cleavage parallel to the layers are possible, their propagation is avoided perpendicular to this direction (Fig. 4.33b).

Lastly, atypical microstructures can be observed as demonstrated for *yo-yo-shaped microstructures*. Although mica usually crystallizes as sheets, it is sometimes possible to observe a yo-yo-shaped microstructure in the case of a small nonstoichiometry in the parent glass. This composition deviation induces the apparition of defects at the time of crystallization, especially norbergite precipitation in the central part of the yo-yos (Fig. 4.33c).

4.5 Glass-Ceramic Applications

By playing around with the composition of the parent glass, the nature and the microstructure of the crystallizing phases, glass-ceramic materials can combine a wide range of physical properties hardly achievable in a classic glass or ceramic material [4.1, 180–183]. These properties (transparency, low thermal expansion coefficient, resistance to temperature or mechanical constraints, etc.) can be used for applications such as cooktops, fire screens, kitchen ware, cutlery, dental implants, mirrors for telescopes, radomes for missiles, matrices for waste management, etc. However, the elaboration of glass-ceramic materials must be realized at reasonable cost in order to be commercial.

This section illustrates diverse types of technical, optical, medical, electrical, magnetic, and aesthetic applications, with a special interest in demonstrating the existing links between the microstructure, obtained by a precise control of the crystallization processes, and the macroscopic properties of the developed glass-ceramic. Some famous commercial glass-ceramic materials will be presented to emphasize this aspect.

4.5.1 Transparent Glass-Ceramics with Low Coefficient of Thermal Expansion

The first and greatest commercial success of glass-ceramic materials was obtained from materials showing low thermal expansion coefficient (resistance to thermal shocks) combined with strong heat resistance and possibly transparency (Fig. 4.34) [4.181].

Such glass-ceramic materials are elaborated from lithium aluminosilicate (LAS) glasses, possibly enriched in CaO, MgO, ZnO, BaO, P_2O_5, Na_2O, and K_2O to ease glass melting and to optimize thermomechanical properties. The use of nucleating agents (especially TiO_2 and ZrO_2) induces the crystallization of numerous $Li_{2-2(x+y)}Mg_xZn_yO\text{-}Al_2O_3\text{-}nSiO_2$ crystals (derived from a β-quartz solid solution structure) with negative thermal expansion (down to $-4\times10^{-6}\,K^{-1}$). The crystallization sequence starts with the formation of nanometer-sized $ZrTiO_4$ crystals at around 700–800 °C (Sect. 4.4.2, *Microstructures from Crystallization Using Nucleating Agents*). This first step expels

Fig. 4.34 Low thermal expansion coefficient glass-ceramic for **(a)** giant telescope mirror (SCHOTT ZERODUR®) and **(b)** cooktops (SCHOTT CERAN® Miradur™). **(c)** Fire-resistant windows (SCHOTT ROBAX®). **(d)** Cookwares (VISIONS®, a registered trademark of World Kitchen, LLC)

aluminum at the edge of the crystals which further induces crystallization of a β-quartz solid solution at around 800–900 °C. The size of the crystals is maintained below 70 nm to ensure transparency in the visible range (Sect. 4.5.3) and the crystallization rate can reach 70 vol.% (Fig. 4.26a) [4.126, 162, 184–186].

The β-quartz solid solution is metastable and evolves into β-spodumene above 950 °C. However, the high-temperature treatment required for this phase transition induces crystal growth which leads to transparency loss in the glass-ceramic (increase in crystal size). Nevertheless, such elaborated glass-ceramic materials still exhibit low thermal expansion coefficient and are used for similar applications when transparency is not required.

With the thermal expansion coefficient of a glass-ceramic material being the weighted mean of the thermal expansion coefficient of the crystalline phase(s) and the residual glass phase, it is possible to precisely control the thermal expansion coefficient of the final material by varying the composition of the solid solution and the crystallization rate. As the transparency can also be tailored depending on the size of the crystals (Sect. 4.5.3), numerous applications have been developed (Fig. 4.30 and Table 4.2). A spectacular application of such glass-ceramics is the development of giant telescope mirrors (Zerodur® (Schott)), whose development was enabled by the almost null thermal expansion coefficient ($0 \pm 0.02 \times 10^{-6}\,K^{-1}$) coupled to a perfect homogeneity of the glass-ceramic material (Fig. 4.34a).

4.5.2 Machinable Glass-Ceramics

Machinable glass-ceramics have been developed for applications such as technical pieces in numerous areas (semiconductor, vacuum, electronics, aerospace, and laser industries for example) (Fig. 4.35a). The

Table 4.2 Examples of commercial transparent glass-ceramics with low thermal coefficient

Application	Initial glass composition (wt%)	Crystalline phase	Thermal coefficient (10^{-6} K^{-1})	Characteristics	Commercial name
Telescope mirror	57.2 SiO_2, 25.3 Al_2O_3, 6.5 P_2O_5, 3.4 Li_2O, 1.0 MgO, 1.4 ZnO, 0.2 Na_2O, 0.4 K_2O, 0.5 As_2O_3, 2.3 TiO_2, 1.8 ZrO_2	β-quartz s.s.	0±0.02	– Translucent – High homogeneity	– Zerodur® (Schott)
Fire-resistant windows	55–70 SiO_2 15–27 Al_2O_3 3–7 Li_2O	β-quartz s.s.	≈ +0.3	– High transparency – Heat resistance (700 °C)	– Robax® (Schott) – Keralite (Eurokera) – Neoceram® (Nippon)
Cookwares		β-spodumene s.s.	≈ +0.7	– Resistance to thermal shocks	– CorningWare® (Corning)
Transparent cookwares		β-quartz s.s.	≈ +1	– Transparency – Resistance to thermal shocks	– Vision® (Corning)
Translucent cooktops	0–4 MgO 0–4 ZnO 2–5 TiO_2+ZrO_2	β-quartz s.s.	> −0.3 and < +0.15	– Transparency – Thermal resistance – Hardness	– Ceran® (Schott) – Kerablack® (Eurokera) – Neoceram N-0® (Nippon)
Cooktops		β-spodumene s.s.	≈ +1.3	– Thermal resistance – Esthéticism (coloration) – Hardness	– Kerawhite® (Eurokera) – Neoceram N-11® (Nippon)

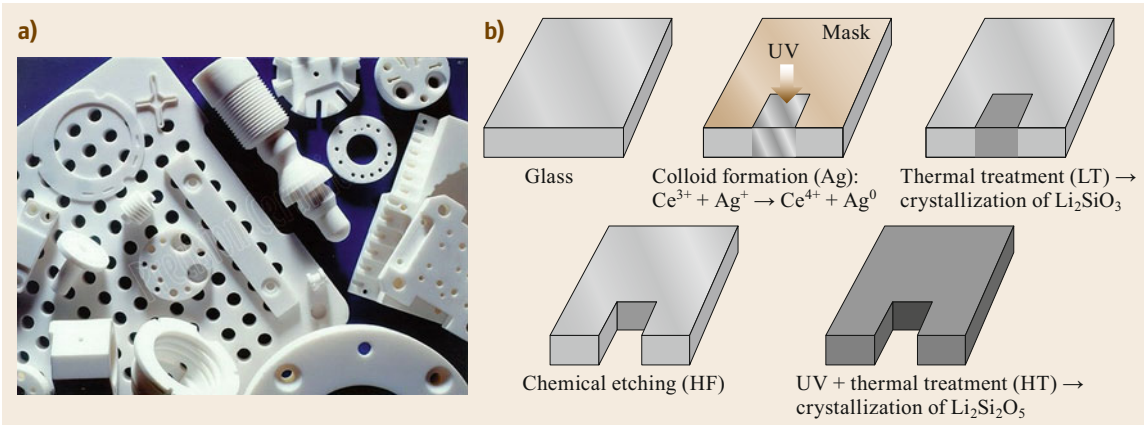

Fig. 4.35 (a) Machinable glass-ceramics (Courtesy of Precision Ceramics UK). (b) Scheme of the elaboration process of chemically machined glass-ceramics

two main machining processes are mechanical machining and chemical machining of photoengraving materials.

Mechanical machining is used for materials such as mica-based glass-ceramics. These usually exhibit a house-of-cards microstructure (Fig. 4.31a) obtained from random orientation of mica sheets which are interconnected, thus forming numerous barriers to the propagation of cracks during machining (Sect. 4.4.2, *Microstructures from Phase-Separated Glass Crystallization*). Structural damage is thus limited to small residual glass areas, which enables a machining tolerance of about 10 µm. Moreover, the interlocking of the mica sheet crystals also leads to remarkable dielectric properties and very low gas permeability (Table 4.3).

The elaboration of glass-ceramics from chemical machining is a multistep process. First, lithium silicate glasses are synthesized using a small amount of silver salt and cerium oxide in order to induce photosensitivity. After glass forming, UV irradiation is performed on areas to be removed. This irradiation induces oxidation of Ce^{3+} into Ce^{4+} via reduction of Ag^{+} into Ag^{0}. During the first crystallization heat treatment performed at around 500–600 °C, Li_2SiO_3 dendrites, not chemically stable, are formed in irradiated areas. Chemical etching, for example performed using hydrofluoric acid, then leads to removal of the crystallized areas. Fi-

Table 4.3 Examples of commercial machinable glass-ceramics

Application	Initial glass composition (wt%)	Crystalline phase	Thermal coefficient (10^{-6} K^{-1})	Density	Young's modulus (GPa)	Resistivity (Ω cm)	Knoop hardness (100 g)	Commercial name
Mechanical machining	47.2 SiO_2, 16.7 Al_2O_3, 14.5 MgO, 9.5 K_2O, 8.5 B_2O_3, 6.3 F	Mica $KMg_3AlSi_3O_{10}F_2$	9.4	2.52	67	$> 10^{16}$	250	Macor® (Corning)
Chemical machining after photoengraving	79.6 SiO_2, 4 Al_2O_3, 9.3 Li_2O, 4.1 K_2O, 1.6 Na_2O, 0.11 Ag, 0.014 CeO_2, 0.4 Sb_2O_3	$Li_2Si_2O_5$	10.3–16	2.40	87	$> 10^{16}$	500	Fotoceram® (Corning)
	75–85 SiO_2, 3–6 Al_2O_3, 7–11 Li_2O, 3–6 K_2O, 1–2 Na_2O, 0–2 ZnO, 0.05–0.15 Ag_2O, 0.01–0.04 CeO_2, 0.2–0.4 Sb_2O_3	$Li_2Si_2O_5$	10.5	2.41	88	5.6×10^{16}	520	Foturan® (Schott)

nally, during the final crystallization step performed at high temperature (600–700 °C), the remaining material is fully crystallized into $Li_2Si_2O_5$, a much more stable crystalline phase compared to Li_2SiO_3 (Fig. 4.35b). Such materials are used for the fabrication of high-precision components (micron-scale machining) in various domains such as micromechanics, micro-optics, and microfluidics.

4.5.3 Optical Glass-Ceramics

Since the first transparent glass-ceramics developed in the 1960s for their low coefficient of thermal expansion (Sect. 4.5.1), numerous studies have been devoted to the research of optical and photonic glass-ceramics. These materials find application mostly in communications and solar thermal energy. Highly transparent glass-ceramics show improved mechanical and active optical properties compared to their glass counterparts. This can be partly explained by the segregation of the dopants in the crystallites [4.187–189]. By combining glass transparency with specific optical/photonic properties of crystalline phases, light excitation and emission in glass-ceramic materials takes place in the whole sample volume, enabling glass-ceramics to compete with the costly single-crystal technology which offers low shaping flexibility.

Transparency in Glass-Ceramics

During the crystallization process, glass transparency is usually degraded, if not totally lost, because of the creation of light-scattering centers (porosity, interface between different refractive index environments, large grain boundaries, etc.). Different theoretical models have been developed to simulate light scattering in heterogeneous matrices [4.190]. Here we will consider Rayleigh's scattering which can be applied for crystallites with sizes significantly lower (at least 10 times) than the incident wavelength [4.191]. From this model, at least one of the two following conditions must be obtained to generate negligible light scattering, i. e., transparency:

- The refractive indices of the glass and the crystalline phases are very close. In this case, it is also required that the material be optically isotropic (no birefringence effect) and does not show any refractive index fluctuation. In practice, these conditions are rarely fulfilled [4.192].
- The size of the crystallites must be much smaller than the wavelength of the incident light, which is obtained in most actual transparent glass-ceramics (crystallite sizes well below 100 nm to achieve transparency in the visible range–usually below 70 nm). In order to ensure transparency in these ma-

terials during crystallization, it is useful to predict the maximum crystallite size allowed in a given matrix. For this purpose, recent theories simulating turbidity (attenuation due to light scattering) have been developed and demonstrate that a maximum crystallite size of 50–70 nm allows retention of glass transparency in the visible range during crystallization [4.193–195].

In order to synthesize a transparent glass-ceramic material, several processes can be applied. The most common one is the use of nucleating agents to induce strong heterogeneous nucleation (Sect. 4.2.1, *Heterogeneous Nucleation*) which is coupled to a short thermal treatment to limit the crystallite size. Numerous transparent glass-ceramics are also developed from a nanometer-scale phase separation (Sect. 4.3.1, *Phase-Separated Glasses* and Figs. 4.16 and 4.17). In this case, the size of the crystals remains smaller than the size of the phase-separated domains, at least before any coalescence effect takes place. Lastly, a transparent glass-ceramic can also be prepared despite a surface crystallization mechanism by using a compaction and sintering process. However, it is difficult to get rid of all residual porosity, and so of associated light scattering, via this process (Sect. 4.3.2, *Crystallization from Glass Powder Sintering*).

A particular case of transparency is opalescence which is defined as the property of a translucent material which scatters only short wavelengths of the visible range (blue light), whereas the longest wavelengths are transmitted (green and red lights). In glass-ceramics, opalescence can be obtained from homogeneous nanoparticles well dispersed in the glass matrix, with a size typically slightly below 100 nm. Such opalescent glass-ceramics can be used in dental restoration (Sect. 4.5.4).

Oxide Transparent Glass-Ceramics

Oxide-based compositions are the most common of transparent glass-ceramics. Although the LAS (Li_2O-Al_2O_3-SiO_2) system was the first that demonstrated production of transparent glass-ceramics with low coefficient of thermal expansion (Sect. 4.5.1), numerous other systems have been studied and developed.

Mullite (SiO_2–Al_2O_3 System) Transparent Glass-Ceramics. In the pseudobinary SiO_2-Al_2O_3 family, glass compositions with high contents show a nanometer-scale phase separation. Upon crystallization, the alumina-rich nanometer-scale domains will selectively crystallize into spherulitic mullite nanocrystals, dispersed in a silicate matrix, and thus lead to transparent glass-ceramics retaining glass transparency [4.74, 77, 163]. The addition of alkaline-earth or boron oxides eases melting/glass formation and control of the phase separation. However, in this case the phase separation is no longer spontaneously present in the glass obtained by melt quenching but appears during later heat treatment.

These mullite transparent glass-ceramics can be doped with Cr^{3+} (substituting for Al^{3+}) for luminescence applications and more especially for concentrated solar power technology [4.196–199]. However, despite their remarkable transparency, light emission currently remains insufficient. A smaller crystal size and higher crystallization rate would be required to enhance luminescence efficiency.

Aluminate Transparent Glass-Ceramics. Ten-nanometer spinel nanocrystals with a composition varying between $MgAl_2O_4$ and $ZnAl_2O_4$ (gahnite) have been elaborated from the SiO_2-Al_2O_3-ZnO-MgO system [4.74, 163]. A 30–40% crystal volume fraction can be achieved when nucleation is induced by TiO_2 or ZrO_2 nucleating agents. These materials present a remarkable thermal stability and a coefficient of thermal expansion ($3–4\times10^{-6}\,K^{-1}$) close to the value of silicon. They are therefore of potential use as substrates for flat panels or photovoltaic devices [4.167].

Translucent YAG ($Y_3Al_5O_{12}$) glass-ceramics have also been prepared [4.202, 203]. Ce^{3+} doping then yields a strong yellow emission under a blue LED excitation. Nevertheless, enhanced transparency and higher crystallization rate remain necessary in order to compete with polycrystalline ceramic technology developing white LEDs by coupling the yellow YAG emission to the blue emission from the exciting LED [4.204, 205]. This elaboration process still requires further improvement as opacity appears during crystallization, because of the refractive index difference between the glass and the crystalline phases, even in the case of a glass matrix composition very close to that of the YAG composition [4.206]. Note that YAG-Al_2O_3 glasses, further leading to nanometer scale biphasic YAG-Al_2O_3 ceramics via a full bulk glass crystallization process [4.207], could offer an alternative to these limitations.

Remarkable long-lasting luminescent Eu^{2+},Dy^{3+}:$SrAl_2O_4$ glass-ceramics with high transparency in the visible region were also successfully synthesized using an innovative frozen sorbet technique [4.208, 209] with the control of O_2 partial pressure (PO_2) for the oxidation of Eu^{2+} ions. Through the quenching of melts (e. g., $55SrO_2$-$7Al_2O_3$-$18B_2O_3$ with Eu_2O_3 and Dy_2O_3), $SrAl_2O_4$ crystals with a diameter of 40 μm are fabricated and lie in the glass phase. Eu^{2+},Dy^{3+}-

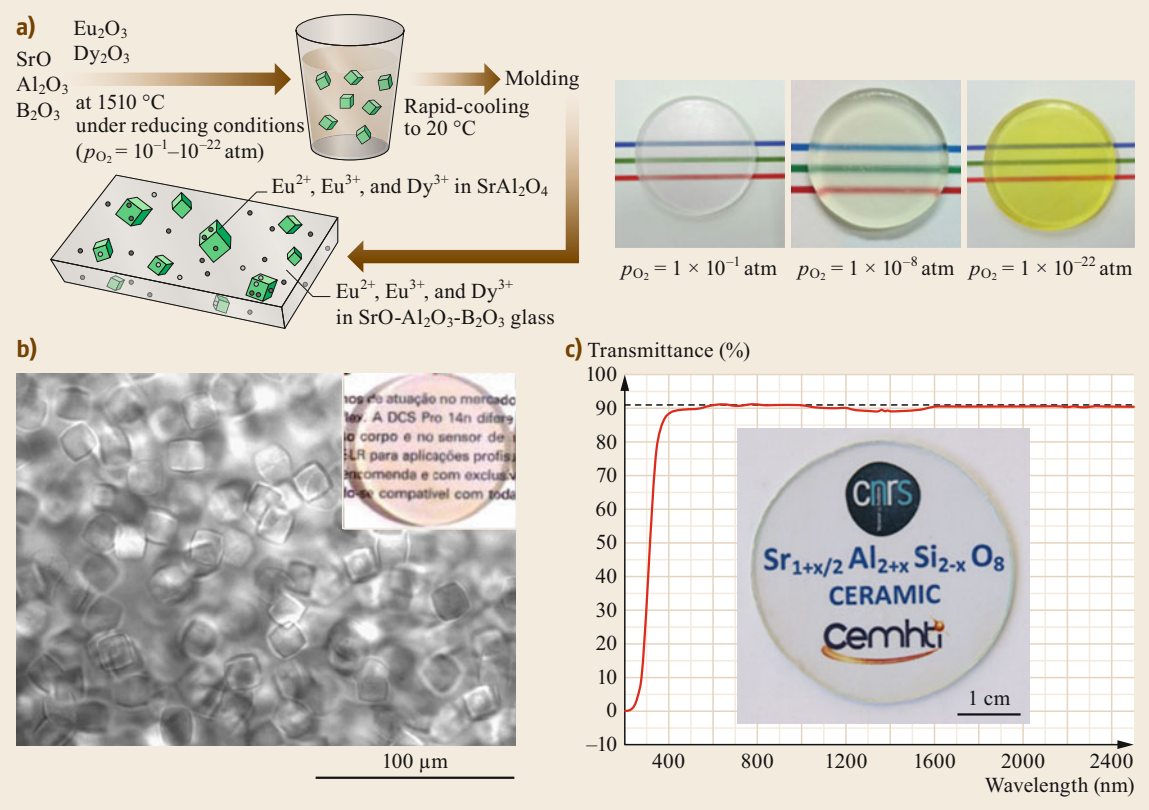

Fig. 4.36 **(a)** Long-lasting luminescent Eu,Dy:$SrAl_2O_4$ transparent glass-ceramics elaborated by the frozen sorbet technique. Adapted with permission from [4.200]. **(b)** NCS transparent glass-ceramic characterized by micrometer-scale crystals ($Na_{4+2x}Ca_{4-x}Si_6O_{18}$). Reprinted from [4.192], © 2008, with permission from Elsevier. **(c)** Transmittance spectrum and photograph of $Sr_{1+x/2}Al_{2+x}Si_{2-x}O_8$ ($x = 0.2$) transparent polycrystalline ceramic elaborated by full crystallization from glass. Adapted with permission from [4.201], © 2015 American Chemical Society

codoped materials appear to be promising materials for application in novel photonic and light storage materials (Fig. 4.36a) [4.200].

Orthosilicate (Forsterite, Willemite) Transparent Glass-Ceramics. Forsterite (Mg_2SiO_4) and willemite (Zn_2SiO_4) can crystallize from the MAS (MgO-Al_2O_3-SiO_2) [4.210] and ZAS (ZnO-Al_2O_3-SiO_2) [4.211] systems. These nanocrystalline glass-ceramics are transparent and exhibit fluorescence in the near-infrared region when they are doped with Cr^{4+} [4.212]. Moreover, these materials exhibit nonlinear optical properties, with an efficiency similar to that of single-crystal technology, when they are doped with Co^{2+} [4.213]. Remarkably, in the ZAS system, hexagonal ZnO crystals with tunable size (5–20 nm) can be precipitated [4.214]. When doped with Sb^{3+}, these glass-ceramics demonstrate adjustable absorption from visible to infrared ranges.

Gallate Transparent Glass-Ceramics. Lithium aluminogallate glass-ceramics ($Li(Ga,Al)_5O_8$ solid solution) doped with Ni^{2+} show strong dark brown coloration as a glass and become turquoise after crystallization [4.215]. These materials show luminescence emission in the infrared range [4.216–218] and can be drawn as fibers with similar properties, which may open the way to optical applications [4.219].

Barium gallogermanate (BGG) glasses such as the 20BaO-10Ga_2O_3-70GeO_2 composition are highly transparent in the near-infrared and lead to $BaGe_4O_9$ glass-ceramics with improved mechanical properties. These materials retain glass transparency and are of special interest for military applications [4.220, 221]. The possibility of tuning luminescence properties in Ni^{2+}-doped gallogermanate glass-ceramics (80GeO_2-12Ga_2O_3-8Na_2O composition) was also demonstrated over a large infrared range [4.222]. Lastly, new highly transparent nanostructured gallogermanate-based glass

and glass-ceramic materials have been reported. The parent glasses present nanoscale phase separation whose size can be tailored depending on the nominal composition (Sect. 4.3.1, *Choice of the Parent Glass Composition*). The large variety of accessible compositions combined with precise control of the nanostructuration offers a great opportunity to design new highly transparent nanostructured glass-ceramics with a wide range of tunable optical properties both in the visible and the infrared ranges, as demonstrated for $ZnGa_2O_4$ glass-ceramics which are highly transparent and have long-lasting luminescence [4.78, 79].

Laser-Assisted Crystallization. As discussed in Sect. 4.3.2, *Crystallization Induced by Laser Irradiation*, crystallization can be induced by laser irradiation, especially using femtosecond laser technology. This process has been demonstrated for several noncentrosymmetric materials such as $LiNbO_3$ [4.100, 223], $Ba_2Ti(Ge,Si)_2O_8$ [4.224, 225], $LaBGeO_5$ [49] [4.95], and β-BaB_2O_4 [4.226] in silicate matrices. These glass-ceramics can demonstrate nonlinear optical properties and also piezoelectricity and ferroelectricity for applications as waveguides, optical switches, or frequency convertors [4.107, 227]. Recently, the possibility of perennial optical information storage was demonstrated [4.108].

Towards Transparent Polycrystalline Ceramics. Transparent glass-ceramics with high crystallization rate were reported from the NCS (Na_2O-CaO-SiO_2) system (Fig. 4.36b) [4.192]. In this case, the retention of transparency during crystallization was explained by the strong similarity between the refractive index of the crystals ($Na_{4+2x}Ca_{4-x}Si_6O_{18}$ solid solution) and the residual glass. This work opened the way to elaboration of fully crystalline transparent (glass-)ceramics.

Transparent polycrystalline ceramics are usually synthesized from high-temperature and high-pressure sintering of raw crystalline powders. They constitute an emerging class of optical and photonic materials which is competing with single-crystal technology over a wide range of applications (scintillators, transparent armors, optical lenses, etc.) [4.228–231]. However, their elaboration remains complex, costly, and the presence of residual pores preventing high transparency is difficult to avoid for numerous compositions. In fact, only a few compositions of transparent polycrystalline ceramics have been reported, most of them exhibiting cubic symmetry, such as $Y_3Al_5O_{12}$ (YAG) [4.232], $MgAl_2O_4$ [4.233], sesquioxides [4.234], and ZrO_2 [4.235]. Therefore, a recent approach using a full and congruent crystallization from a glass process enables the combination of several advantages: absence of porosity, high and homogenous doping, shaping ability, and possibly reduced cost. Several polycrystalline materials such as $BaAl_4O_7$ (orthorhombic symmetry), $Sr_3Al_2O_6$ (cubic symmetry), $Sr_{1-x}RE_{1+x}Ga_3O_{7+x/2}$ (tetragonal symmetry), $Bi_{0.8}Nb_{0.8}Te_{2.4}O_8$ (cubic symmetry), $Sr_{1+x/2}Al_{2+x}Si_{2-x}O_8$ (hexagonal symmetry), and YAG-Al_2O_3 (biphasic, hexagonal symmetry) have been elaborated via this innovative process (Fig. 4.36c) [4.23, 201, 207, 236–242].

Non-Oxide Transparent Glass-Ceramics

The development of photonic applications led the scientific community to focus on fluoride and chalcogenide compositions. Indeed, contrary to oxides, the low phonon energy of these systems allows retention of transparency up to the infrared range (Fig. 4.37). As light scattering is less important at these long wavelengths, high transparency can be obtained, although mechanical and chemical durability properties usually remain limited.

Oxyfluoride Transparent Glass-Ceramics. Pure fluoride glass-ceramic compositions, which can accommodate high rare earth contents, can be elaborated [4.245–247]. However, their synthesis is difficult (atmospheric control required, fluorine volatilization hardly avoidable), costly, and the resulting materials do not show great chemical durability. Therefore, the addition of oxides has been considered, in order to combine the ease of rare earth incorporation of fluorides with the thermal and chemical properties of oxide glasses. Actually, transparent oxyfluoride glass-ceramics show strong segregation of rare earth elements within the nanocrystals during crystallization (strong affinity of rare earth elements for fluorine anions). Moreover, these materials are of particular interest for the development of new

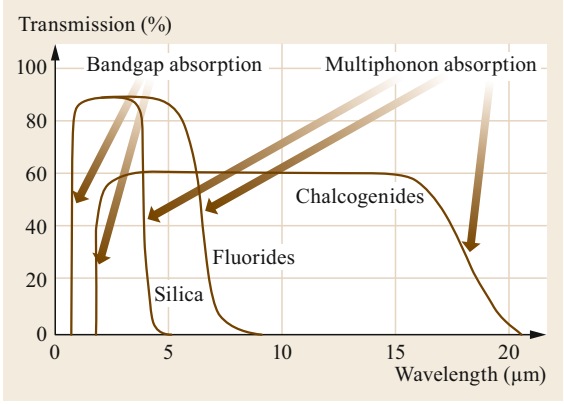

Fig. 4.37 Transmission spectra of different transparent glass-ceramic families

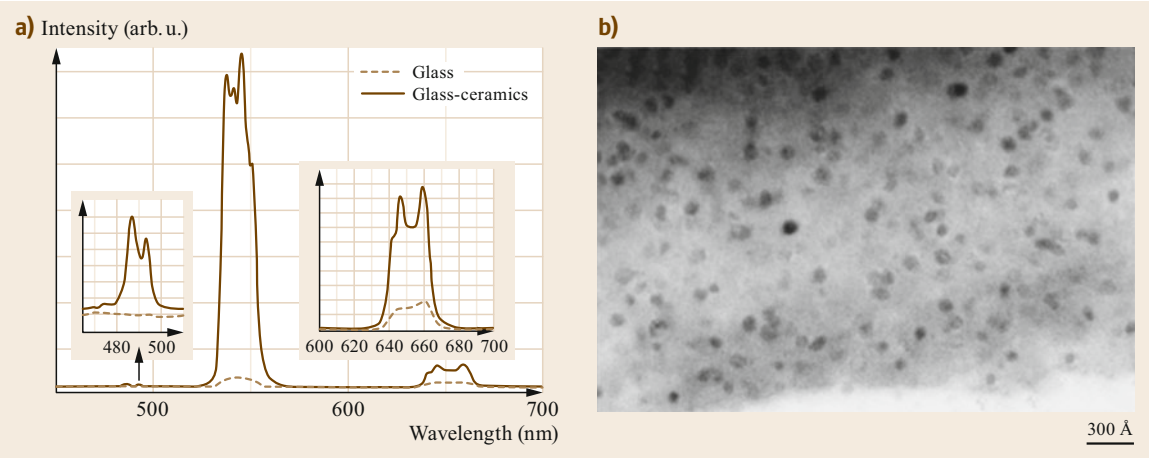

Fig. 4.38 **(a)** Luminescence spectra of $30SiO_2$-$15AlO_{1.5}$-$28PbF_2$-$22CdF_2$-$3.9GdF_3$-$0.1HoF_3$-$1YbF_3$ glass and glass-ceramic materials under a 980 nm excitation. After [4.243]. **(b)** TEM image of a germanate-based oxyfluoride glass-ceramic. Reprinted with permission from [4.244]

optoelectronic setups, especially in regard to up-conversion luminescence (emission at higher energy than the exciting wavelength). Two main families of oxyfluoride materials can be distinguished:

- Aluminosilicate-based oxyfluorides: during crystallization of SiO_2-Al_2O_3-PbF_2-CdF_2 compositions, rare earth cations (Yb^{3+} and Er^{3+}) introduced as doping agents are segregated in 20 nm $(Pb,Cd)F_2$ nanocrystals of fluorine structure. This feature leads to an up-conversion efficiency 100-times higher than that of the noncrystallized glass (Fig. 4.38a) [4.187]. These results opened the way to trials of numerous dopings, of which Nd^{3+}, which is segregated at more than 85% in the fluoride nanocrystals, led to the demonstration of a laser effect [4.248]. The synthesis of a 5 μm glass-ceramic fiber containing 10 nm crystals has also been demonstrated. This fiber shows attenuation below 1 dB m^{-1} [4.249]. Following this success, various fluoride crystalline phases have been introduced in aluminosilicate matrices, especially CaF_2 [4.250–252] or LaF_3 [4.75, 253, 254]. Recently, pure silicate oxide matrices have been used [4.255, 256], enabling the incorporation of new elements such as SrF_2 or BaF_2 [4.257, 258].
- Germanate-based oxyfluorides: the $50GeO_2$-$40PbO$-$10PbF_2$ composition is at the root of transparent glass-ceramics characterized by 10 nm β-PbF_2 nanocrystals [4.188]. Doping with Er^{3+} cations was used to demonstrate optical amplification applications [4.259, 260].

Even though oxyfluoride glass-ceramics have not yet undergone large-scale industrial development, they remain promising materials for various photonic applications.

Chalcogenide Transparent Glass-Ceramics. Chalcogenide glasses (glasses based on sulfur, selenium, or tellurium; Chap. 15) show great transparency in the near- and mid-infrared regions (up to 20 μm) [4.261, 262]. These materials are semiconductors that show ionic conductivity when they are doped by alkaline or silver ions. They also exhibit structural modifications when under the effects of optical or electrical stimuli. These remarkable properties are the root of diverse applications: battery electrolytes, optical devices for night vision, infrared waveguides, and active materials for data storage devices. The controlled crystallization of chalcogenide glasses (i) enables enhancement of their rather modest mechanical properties and (ii) is mandatory for the development of electrical memory.

The first chalcogenide glass-ceramics showing transparency in the infrared were reported in 1973 [4.265, 266]. Starting from a $PbSeGe_{1.5}As_{0.5}Se_3$ glass composition, 500 nm lead selenide crystals were obtained and the glass-ceramics showed transparency between 8 and 12 μm. The use of nucleating agents in the Ag-Ge-Se-Sn system then enabled development of smaller crystallite sizes and so widened the transmittance window towards the near-infrared [4.267]. However, the crystallization process in chalcogenide glasses remained uncontrolled until the discovery of chalcohalides (GeS_2-Sb_2S_3-CsCl) [4.268]. The addition of ionic compounds such as halides induces a competition effect which limits the crystallization rate (Fig. 4.39a,b). Such glass-ceramics find application as lenses for thermal imaging [4.269, 270]. Active optical

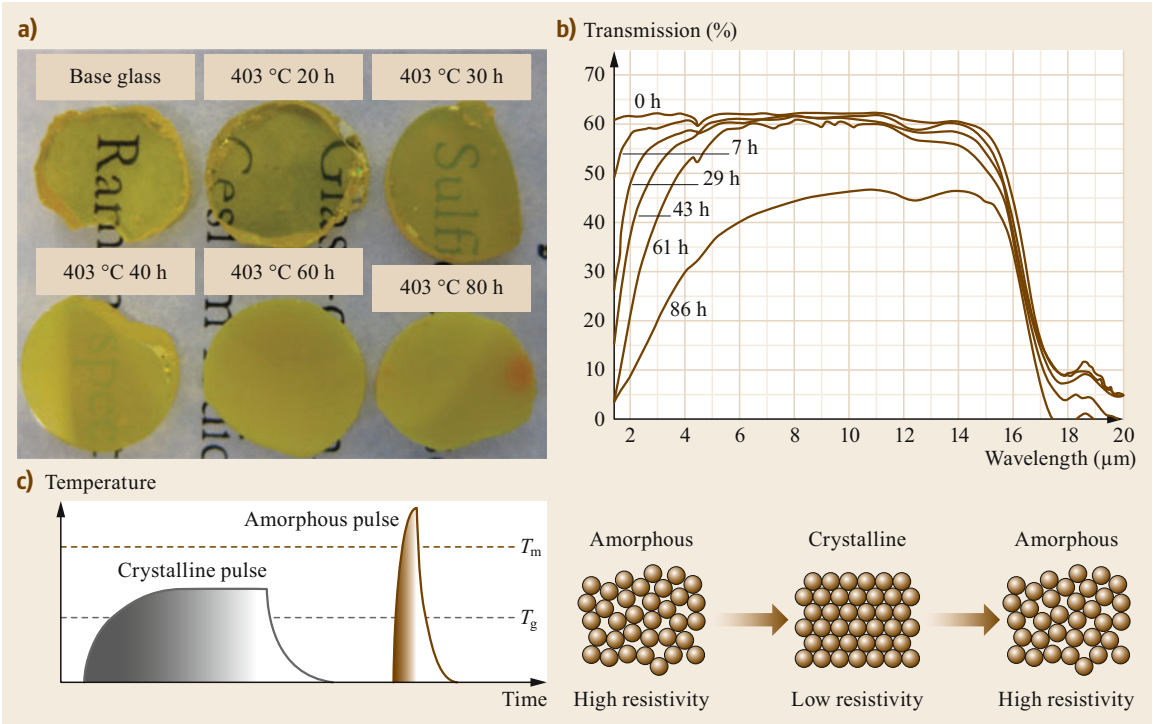

Fig. 4.39 **(a)** Transparent chalcogenide glass-ceramics obtained from the $62.5GeS_2$-$12.5Sb_2S_3$-25CsCl glass composition. Reproduced from [4.263] with permission of The Royal Society of Chemistry. **(b)** Transmission spectra of glass-ceramic materials elaborated from a $80GeSe_2$-$20Ga_2Se_3$ glass composition heat treated at 380 °C for different durations. After [4.264]. **(c)** Scheme of electrical switching in chalcogenide phase-change materials

applications have also been developed, thanks to the segregation of the doping agents in the nanocrystals whose low phonon energy crystalline environment is favorable to high quantum yields [4.271].

Recently, the crystallization of noncentrosymmetric nanoparticles enabled nonlinear optical properties to be accessed [4.272, 273]. However, shaping/molding processes remain very complex and therefore limit applications to fibers even though a promising alternative elaboration process could be the synthesis at low temperature combining ball-milling and sintering by SPS for large bulk pieces (Fig. 4.22).

A particular class of telluride are called phase-change materials (PCMs; see Chap. 44): these materials have the ability to switch from an amorphous state to a crystalline state under a laser or electrical pulse effect. This transformation is reversible depending on the applied temperature, very fast (phase transition of a few nanoseconds), and almost infinitely reproducible (Fig. 4.39c). The work of *Ovshinsky* relating to the development of data storage devices [4.274] led to the rewritable compact disk technology whose active material is a telluride. Current research is devoted to electrical storage devices (where electrical pulses replace laser pulses) in order to replace flash memories [4.275].

Lastly, chalcogenide glass-ceramics can also show remarkable Li^+ conductivity and thus are interesting candidates for solid-state batteries. The high polarizability of sulfur and selenium induce conductivity properties greater than for oxides. The crystallization of well-controlled crystallite composition in the $70Li_2S$-$30P_2S_5$ (molar composition) allows high conductivities (up to 4×10^{-3} S cm^{-1}) to be obtained [4.276].

4.5.4 Glass-Ceramics for Biomedical Applications

Numerous biomedical applications have been developed for glass materials such as for the 45S5 or BioGlass® glasses developed by *Hench* [4.277, 278]. However, only glass-ceramics materials will be discussed here and the reader may refer to Chap. 23 for more detail on biomedical glasses. The main interests of glass-ceramic materials for biomedical applications lie in their mechanical, aesthetic, and/or biological properties. Three types of glass-ceramics differing in their applications and properties can be distinguished:

materials for dental implants, cosmetic dentistry, and orthopedic surgery (Table 4.4).

Glass-Ceramics for Dental Implants

The realization of dental structures (pillars, crowns, bridges, etc.) requires materials with remarkable mechanical properties, especially regarding toughness and fracture strength. First glass-ceramics based on leucite crystallization and characterized by surface crystallization were developed from the K_2O-Al_2O_3-SiO_2 system using sintering of glass powder (IPS Empress®, Ivoclar) [4.88]. Then, their modest mechanical properties motivated the development of glass-ceramics with greater resistance, especially for the creation of dental bridges, leading to the use of the Li_2O-SiO_2 system, crystallizing to lithium disilicate [4.279]. Most current dental glass-ceramics are shaped by machining, in particular using the CAD-CAM (Computer-Assisted Design-Machining) approach. Mica glass-ceramics from the SiO_2-Al_2O_3-MgO-K_2O system were the first materials to be used for these applications. As mica sheets cleave very easily, these glass-ceramics present remarkable machining properties (Dicor MGC®). Nowadays, the CAD-CAM process is mainly used for commercial glass-ceramics based on leucite (ProCAD®, Ivoclar), feldspath (InCeram®, Vita), or lithium disilicate (IPS e.max®, Ivoclar) [4.280].

Glass-Ceramics for Cosmetic Dentistry

The main goal of cosmetic dental surgery consists in covering dental implants with a glass-ceramic layer, whose external aspect mimics natural enamel and exhibits remarkable mechanical properties. Regarding dental restoration, esthetics is very important to the patient. Optical properties (fluorescence, opalescence, and translucence) must simulate as much as possible natural teeth (Fig. 4.40a). Lithium disilicate-based glass-ceramics are often employed to perform this biomimetic function, via the deposition of a cosmetic layer on the dental implant. In addition to its esthetic function, this covering must demonstrate specific strength properties (strength high enough to perform mastication, but not too high in order to avoid deterioration of the protagonist tooth). Apatite glass-ceramics, crystallizing in the SiO_2-Al_2O_3-CaO-Na_2O-K_2O-P_2O_5 system, are also frequently used. In this case, needle-shape fluoroapatite crystals can be synthesized without precipitation of leucite (IPS Empress 2®). The obtained morphology is very similar to the one observed in natural teeth, with therefore very close optical properties (Fig. 4.36a). Another possibility consists in crystallizing both leucite and apatite (IPS d.Sign®) via two distinct crystallization mechanisms. The precipitation of leucite at the surface of the grains of glass powder is coupled to apatite

Table 4.4 Characteristics of dental and orthopedic glass-ceramics

Application	Initial glass composition (wt%)	Crystalline phase	Density	Fracture strength (MPa)	Transmittance (%)	Tenacity ($MPa\,m^{0.5}$)	Young modulus (GPa)	Thermal coefficient ($10^{-6}\,K^{-1}$)	Commercial name
Dental implants	56–64 SiO_2, 0–2 Al_2O_3, 15–20 MgO, 12–18 K_2O, 4–9 F, 0–5 ZrO_2	$K_{1-x}Mg_{2.5+x/2}Si_4O_{10}F_2$ ($x < 2$)	2.7	828 (compression)	56	2.1	70.3	7.2	Dicor® (Corning)
	SiO_2-Al_2O_3-CaO-Na_2O-K_2O-P_2O_5	Lithium disilicate	2.5	360–400 (flexion)	55–80	2.3–2.9	95–120	10.6	IPS e.max® (Ivoclar)
	SiO_2-Al_2O_3-CaO-Na_2O-K_2O-P_2O_5	Leucite	1.95	160 (flexion)	50–60	1.3	65	15–18	IPS Empress® (Ivoclar)
Cosmetics dentistry	50–65 SiO_2, 8–20 Al_2O_3, 7–13 K_2O, 4–12 Na_2O, 0.1–6 CaO, 0–5 P_2O_5, 0.1–3 F, Li_2O, ZrO_2	Fluoroapatite and leucite	–	80 (flexion)	10-90	1.1	–	12.6	IPS d.sign® (Ivoclar)
Orthopedic surgery	34 SiO_2, 44.7 CaO, 4.6 MgO, 16.2 P_2O_5, 0.5 CaF_2	Apatite and wollastonite	3.07	1080 (compression) 215 (flexion)	0	2.0	118	–	Cerabone® (Nippon)
	48.9 SiO_2, 27.3 Al_2O_3, 11.7 MgO, 3.2 Na_2O, 5.2 K_2O, 3.7F	Mica and apatite	2.8	450 (compression) 90–140 (flexion)	0	1.2–1.8	70	7.5–12	Bioverit II® (Vitron)

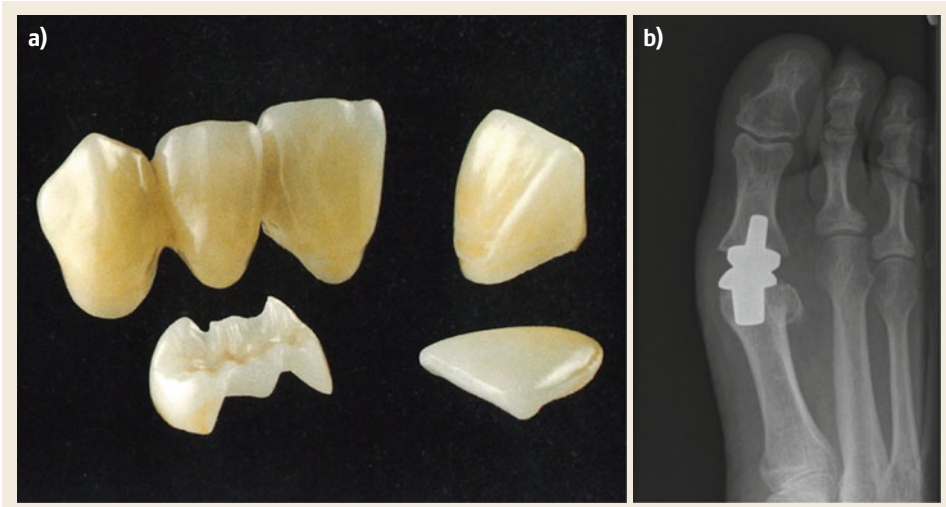

Fig. 4.40a,b Examples of glass-ceramics for biomedical applications. **(a)** Dental restoration glass-ceramics (products of Ivoclar Vivadent AG, reprinted with permission from [4.281]). **(b)** Orthopedic glass-ceramics: prosthesis radiography

crystallization within the volume, initiated by nanometer-scale phase separation, and leading to the presence of these two crystalline phases for better biomimetics [4.64].

Glass-Ceramics for Orthopedic Surgery

Apatite-based glass-ceramics are also used as orthopedic implants. Commercial materials such as Cerabone® (apatite-wollastonite), Ceravital (apatite-devitrite), and Bioverit (mica-apatite) are particularly adapted to the preparation of dense blocks. Cerabone® is elaborated from a SiO_2-CaO-MgO-P_2O_5-CaF_2 glass powder which is first fully densified at 830 °C and further crystallized around 880 °C to generate both oxyfluoroapatite ($Ca_{10}(PO_4)_6(O,F)_2$) and wollastonite ($CaSiO_3$) nanocrystals (50–100 nm) homogeneously dispersed in glass [4.282]. This glass-ceramic material demonstrates mechanical properties similar to materials based on lithium disilicate (Sect. 4.5.2) and presents remarkable bioactivity properties (formation of a hydroxyapatite layer in contact with biological fluids). These glass-ceramic materials are particularly used in spinal surgery [4.283].

4.5.5 Glass-Ceramics for Diverse Applications

Other types of applications have also been developed for glass-ceramics. Some of them are briefly cited here.

Glass-Ceramics for Building Materials

The most famous glass-ceramic building material is Neoparies® (NEG), which is produced at relatively low cost and shows remarkable mechanical properties and chemical durability. It is used at large scale as an architectural coating material for flat or curved panels (Fig. 4.21d). This glass-ceramic is composed of wollastonite ($CaSiO_3$) crystals which arise from a surface nucleation mechanism (Fig. 4.21c). Shaping is performed by glass powder sintering with possible addition of binders [4.93].

Glass-Ceramics for Waste Immobilization and Valorization

The constant growth of industrial development leads to an increase in waste of which only a part can be recycled. Some hazardous, toxic, or radioactive materials must be neutralized or isolated [4.284]. Radioactive wastes, especially wastes coming from nuclear fuel, require either a complete dissolution in the glass melt or encapsulation in chemically and physically stable matrices [4.285, 286]. SiO_2-B_2O_3-Al_2O_3-Na_2O-CaO is a typical glass matrix used for nuclear reprocessing. Nowadays, numerous studies are focusing on glass-ceramic matrices, such as SiO_2-B_2O_3-Al_2O_3-Na_2O-CaO-MoO_3-Ln_2O_3. Glass-ceramics offer enhanced mechanical properties and chemical durability compared to glass and can incorporate higher waste concentration in the matrix [4.287–289]. In the case of hazardous or toxic but nonradioactive industrial waste (ashes, sludge), the glass-ceramic encapsulation strongly limits dissolution. Valorization of such glass-ceramic materials is even conceivable [4.290–292], as demonstrated by the Cofalit® (Europlasma) material produced from asbestos waste (SiO_2-CaO-MgO-Al_2O_3-Fe_2O_3) and valorized for road construction and thermal storage in concentrated solar power technology [4.293].

Substrates for Electronics

The production of films for the microelectronic industry (such as for printed circuit boards) requires particular substrates with high dielectric properties. P_2O_5-B_2O_3-SiO_2 glass-ceramics with boron phosphate BPO_4 answer these needs given their resistivity, which is higher than polycrystalline alumina [4.294].

Glass-Ceramics for Coating and Sealing

Glass-ceramics for ceramic-metal junctions (glass sealing) have also been developed, in particular for energy and biological applications. The main condition to ensure quality sealing is to use a glass-ceramic with a thermal coefficient of expansion identical to the coated/sealed materials in order to ensure high impermeability [4.295–298].

Glass-Ceramics for Energy

Glass-ceramics are also developed for energy production, storage, or saving. For example, $LiFePO_4$ glass-ceramics are used as cathodes for lithium batteries which may prove more efficient than their ceramic counterparts [4.299, 300]. Glass-ceramics are also sought to be used for thermal storage in concentrated solar power technology [4.301, 302].

4.6 Conclusion and Future Directions

Through this chapter, the reader has been able to apprehend the diversity of properties and applications of glass-ceramics. Although these materials are relatively recent, a great variety of compositions has been developed, in particular by improving our understanding of the nucleation and growth mechanisms. It is now possible to precisely control the microstructure of the crystalline phases in many glass matrices, and thus the properties induced in the glass-ceramics.

A significant improvement of the properties of glass-ceramics compared to those of glasses, ceramics, and single crystals has been demonstrated in numerous areas, such as consumer products (cookwares and cooktops), technical applications (machinable glass-ceramics), optical materials (phosphors), and medical devices (dental prostheses). These advances have allowed the commercialization of new products, some of which have now become mass consumed.

There are many prospects for development. The search for new synthesis methods will probably extend the domains of glass compositions available today by making possible the glass formation of previously inaccessible refractory compositions. New crystalline phases will thus probably be used and will lead to the elaboration of original materials.

Moreover, several recent research directions, as developed in Sect. 4.5, appear promising: localized crystallization by femtosecond laser irradiation for 3-D design of glass-ceramics and applications to data storage, biocide glass-ceramics limiting the proliferation of viruses and bacteria, optical fibers with crystalline nanoparticles, glass-ceramics for the storage of solar energy synthesized from waste (asbestos), transparent (glass-)ceramics elaborated by complete crystallization of the glass... Although it is difficult to predict what the materials of the future will be, we stipulate that the conjunction of different properties in multifunctional materials is likely to be the next step in the development of glass-ceramic technology.

References

4.1 W. Höland, G.H. Beall: *Glass-Ceramic Technology*, 2nd edn. (Wiley, Hoboken 2012)

4.2 D.R. Neuville, L. Cormier, D. Caurant, L. Montagne (Eds.): *From Glass to Crystal – Nucleation, Growth and Phase Separation: From Research to Applications* (EDP-Sciences, Les Ulis 2017)

4.3 M. Montazerian, S.P. Singh, E.D. Zanotto: An analysis of glass-ceramic research and commercialiation, Am. Ceram. Soc. Bull. **94**, 30–35 (2015)

4.4 R.J. Kirkpatrick: Theory of nucleation in silicate melts, Am. Mineral. **68**, 66–77 (1983)

4.5 J.W. Gibbs: On the equilibrium of heterogeneous substances, Trans. Conn. Acad. Arts Sci. **3**, 108–248 (1876), (1874–1878)

4.6 M. Volmer, A. Weber: Keimbildung in übersättigten Gebilden, Z. Phys. Chem. **119**, 277 (1926)

4.7 R. Becker, W. Döring: Kinetische Behandlung der Keimbildung in übersättigten Dämpfen, Ann. Phys. **24**, 719–752 (1935)

4.8 E.D. Zanotto, V.M. Fokin: Recent studies of internal and surface nucleation in silicate glasses, Philos. Trans. R. Soc. A **361**, 591–612 (2003)

4.9 Y. Takahashi, M. Osada, H. Masai, T. Fujiwara: Transmission electron microscopy and in situ Raman studies of glassy sanbornite: An insight into nucleation trend and its relation to structural variation, J. Appl. Phys. **108**, 063507 (2010)

4.10 J. Deubener, R. Bruckner, M. Sternitzke: Induction time analysis of nucleation and crystal growth in

di- and metasilicate glasses, J. Non-Cryst. Solids **163**, 1–12 (1993)
4.11 P.C. Soares Jr, E.D. Zanotto, V.M. Fokin, H. Jain: TEM and XRD study of early crystallization of lithium disilicate glasses, J. Non-Cryst. Solids **331**, 217–227 (2003)
4.12 V.M. Fokin, E.D. Zanotto, J.W.P. Schmelzer: Homogeneous nucleation versus glass transition temperature of silicate glasses, J. Non-Cryst. Solids **321**, 52–65 (2003)
4.13 Y. Takahashi, H. Masai, T. Fujiara: Nucleation tendency and crystallizing phase in silicate glasses: A structural aspect, Appl. Phys. Lett. **95**, 071904 (2009)
4.14 E.D. Zanotto: Isothermal and adiabatic nucleation in glass, J. Non-Cryst. Solids **89**, 361–370 (1987)
4.15 E.D. Zanotto: Glass crystallization research – A 36-year retrospective. Part I, fundamental studies, Int. J. Appl. Glass Sci. **4**, 105–116 (2013)
4.16 J. Schneider, V.R. Mastelaro, H. Panepucci, E.D. Zanotto: ^{29}Si MAS-NMR studies of Q^n structural units in metasilicate glasses and their nucleating ability, J. Non-Cryst. Solids **273**, 8–18 (2000)
4.17 V.R. Mastelaro, E.D. Zanotto, N. Lequeux, R. Cortes: Relationship between short-range order and ease of nucleation in $Na_2Ca_2Si_3O_9$, $CaSiO_3$ and $PbSiO_3$ glasses, J. Non-Cryst. Solids **262**, 191–199 (2000)
4.18 J.G. Longstaffe, U. Werner-Zwanziger, J.F. Schneider, M.L.F. Nascimento, E.D. Zanotto, J.W. Zwanziger: Intermediate-range order of alkali disilicate glasses and its relation to the devitrification mechanism, J. Phys. Chem. C **112**, 6151–6159 (2008)
4.19 B. Chen, U. Werner-Zwanziger, M.L.F. Nascimento, L. Ghussn, E.D. Zanotto, J.W. Zwanziger: Structural similarity on multiple length scales and its relation to devitrification mechanism: A solid-state NMR study of alkali diborate glasses and crystals, J. Phys. Chem. C **113**, 20725–20732 (2009)
4.20 B. Chen, U. Werner-Zwanziger, J.W. Zwanziger, M.L.F. Nascimento, L. Ghussn, E.D. Zanotto: Correlation of network structure with devitrification mechanism in lithium and sodium diborate glasses, J. Non-Cryst. Solids **356**, 2641–2644 (2010)
4.21 D. Kashchiev: Solution of the non-steady state problem in nucleation kinetics, Surf. Sci. **14**, 209–220 (1969)
4.22 V.M. Fokin, E.D. Zanotto: Continuous compositional changes of crystal and liquid during crystallization of a sodium calcium silicate glass, J. Non-Cryst. Solids **353**, 2459–2468 (2007)
4.23 S. Sen, T. Mukerji: A generalized classical nucleation theory for rough interfaces: Application in the analysis of homogenous nucleation in silicate liquids, J. Non-Cryst. Solids **246**, 229–239 (1999)
4.24 M. Roskosz, M.J. Toplis, P. Beson, P. Richet: Nucleation mechanisms: a crystal-chemical investigation of phase forming in highly supercooled aluminosilicate liquids, J. Non-Cryst. Solids **351**, 1266–1282 (2005)
4.25 M. Roskosz, M.J. Toplis, P. Richet: Experimental determination of crystal growth rates in highly supercooled aluminosilicate liquids: implications for rate-controlling processes, Am. Mineral. **90**, 1146–1156 (2005)
4.26 G. Gruener, P. Odier, D. De Sousa Meneses, P. Florian, P. Richet: Bulk and local dynamics in glass-forming liquids: a viscosity, electrical conductivity, and NMR study of aluminosilicate melts, Phys. Rev. B **64**, 24206–24201–24205 (2001)
4.27 T. Kawasaki, H. Tanaka: Formation of a crystal nucleus from liquid, Proc. Natl. Acad. Sci. USA **107**, 14036–14041 (2010)
4.28 O. Dargaud, L. Cormier, N. Menguy, G. Patriarche, G. Calas: Mesoscopic scale description of nucleation processes in glasses, Appl. Phys. Lett. **99**, 021904 (2011), https://doi.org/10.1063/1.3610557
4.29 O. Dargaud, L. Cormier, N. Menguy, G. Patriarche: Multi-scale structuration of glasses: Observations of phase separation and nanoscale heterogeneities in glasses by Z-contrast scanning electron transmission microscopy, J. Non-Cryst. Solids **358**, 1257–1262 (2012)
4.30 J. Russo, H. Tanaka: The microscopic pathway to crystallization in supercooled liquids, Sci. Rep. **2**, 505 (2012)
4.31 J. Russo, H. Tanaka: Nonclassical pathways of crystallization in colloidal systems, MRS Bulletin **41**, 369–374 (2016)
4.32 W. Ostwald: Studien über die Bildung und Umwandlung fester Körper, Z. Phys. Chem. **22**, 289–330 (1897)
4.33 S.Y. Chung, Y.M. Kim, J.G. Kim, Y.J. Kim: Multiphase transformation and Ostwald's rule of stages during crystallization of a metal phosphate, Nat. Phys. **5**, 68–73 (2009)
4.34 L. Burgner, M. Weinberg: Crystal growth mechanisms in inorganic glasses, Phys. Chem. Glass.-Eur. J. Glass Sci. Technol. B **42**, 184–190 (2001)
4.35 R.J. Kirkpatrick: Crystal growth form the melt: A review, Am. Mineral. **60**, 798–814 (1975)
4.36 J.W. Christian: *The Theory of Transformations in Metals and Alloys* (Pergamon, Oxford 1975)
4.37 M. Avrami: Kinetics of Phase Change. I General Theory, J. Chem. Phys. **7**, 1103–1112 (1939)
4.38 A.N. Kolmogorov: On the statistical theory of the crystallization of metals, Bull. Acad. Sci. URSS (Cl. Sci. Math. Nat.) **3**, 355 (1937)
4.39 W.A. Johnson, R.F. Mehl: Reaction kinetics in processes of nucleation and growth, Trans. Am. Inst. Min. Eng. **135**, 416–458 (1939)
4.40 C.N.R. Rao, K.J. Rao: *Phase Transitions in Solids* (McGraw-Hill, New York 1978)
4.41 V.M. Fokin, E.D. Zanotto, N.S. Yuritsyn, J.W.P. Schmelzer: Homogeneous crystal nucleation in silicate glasses: A 40 years perspective, J. Non-Cryst. Solids **352**, 2681–2714 (2006)
4.42 J.W.P. Schmelzer, A.R. Gokhman, V.M. Fokin: Dynamics of first-order phase transitions in multicomponent systems: A new theoretical approach, J. Colloid. Interface Sci. **272**, 109–133 (2004)
4.43 P.G. Vekilov: Nucleation, Cryst. Growth Des. **10**, 5007–5019 (2010)
4.44 K.F. Kelton, A.L. Greer, C.V. Thompson: Transient nucleation in condensed systems, J. Chem. Phys. **79**, 6261–6276 (1983)

4.45 A. Dillmann, G.E.A. Meier: Homogeneous nucleation of supersaturated vapors, Chem. Phys. Lett. **160**, 71–74 (1989)

4.46 K. Lakshmi Narayan, K.F. Kelton, C.S. Ray: Effect of Pt doping on nucleation and crystallization in Li_2O–$2SiO_2$ glass: experimental measurements and computer modeling, J. Non-Cryst. Solids **195**, 148–157 (1996)

4.47 K.S. Ranasinghe, P.F. Wei, K.F. Kelton, C.S. Ray, D.E. Day: Verification of an analytical method for measuring crystal nucleation rates in glasses from DTA data, J. Non-Cryst. Solids **337**, 261–267 (2004)

4.48 J.W. Cahn, J.E. Hilliard: Free energy of a nonuniform system. I. Interfacial free energy, J. Chem. Phys. **28**, 258–267 (1958)

4.49 J.W. Cahn: Spinodal decomposition, Acta Metall. **9**, 795–801 (1961)

4.50 J.W. Cahn, R.J. Charles: Initial stages of phase separation in glasses, Phys. Chem. Glasses **6**, 181–191 (1965)

4.51 J.W.P. Schmelzer: Crystal nucleation and growth in glass-forming melts: Experiment and theory, J. Non-Cryst. Solids **354**, 269–278 (2008)

4.52 P.G. Vekilov: Dense liquid precursor for the nucleation of ordered solid phases from solution, Cryst. Growth Des. **4**, 671–685 (2004)

4.53 J.W.P. Schmelzer, V.G. Baidakov, G.S. Boltachev: Kinetics of boiling in binary liquid-gas solutions: Comparison of different approaches, J. Chem. Phys. **119**, 6166–6183 (2003)

4.54 J.W.P. Schmelzer, G.S. Boltachev, V.G. Baidakov: Classical and generalized Gibbs' approaches and the work of critical cluster formation in nucleation theory, J. Chem. Phys. **124**, 194503 (2006)

4.55 A.S. Abyzov, J.W.P. Schmelzer, A.A. Kovalchuk, V.V. Slezov: Evolution of cluster size-distributions in nucleation–growth and spinodal decomposition processes in a regular solution, J. Non-Cryst. Solids **356**, 2915–2922 (2010)

4.56 J.W.P. Schmelzer, A.S. Abyzov, J. Moller: Nucleation versus spinodal decomposition in phase formation processes in multicomponent solutions, J. Chem. Phys. **121**, 6900–6917 (2004)

4.57 J.F. Lutsko, G. Nicolis: Theoretical evidence for a dense fluid precursor to crystallization, Phys. Rev. Lett. (2006), https://doi.org/10.1103/PhysRevLett.96.046102

4.58 P.R. ten Wolde, D. Frenkel: Enhancement of protein crystal nucleation by critical density fluctuations, Science **277**, 1975–1978 (1997)

4.59 V.J. Anderson, H.N.W. Lekkerkerker: Insights into phase transition kinetics from colloid science, Nature **416**, 811–815 (2002)

4.60 S.T. Yau, P.G. Vekilov: Direct observation of nucleus structure and nucleation pathways in apoferritin crystallization, J. Am. Chem. Soc. **123**, 1080–1089 (2001)

4.61 D. Erdemir, A.Y. Lee, A.S. Myerson: Nucleation of crystals from solution: Classical and two-step models, Acc. Chem. Res. **42**, 621–629 (2009)

4.62 W. Pan, A.B. Kolomeisky, P.G. Vekilov: Nucleation of ordered solid phases of proteins via a disordered high-density state: Phenomenological approach, J. Chem. Phys. **122**, 174905 (2005)

4.63 J. de Yoreo: Crystal nucleation: More than one pathway, Nat. Mater. **12**, 284–285 (2013)

4.64 W. Holand, V. Rheinberger, M. Schweiger: Control of nucleation in glass ceramics, Philos. Trans. R. Soc. Math. Phys. Eng. Sci. **361**, 575–588 (2003)

4.65 L.R. Pinckney, G.H. Beall: Microstructural evolution in some silicate glass-ceramics: A review, J. Am. Ceram. Soc. **91**, 773–779 (2008)

4.66 E.D. Zanotto, V.M. Fokin: Recent studies of internal and surface nucleation in silicate glasses, Philos. Trans. R. Soc. Math. Phys. Eng. Sci. **361**, 591–0612 (2003)

4.67 S.D. Stookey: Catalyzed crystallization of glass in theory and practice, Ind. Eng. Chem. **51**, 805–808 (1959)

4.68 M. Dittmer, M. Müller, C. Rüssel: Self-organized nanocrystallinity in MgO–Al_2O_3–SiO_2 glasses with ZrO_2 as nucleating agent, Mater. Chem. Phys. **124**, 1083–1088 (2010)

4.69 G.H. Beall, B.R. Karstett, H.L. Rittler: Crystallization and chemical strengthening of stuffed beta-quartz glass-ceramics, J. Am. Ceram. Soc. **50**, 181–190 (1967)

4.70 G.H. Beall: Design and properties of glass-ceramics, Annu. Rev. Mater. Sci. **22**, 91–119 (1992)

4.71 C. Patzig, T. Höche, M. Dittmer, C. Rüssel: Temporal evolution of crystallization in MgO–Al_2O_3–SiO_2–ZrO_2 glass ceramics, Cryst. Growth Des. **12**, 2059–2067 (2012)

4.72 S. Bhattacharyya, C. Bocker, T. Heil, J.R. Jinschek, T. Höche, C. Rüssel, H. Kohl: Experimental evidence of self-limited growth of nanocrystals in glass, Nano Lett. **9**, 2493–2496 (2009)

4.73 T. Höche, C. Patzig, T. Gemming, R. Wurth, C. Rüssel, I. Avramov: Temporal evolution of diffusion barriers surrounding $ZrTiO_4$ nuclei in lithia aluminosilicate glass-ceramics, Cryst. Growth Des. **12**, 1556–1563 (2012)

4.74 G.H. Beall, L.R. Pinckney: Nanophase glass-ceramics, J. Am. Ceram. Soc. **82**, 5–16 (1999)

4.75 M.J. Dejneka: The luminescence and structure of novel transparent oxyfluoride glass-ceramics, J. Non-Cryst. Solids **239**, 149–155 (1998)

4.76 M. Höland, A. Dommann, W. Holand, V. Rheinberger: Microstructure formation and surface properties of a rhenanite-type glass-ceramic containing 6.0 wt% P_2O_5, Glass Sci. Technol. **78**, 153–158 (2005)

4.77 J. Macdowell, G.H. Beall: Immiscibility and crystallization in Al_2O_3–SiO_2 glasses, J. Am. Ceram. Soc. **52**, 17–25 (1969)

4.78 S. Chenu, E. Véron, C. Genevois, G. Matzen, T. Cardinal, A. Etienne, D. Massiot, M. Allix: Tuneable nanostructuring of highly transparent zinc gallogermanate glasses and glass-ceramics, Adv. Opt. Mater. **2**, 364–372 (2014)

4.79 S. Chenu, E. Véron, C. Genevois, A. Garcia, G. Matzen, M. Allix: Long-lasting luminescent $ZnGa_2O_4$:Cr^{3+} transparent glass-ceramics, J. Mater. Chem. C **2**, 10002–10010 (2014)

4.80 P.F. James: Glass-ceramics – New compositions and uses, J. Non-Cryst. Solids **181**, 1–15 (1995)
4.81 C.J. Brinker, G.W. Scherer: *Sol-Gel Science* (Academic, New York 1990)
4.82 T. Ban, Y. Ohta, Y. Takahashi: Low-temperature crystallization of forsterite and orthoenstatite, J. Am. Ceram. Soc. **82**, 22–26 (1999)
4.83 E. Bernardo, G. Scarinci, E. Edme, U. Michon, N. Planty: Fast-sintered gehlenite glass-ceramics from plasma-vitrified municipal solid waste incinerator fly ashes, J. Am. Ceram. Soc. **92**, 528–530 (2009)
4.84 D.T. Weaver, D.C. Van Aken, J.D. Smith: The role of bulk nucleation in the formation of crystalline cordierite coatings produced by air plasma spraying, Mater. Sci. Eng. A **339**, 96–102 (2003)
4.85 C.R. Chang, J.H. Jean: Crystallization kinetics and mechanism of low-dielectric, low-temperature, cofirable $CaO-B_2O_3-SiO_2$ glass-ceramics, J. Am. Ceram. Soc. **82**, 1725–1732 (1999)
4.86 W. Wisniewski, M. Patschger, S. Murdzheva, C. Thieme, C. Rüssel: Oriented nucleation of both Ge-fresnoite and benitoite/$BaGe_4O_9$ during the surface crystallisation of glass studied by electron backscatter diffraction, Sci. Rep. (2016), https://doi.org/10.1038/srep20125
4.87 T. Höche, R. Keding, C. Rüssel, R. Hergt: Microstructural characterization of grain-oriented glass-ceramics in the system $Ba2TiSi_2O_8-SiO_2$, J. Mater. Sci. **34**, 195–208 (1999)
4.88 W. Holand, M. Frank, V. Rheinberger: Surface crystallization of leucite in glasses, J. Non-Cryst. Solids **180**, 292–307 (1995)
4.89 J. Schneider, V.R. Mastelaro, H. Panepucci, E.D. Zanotto: Si-29 MAS-NMR studies of Q(n) structural units in metasilicate glasses and their nucleating ability, J. Non-Cryst. Solids **273**, 8–18 (2000)
4.90 D.S. Jung, J.M. Han, Y.C. Kang: Sintering characteristics of $CaO-B_2O_3-SiO_2$ glass-ceramic powders prepared by spray pyrolysis, J. Ceram. Process. Res. **10**, 77–80 (2009)
4.91 M. Albakry, M. Guazzato, M.V. Swain: Influence of hot pressing on the microstructure and fracture toughness of two pressable dental glass-ceramics, J. Biomed. Mater. Res. Part B **71B**, 99–107 (2004)
4.92 W. Wisniewski, M. Patschger, C. Rüssel: Viscous fingering and dendritic growth of surface crystallized $Sr_2TiSi_2O_8$ fresnoite, Sci. Rep. (2013), https://doi.org/10.1038/srep03558
4.93 M. Wada, M. Ninomiya: Glass-ceramic architectural cladding materials, Sci. Tech. Compost. Mater. **30**, 846–850 (1995)
4.94 M. Hubert, G. Delaizir, J. Monnier, C. Godart, H.L. Ma, X.H. Zhang, L. Calvez: An innovative approach to develop highly performant chalcogenide glasses and glass-ceramics transparent in the infrared range, Opt. Express **19**, 23513–23522 (2011)
4.95 A. Stone, M. Sakakura, Y. Shimotsuma, G. Stone, P. Gupta, K. Miura, K. Hirao, V. Dierolf, H. Jain: Directionally controlled 3D ferroelectric single crystal growth in $LaBGeO_5$glass by femtosecond laser irradiation, Opt. Express **17**, 23284–23289 (2009)
4.96 D. Savytskii, B. Knorr, V. Dierolf, H. Jain: Demonstration of single crystal growth via solid-solid transformation of a glass, Sci. Rep. (2016), https://doi.org/10.1038/srep23324
4.97 D.I.H. Atkinson, P.W. McMillan: Glass-ceramics with random and oriented microstructures – Part 2. Physical-properties of a randomly oriented glass-ceramic, J. Mater. Sci. **11**, 994–1002 (1976)
4.98 O. Anspach, R. Keding, C. Rüssel: Oriented lithium disilicate glass-ceramics prepared by electrochemically induced nucleation, J. Non-Cryst. Solids **351**, 656–662 (2005)
4.99 C. Moisescu, C. Jana, S. Habelitz, G. Carl, C. Rüssel: Oriented fluoroapatite glass-ceramics, J. Non-Cryst. Solids **248**, 176–182 (1999)
4.100 U. Ding, Y. Miura, S. Nakaoka, T. Nanba: Oriented surface crystallization of lithium niobate on glass and second harmonic generation, J. Non-Cryst. Solids **259**, 132–138 (1999)
4.101 C. Rüssel: Oriented crystallization of glass. A review, J. Non-Cryst. Solids **219**, 212–218 (1997)
4.102 Y. Ding, Y. Miura, A. Osaka: Polar-oriented crystallization of fresnoite ($Ba_2TiSi_2O_8$) on glass-surface due to ultrasonic treatment with suspensions, J. Am. Ceram. Soc. **77**, 2905–2910 (1994)
4.103 J. Llorca, V.M. Orera: Directionally solidified eutectic ceramic oxides, Prog. Mater. Sci. **51**, 711–809 (2006)
4.104 S.D. Stookey: Photosensitive glass – A new photographic medium, Ind. Eng. Chem. **41**, 856–861 (1949)
4.105 V.M. Fokin, G.P. Souza, E.D. Zanotto, J. Lumeau, L. Glebova, L.B. Glebov: Sodium fluoride solubility and crystallization in photo-thermo-refractive glass, J. Am. Ceram. Soc. **93**, 716–721 (2010)
4.106 J. Lumeau, A. Sinitskii, L. Glebova, L.B. Glebov, E.D. Zanotto: Spontaneous and photo-induced crystallisation of photo-thermo-refractive glass, Phys. Chem. Glass. – Eur. J. Glass Sci. Technol. B **48**, 281–284 (2007)
4.107 R. Ihara, T. Honma, Y. Benino, T. Fujiwara, R. Sato, T. Komatsu: Writing of two-dimensional crystal curved lines at the surface of $Sm_2O_3-Bi_2O_3-B_2O_3$ glass by samarium atom heat processing, Solid State Commun. **136**, 273–277 (2005)
4.108 A. Royon, K. Bourhis, M. Bellec, G. Papon, B. Bousquet, Y. Deshayes, T. Cardinal, L. Canioni: Silver clusters embedded in glass as a perennial high capacity optical recording medium, Adv. Mater. **22**, 5282–5286 (2010)
4.109 E. Véron: *Synthèse et étude structurale de la gehlenite au bore* $Ca_2Al_{2-x}B_xSiO_7$*: mécanisme de substitution B/Al et ordre local*, PhD Thesis (Université d'Orléans, Orléans 2010)
4.110 C.S. Ray, Q.Z. Yang, W.H. Huang, D.E. Day: Surface and internal crystallization in classes as determined by differential thermal analysis, J. Am. Ceram. Soc. **79**, 3155–3160 (1996)
4.111 C.S. Ray, D.E. Day: An analysis of nucleation-rate type of curves in glass as determined by differential thermal analysis, J. Am. Ceram. Soc. **80**, 3100–3108 (1997)
4.112 C.S. Ray, D.E. Day: Determining the nucleation rate curve for lithium disilicate glass by differential

thermal-analysis, J. Am. Ceram. Soc. **73**, 439–442 (1990)
4.113 A. Marotta, A. Buri, F. Branda: Nucleation in glass and differential thermal-analysis, J. Mater. Sci. **16**, 341–344 (1981)
4.114 H.M. Rietveld: A profile refinement method for nuclear and magnetic structures, J. Appl. Cryst. **2**, 65–71 (1969)
4.115 A.F. Gualtieri: A guided training exercise of quantitative phase analysis using EXPGUI, http://www.ccp14.ac.uk/gsas/files/expgui_quant_ gualtieri.pdf (2003)
4.116 G.W. Brindley: XLV. The effect of grain or particle size on X-ray reflections from mixed powders and alloys, considered in relation to the quantitative determination of crystalline substances by X-ray methods, Philos. Mag. Ser. **36**, 347–369 (1945)
4.117 A.L. Patterson: The Scherrer formula for x-ray particle size determination, Phys. Rev. **56**, 978–982 (1939)
4.118 E.J. Mittemeijer, U. Welzel: The "state of the art" of the diffraction analysis of crystallite size and lattice strain, Z. Kristallog. **223**, 552–560 (2008)
4.119 A. Le Bail: Profile fitting, decomposition, and microstructural effects. In: *Accuracy in Powder Diffraction II*, NIST Special Publication, Vol. 846, ed. by E. Prince, J.K. Stalick (NIST, Gaithersburg 1992) p. 213
4.120 L. Lutterotti: Total pattern fitting for the combined size-strain-stress-texture determination in thin film diffraction, Nucl. Instrum. Methods Phys. Res. Sect. B **268**, 334–340 (2010)
4.121 O. Dargaud, L. Cormier, N. Menguy, L. Galoisy, G. Calas, S. Papin, G. Querel, L. Olivi: Structural role of Zr^{4+} as a nucleating agent in a $MgO-Al_2O_3-SiO_2$ glass-ceramics: A combined XAS and HRTEM approach, J. Non-Cryst. Solids **356**, 2928–2934 (2010)
4.122 W. Wisniewski, C. Rüssel: EBSD measurements of phlogopite glass ceramics, CrystEngComm **17**, 8671–8675 (2015)
4.123 W. Wisniewski, K. Takano, Y. Takahashi, T. Fujiwara, C. Rüssel: Microstructure of transparent strontium fresnoite glass-ceramics, Sci. Rep. (2015), https://doi.org/10.1038/srep09069
4.124 T. Höche: Crystallization in glass: elucidating a realm of diversity by transmission electron microscopy, J. Mater. Sci. **45**, 3683–3696 (2010)
4.125 O. Dargaud, G. Calas, L. Cormier, L. Galoisy, C. Jousseaume, G. Querel, M. Newville: In situ study of nucleation of zirconia in an $MgO-Al_2O_3-SiO_2$ glass, J. Am. Ceram. Soc. **93**, 342–344 (2010)
4.126 S. Bhattacharyya, T. Höche, J.R. Jinschek, I. Avramov, R. Wurth, M. Müller, C. Rüssel: Direct evidence of Al-rich layers around nanosized $ZrTiO_4$ in glass: Putting the role of nucleation agents in perspective, Cryst. Growth Des. **10**, 379–385 (2010)
4.127 C. Patzig, M. Dittmer, A. Gawronski, T. Hoeche, C. Rüssel: Crystallization of ZrO_2-nucleated $MgO/Al_2O_3/SiO_2$ glasses – A TEM study, CrystEngComm **16**, 6578–6587 (2014)
4.128 W. Vogel, L. Horn, H. Reiss, G. Volksch: Electronmicroscopical studies of glass, J. Non-Cryst. Solids **49**, 221–240 (1982)
4.129 O. Becker, K. Bange: Ultramicrotomy – An alternative cross-section preparation for oxidic thin-films on glass, Ultramicroscopy **52**, 73–84 (1993)
4.130 J. Ayache, L. Beaunier, J. Boumendil, G. Ehret, D. Laub: *Guide de Préparation des Échantillons Pour la Microscopie Électronique en Transmission* (MRCT-CNRS, Meudon 2007)
4.131 E. Apel, J. Deubener, A. Bernard, M. Holand, R. Müller, H. Kappert, V. Rheinberger, W. Holand: Phenomena and mechanisms of crack propagation in glass-ceramics, J. Mech. Behav. Biomed. Mater. **1**, 313–325 (2008)
4.132 E. Radlein, G.H. Frischat: Atomic force microscopy as a tool to correlate nanostructure to properties of glasses, J. Non-Cryst. Solids **222**, 69–82 (1997)
4.133 M. Eden: NMR studies of oxide-based glasses, Annu. Rep. Sect. C **108**, 177–221 (2012)
4.134 J.V. Hanna, M.E. Smith: Recent technique developments and applications of solid state NMR in characterising inorganic materials, Solid State Nucl. Magn. Reson. **38**, 1–18 (2010)
4.135 D. Massiot, F. Fayon, V. Montouillout, N. Pellerin, J. Hiet, C. Rolland, P. Florian, J.P. Coutures, L. Cormier, D.R. Neuville: Structure and dynamics of oxide melts and glasses: A view from multinuclear and high temperature NMR, J. Non-Cryst. Solids **354**, 249–254 (2008)
4.136 M.J. Duer: *Introduction to Solid-State NMR Spectroscopy* (Wiley, Hoboken 2005)
4.137 K. Mackenzie, M. Smith: *Multinuclear Solid-State NMR of Inorganic Materials* (Pergamon, Oxford 2002)
4.138 W.S. Price: Spin dynamics: Basics of nuclear magnetic resonance. In: *Concepts in Magnetic Resonance Part A*, 2nd edn., Vol. 34 (2009) pp. 60–61
4.139 D. Massiot, R.J. Messinger, S. Cadars, M. Deschamps, V. Montouillout, N. Pellerin, E. Véron, M. Allix, P. Florian, F. Fayon: Topological, geometric, and chemical order in materials: Insights from solid-state NMR, Acc. Chem. Res. **46**, 1975–1984 (2013)
4.140 M. Guignard, L. Cormier, V. Montouillout, N. Menguy, D. Massiot, A.C. Hannon, B. Beuneu: Rearrangement of the structure during nucleation of a cordierite glass doped with TiO_2, J. Phys.-Cond. Matter (2010), https://doi.org/10.1088/0953-8984/22/18/185401
4.141 M. Goswami, G.P. Kothlyal, L. Montagne, L. Delevoye: MAS-NMR study of lithium zinc silicate glasses and glass-ceramics with various ZnO content, J. Solid State Chem. **181**, 269–275 (2008)
4.142 D. de Lygny, D.R. Neuville: Raman spectroscopy: A valuable tool to improve our understanding of nucleation and growth mechanism. In: *From Glass to Crystal – Nucleation, Growth and Phase Separation: From Research to Applications*, ed. by D.R. Neuville, L. Cormier, D. Caurant, L. Montagne (EDP Sciences, Les Ulis 2017)

4.143 Y. Takahashi, M. Osada, H. Masai, T. Fujiwara: Transmission electron microscopy and in situ Raman studies of glassy sanbornite: An insight into nucleation trend and its relation to structural variation, J. Appl. Phys. (2010), https://doi.org/10.1063/1.3487473

4.144 M. Bouska, S. Pechev, Q. Simon, R. Boidin, V. Nazabal, J. Gutwirth, E. Baudet, P. Němec: Pulsed laser deposited GeTe-rich GeTe-Sb_2Te_3 thin films, Sci. Rep. (2016), https://doi.org/10.1038/srep26552

4.145 J. Gaudin, O. Peyrusse, J. Chalupsky, M. Toufarova, L. Vysin, V. Hajkova, R. Sobierajski, T. Burian, S. Dastjani-Farahani, A. Graf, M. Amati, L. Gregoratti, S.P. Hau-Riege, G. Hoffmann, L. Juha, J. Krzywinski, R.A. London, S. Moeller, H. Sinn, S. Schorb, M. Stormer, T. Tschentscher, V. Vorlicek, H. Vu, J. Bozek, C. Bostedt: Amorphous to crystalline phase transition in carbon induced by intense femtosecond x-ray free-electron laser pulses, Phys. Rev. B (2012), https://doi.org/10.1103/PhysRevB.86.024103

4.146 G.E. Brown, F. Farges, G. Calas: X-ray scattering and x-ray spectroscopy studies of silicate melts, Struct. Dyn. Prop. Silic. Melts **32**, 317–410 (1995)

4.147 L. Cormier, O. Dargaud, N. Menguy, G.S. Henderson, M. Guignard, N. Trcera, B. Watts: Investigation of the role of nucleating agents in MgO-SiO_2-Al_2O_3-SiO_2-TiO_2 glasses and glass-ceramics: A XANES study at the Ti K- and $L_{2,3}$-edges, Cryst. Growth Des. **11**, 311–319 (2011)

4.148 H. Schnablegger, Y. Singh: *The SAXS Guide – Getting Acquainted with the Principles*, 2nd edn. (Anton Paar GmbH, Graz 2011)

4.149 G. Lelong, D.L. Price, M.L. Saboungi: Scattering techniques. In: *Nanoporous Materials*, ed. by N. Kamellopoulos (CRC Press, Boca Raton 2011)

4.150 A. Loshmano, V.N. Sigaev, R. Khodakov, N. Pavlushk, I. Yamzin: Small-angle neutron-scattering on silica glasses containing titania, J. Appl. Cryst. **7**, 207–210 (1974)

4.151 A.F. Wright, J. Talbot, B.E.F. Fender: Nucleation and growth studies by small-angle neutron-scattering and results for a glass-ceramic, Nature **277**, 366–368 (1979)

4.152 A.F. Wright, A.N. Fitch, J.B. Hayter, B.E.F. Fender: Nucleation and crystallization of cordierite TiO_2 glass-cermaic. I: Small-angle neutron-scattering measurements and simulations, Phys. Chem. Glasses **26**, 113–118 (1985)

4.153 U. Lembke, R. Bruckner, R. Kranold, T. Höche: Phase formation kinetics in a glass ceramic studied by small-angle scattering of X-rays and neutrons and by visible-light scattering, J. Appl. Crystallogr. **30**, 1056–1064 (1997)

4.154 M.P. Borom, A.M. Turkalo, R.H. Doremus: Strength and microstructure in lithium disilicate glass-ceramics, J. Am. Ceram. Soc. **58**, 385–391 (1975)

4.155 P. Bennema: Crystal growth from solution – Theory and experiment, J. Cryst. Growth **24/25**, 76–83 (1974)

4.156 K.A. Jackson: Theory of crystal growth. In: *Changes of state*, Treatise on Solid State Chemistry, Vol. 5, ed. by N.B. Hannay (Plenum, Boston 1975) pp. 233–288

4.157 R.J. Kirkpatrick, L. Klein, D.R. Uhlmann, J.F. Hays: Rates and proceses of crystal growth in the system anorthite-albite, J. Geophys. Res. **84**, 3671–3676 (1979)

4.158 Y. Oaki, H. Imai: Experimental demonstration for the morphological evolution of crystals grown in gel media, Cryst. Growth Des. **3**, 711–716 (2003)

4.159 N. Steno: *De solido intra solidum naturaliter contento*, https://archive.org/details/ita-bnc-mag-00001426-001 (1669)

4.160 J.-B.L. Romé de L'isle: *Cristallographie, ou Description des formes propres à tous les corps du règne minéral, dans l'état de combinaison saline, pierreuse ou métallique* (Paris 1783)

4.161 R.-J. Haüy: *Essai d'une Théorie sur la Structure des Crystaux* (Paris 1784)

4.162 V. Maier, G. Müller: Mechanisms of oxide nucleation in lithium aluminosilicate glass-ceramics, J. Am. Ceram. Soc. **70**, C176–C178 (1987)

4.163 G.H. Beall, D.A. Duke: Transparent glass-ceramics, J. Mater. Sci. **4**, 340–352 (1969)

4.164 E. Apel, C. van't Hoen, V. Rheinberger, W. Holand: Influence of ZrO_2 on the crystallization and properties of lithium disilicate glass-ceramics derived from a multi-component system, J. Eur. Ceram. Soc. **27**, 1571–1577 (2007)

4.165 H. Shao, K.M. Liang, F. Zhou, G.L. Wang, A.M. Hu: Microstructure and mechanical properties of MgO-Al_2O_3-SiO_2-TiO_2 glass-ceramics, Mater. Res. Bull. **40**, 499–506 (2005)

4.166 T. Uno, T. Kasuga, K. Nakajima: High-strenght mica-containing glass-ceramics, J. Am. Ceram. Soc. **74**, 3139–3141 (1991)

4.167 L.R. Pinckney: Transparent, high strain point spinel glass-ceramics, J. Non-Cryst. Solids **255**, 171–177 (1999)

4.168 M.J. Dejneka: Transparent oxyfluoride glass ceramics, MRS Bulletin **23**, 57–62 (1998)

4.169 S. Bhattacharyya, T. Höche, N. Hemono, M.J. Pascual, P.A. van Aken: Nano-crystallization in LaF_3-Na_2O-Al_2O_3-SiO_2 glass, J. Cryst. Growth **311**, 4350–4355 (2009)

4.170 S. Roy, B. Basu: On the development of two characteristically different crystal morphology in SiO_2-MgO-Al_2O_3-K_2O-B_2O_3-F glass-ceramic system, J. Mater. Sci.-Mater. Med. **20**, 51–66 (2009)

4.171 W.E. Lee, S.E. Arshad, P.F. James: Importance of crystallization hierarchies in microstructural evolution of silicate glass-ceramics, J. Am. Ceram. Soc. **90**, 727–737 (2007)

4.172 A. Gebhardt, T. Höche, G. Carl, I.I. Khodos: TEM study on the origin of cabbage-shaped mica crystal aggregates in machinable glass-ceramics, Acta Mater. **47**, 4427–4434 (1999)

4.173 W. Holand, M. Frank, V. Rheinberger: Opalescence in dental products, Thermochim. Acta **280**, 491–499 (1996)

4.174 W. Holand, V. Rheinberger, S. Wegner, M. Frank: Needle-like apatite-leucite glass-ceramic as a base material for the veneering of metal restorations in dentistry, J. Mater. Sci. – Mater. Med. **11**, 11–17 (2000)

4.175 K. Pengpat, D. Holland: Glass-ceramics containing ferroelectric bismuth germanate (Bi_2GeO_5), J. Eur. Ceram. Soc. **23**, 1599–1607 (2003)

4.176 T. Ryll, A. Brunner, S. Ellenbroek, A. Bieberle-Hutter, J.L.M. Rupp, L.J. Gauckler: Electrical conductivity and crystallization of amorphous bismuth ruthenate thin films deposited by spray pyrolysis, Phys. Chem. Chem. Phys. **12**, 13933–13942 (2010)

4.177 D.I. Atkinson, P.W. McMillan: Glass-ceramics with an aligned microstructure, J. Mater. Sci. **10**, 2012–2014 (1975)

4.178 T. Höche, S. Habelitz, I. Avramov: Crystal morphology engineering in SiO_2-Al_2O_3-MgO-K_2O-Na_2O-F-mica glass-ceramics, Acta Mater. **47**, 735–744 (1999)

4.179 G.H. Beall: Chain silicate glass-ceramics, J. Non-Cryst. Solids **129**, 163–173 (1991)

4.180 E.D. Zanotto: A bright future for glass-ceramics, Am. Ceram. Soc. Bull. **89**, 19–27 (2010)

4.181 W. Pannhorst: Recent developments for commercial applications of low expansion glass ceramics, Glass Technol. **45**, 51–53 (2004)

4.182 W. Pannhorst: Glass ceramics: state-of-the-art, J. Non-Cryst. Solids **219**, 198–204 (1997)

4.183 Z. Strnad: *Glass-Ceramic Materials: Liquid Phase Separation, Nucleation, and Crystallization in Glasses* (Elsevier, Amsterdam 1986)

4.184 J. Zimmer, F. Raether, G. Müller: In-situ investigations of sintering and crystallization of lithium aluminosilicate glass-ceramics, Glastech. Ber. – Glass Sci. Technol. **70**, 186–188 (1997)

4.185 J. Petzoldt, W. Pannhorst: Chemistry and structure of glass-ceramic materials for high-precision optical applications, J. Non-Cryst. Solids **129**, 191–198 (1991)

4.186 U. Schiffner, W. Pannhorst: Nucleation in a precursor glass for a Li_2O-Al_2O_3-SiO_2 glass ceramic. Part 1. Nucleation kinetics, Glastech. Ber. – Glass Sci. Technol. **60**, 211–221 (1987)

4.187 Y.H. Wang, J. Ohwaki: New transparent vitroceramics codoped with Er^{3+} and Yb^{3+} for efficient frequency up-conversion, Appl. Phys. Lett. **63**, 3268–3270 (1993)

4.188 F. Auzel, D. Pecile, D. Morin: Rare-earth doped vitroceramics – New, efficient, blue and green emitting materials for infrared up-conversion, J. Electrochem. Soc. **122**, 101–107 (1975)

4.189 J. Mendez-Ramos, V. Lavin, I.R. Martin, U.R. Rodriguez-Mendoza, V.D. Rodriguez, A.D. Lozano-Gorrin, P. Nunez: Role of the Eu^{3+} ions in the formation of transparent oxyfluoride glass ceramics, J. Appl. Phys. **89**, 5307–5310 (2001)

4.190 G. Mie: Articles on the optical characteristics of turbid tubes, especially colloidal metal solutions, Ann. Phys. **25**, 377–445 (1908)

4.191 J. Strutt: On the transmission of light through an atmosphere containing small particles in suspension, and on the origin of the blue of the sky, Philosoph. Mag. **47**, 375–394 (1899)

4.192 T. Berthier, V.M. Fokin, E.D. Zanotto: New large grain, highly crystalline, transparent glass-ceramics, J. Non-Cryst. Solids **354**, 1721–1730 (2008)

4.193 M. Kerker: *The Scattering of Light* (Academic, New York 1969)

4.194 R.W. Hopper: Stochastic-theory of scattering from idealized spinodal structures. Part 2. Scattering in general and for the basic late stage model, J. Non-Cryst. Solids **70**, 111–142 (1985)

4.195 M. Mattarelli, G. Gasperi, M. Montagna, P. Verrocchio: Transparency and long-ranged fluctuations: The case of glass ceramics, Phys. Rev B (2010), https://doi.org/10.1103/PhysRevB.82.094204

4.196 L.J. Andrews, G.H. Beall, A. Lempicki: Luminescence of Cr^{3+} in mullite transparent glass-ceramics, J. Lumin. **36**, 65–74 (1986)

4.197 R. Reisfeld: Potential uses of chromium(III)-doped transparent glass-ceramics in tunable lasers and luminescent solar concentrators, Mater. Sci. Eng. **71**, 375–382 (1985)

4.198 R. Reisfeld, A. Kisilev, A. Buch, M. Ish-Shalom: Transparent glass-ceramics doped by chromium(III) – Spectroscopic properties and characterization of crystalline phases, J. Non-Cryst. Solids **91**, 333–350 (1987)

4.199 A. Kisilev, R. Reisfeld, E. Greenberg, A. Buch, M. Ish-Shalom: Spectroscopy of chromium(III) in beta-quartz and petalite-like transparent glass-ceramics-ligand-field strengths of chromium(III), Chem. Phys. Lett. **105**, 405–408 (1984)

4.200 T. Nakanishi, K. Watanabe, J. Ueda, K. Fushimi, S. Tanabe, Y. Hasegawa: Enhanced light storage of $SrAl_2O_4$ glass-ceramics controlled by selective europium reduction, J. Am. Ceram. Soc. **98**, 423–429 (2015)

4.201 K. Al Saghir, S. Chenu, E. Véron, F. Fayon, M. Suchomel, C. Genevois, F. Porcher, G. Matzen, D. Massiot, M. Allix: Transparency through structural disorder: A new concept for innovative transparent ceramics, Chem. Mater. **27**, 508–514 (2015)

4.202 S. Tanabe, S. Fujita, S. Yoshihara, A. Sakamoto, S. Yamamoto: YAG glass-ceramic phosphor for white LED (II): Luminescence characteristics, Proc. SPIE **5941**, 594112-1 (2005)

4.203 S. Fujita, A. Sakamoto, S. Tanabe: Luminescence characteristics of YAG glass-ceramic phosphor for white LED, IEEE J. Sel. Top. Quantum Electron. **14**, 1387–1391 (2008)

4.204 A. Ikesue, Y.L. Aung: Ceramic laser materials, Nat. Photon. **2**, 721–727 (2008)

4.205 A. Ikesue: Polycrystalline Nd: YAG ceramics lasers, Opt. Mater. **19**, 183–187 (2002)

4.206 S. Alahraché, M. Deschamps, J. Lambert, M.R. Suchomel, D. De Sousa Meneses, G. Matzen, D. Massiot, E. Véron, M. Allix: Crystallization of Y_2O_3-Al_2O_3 Rich Glasses: Synthesis of YAG glass-ceramics, J. Phys. Chem. C **115**, 20499–20506 (2011)

4.207 X. Ma, X. Li, J. Li, C. Genevois, B. Ma, A. Etienne, C. Wan, E. Véron, Z. Peng, M. Allix: Pressureless glass crystallization of transparent yttrium aluminum garnet-based nanoceramics, Nat. Commun. **9**, 1175 (2018)

4.208 T. Nakanishi, Y. Katayama, J. Ueda, T. Honma, S. Tanabe, T. Komatsu: Fabrication of Eu:$SrAl_2O_4$-

based glass ceramics using Frozen sorbet method, J. Ceram. Soc. Jpn. **119**, 609–615 (2011)
4.209 T. Nakanishi, S. Tanabe: Novel Eu_{2+}-activated glass ceramics precipitated with green and red phosphors for high-power white LED, IEEE J. Sel. Top. Quantum Electron. **15**, 1171–1176 (2009)
4.210 G.H. Beall: Glass-ceramics for photonic applications, Glass Sci. Technol. – Glastech. Ber. **73**, 3–11 (2000)
4.211 L.R. Pinckney: Transparent beta-willemite glass-ceramics, Glass Sci. Technol. – Glastech. Ber. **73**, 329–332 (2000)
4.212 J.-S. Wang, F.-H. Shen: The development of SiO_2 resistant Cr-doped glass ceramics for high Cr^{4+} emission, J. Non-Cryst. Solids **358**, 246–251 (2012)
4.213 A.M. Malyarevich, I.A. Denisov, Y.V. Volk, K.V. Yumashev, O.S. Dymshits, A.A. Zhilin: Nanosized glass-ceramics doped with transition metal ions: Nonlinear spectroscopy and possible laser applications, J. Alloy. Compd. **341**, 247–250 (2002)
4.214 L.R. Pinckney: *Transparent Glass-Ceramics Based on ZnO Crystals*, Vol. 47 (Society of Glass Technology, Sheffield 2006)
4.215 G.H. Beall, L.R. Pinckney, B.N. Samson: Transparent gallate glass-ceramics. US Patent 6632758B2, Assigned to Corning Inc. (2003)
4.216 T. Suzuki, Y. Arai, Y. Ohishi: Quantum efficiencies of near-infrared emission from Ni^{2+}-doped glass-ceramics, J. Lumin. **128**, 603–609 (2008)
4.217 T. Suzuki, G.S. Murugan, Y. Ohishi: Optical properties of transparent Li_2O-Ga_2O_3-SiO_2 glass-ceramics embedding Ni-doped nanocrystals, Appl. Phys. Lett. **86**, doi:10.1063/1.1891272 (2005)
4.218 D. Deng, H. Ma, S. Xu, Q. Wang, L. Huang, S. Zhao, H. Wang, C. Li: Broadband infrared luminescence of Ni^{2+}-doped silicate glass-ceramics containing lithium aluminate spinel nanocrystals, J. Non-Cryst. Solids **357**, 1426–1429 (2011)
4.219 B.N. Samson, L.R. Pinckney, J. Wang, G.H. Beall, N.F. Borrelli: Nickel-doped nanocrystalline glass-ceramic fiber, Opt. Lett. **27**, 1309–1311 (2002)
4.220 S.S. Bayya, B.B. Harbison, J.S. Shanghera, I.D. Aggarwal: IR transmitting rare earth gallogermanate glass-ceramics. US Patent (1998)
4.221 S.S. Bayya, J.S. Sanghera, I.D. Aggarwal, J.A. Wojcik: Infrared transparent germanate glass-ceramics, J. Am. Ceram. Soc. **85**, 3114–3116 (2002)
4.222 S. Zhou, J. Hao, J. Qiu: Ultra-broadband near-infrared luminescence of Ni^{2+}:ZnO-Al_2O_3-SiO_2 nanocomposite glasses prepared by Sol-Gel method, J. Am. Ceram. Soc. **94**, 2902–2905 (2011)
4.223 C.X. Fan, B. Poumellec, M. Lancry, X. He, H.D. Zeng, A. Erraji-Chahid, Q.M. Liu, G.R. Chen: Three-dimensional photoprecipitation of oriented $LiNbO_3$-like crystals in silica-based glass with femtosecond laser irradiation, Opt. Lett. **37**, 2955–2957 (2012)
4.224 Y. Dai, H.L. Ma, B. Lu, B.K. Yu, B. Zhu, J.R. Qiu: Femtosecond laser-induced oriented precipitation of $Ba_2TiGe_2O_8$ crystals in glass, Opt. Express **16**, 3912–3917 (2008)
4.225 Y.J. Dai, X.W. Zhang, G.Y. Zhou: Phase transitional behavior in $K_{0.5}Na_{0.5}NbO_3$-$LiTaO_3$ ceramics, Appl. Phys. Lett. (2007), https://doi.org/10.1111/j.1551-2916.2011.04671.x
4.226 T. Honma, Y. Benino, T. Fujiwara, T. Komatsu, R. Sato: Technique for writing of nonlinear optical single-crystal lines in glass, Appl. Phys. Lett. **83**, 2796–2798 (2003)
4.227 T. Shiosaki, M. Adachi, H. Kobayashi, K. Araki, A. Kawabata: Elastic, piezoelectric, acoustooptic and electro-optic properties of $Li_2B_4O_7$, Jpn. J. Appl. Phys. **24**, 25–27 (1985)
4.228 D.D. Silva, A.R. Boccaccini: Industrial developments in the field of optically transparent inorganic materials: A survey of recent patents, Recent Pat. Mater. Sci. **1**, 56 (2008)
4.229 G. Partridge: Inorganic materials. Part 4. Transparent ceramics and glass-ceramics, Adv. Mater. **2**, 553–556 (1990)
4.230 M. Richardson, R. Gaume: Transparent ceramics for lasers – A game-changer, Am. Ceram. Soc. Bull. **91**, 30–33 (2012)
4.231 R. Won: View from...ASSP 2008: Ceramic future, Nat. Photonics **2**, 216–217 (2008)
4.232 A. Ikesue, T. Kinoshita, K. Kamata, K. Yoshida: Fabrication and optical-properties of high-performance polycristalline Nd-YAG ceramics for solid-state lasers, J. Am. Ceram. Soc. **78**, 1033–1040 (1995)
4.233 A. Krell, J. Klimke, T. Hutzler: Transparent compact ceramics: Inherent physical issues, Opt. Mater. **31**, 1144–1150 (2009)
4.234 Z.M. Seeley, J.D. Kuntz, N.J. Cherepy, S.A. Payne: Transparent Lu_2O_3:Eu ceramics by sinter and HIP optimization, Opt. Mater. **33**, 1721–1726 (2011)
4.235 U. Peuchert, Y. Okano, Y. Menke, S. Reichel, A. Ikesue: Transparent cubic-ZrO_2 ceramics for application as optical lenses, J. Eur. Ceram. Soc. **29**, 283–291 (2009)
4.236 M. Boyer, S. Alahraché, C. Genevois, M. Licheron, F.-X. Lefevre, C. Castro, G. Bonnefont, G. Patton, F. Moretti, C. Dujardin, G. Matzen, M. Allix: Enhanced transparency through second phase crystallization in $BaAl_4O_7$ scintillating ceramics, Cryst. Growth Des. **16**, 386–395 (2016)
4.237 M. Boyer, A.J.F. Carrion, S. Ory, A.I. Becerro, S. Villette, S.V. Eliseeva, S. Petoud, P. Aballea, G. Matzen, M. Allix: Transparent polycrystalline $SrREGa_3O_7$ melilite ceramics: potential phosphors for tuneable solid state lighting, J. Mater. Chem. C **4**, 3238–3247 (2016)
4.238 S. Alahraché, K. Al Saghir, S. Chenu, E. Véron, D. De Sousa Meneses, A.I. Becerro, M. Ocaña, F. Moretti, G. Patton, C. Dujardin, F. Cussó, J.P. Guin, M. Nivard, J.C. Sangleboeuf, G. Matzen, M. Allix: Perfectly transparent $Sr_3Al_2O_6$ polycrystalline ceramic elaborated from glass crystallization, Chem. Mater. **25**, 4017–4024 (2013)
4.239 M. Allix, S. Alahraché, F. Fayon, M. Suchomel, F. Porcher, T. Cardinal, G. Matzen: Highly transparent $BaAl_4O_7$ polycrystalline ceramic obtained by full crystallization from glass, Adv. Mater. **24**, 5570–5575 (2012)
4.240 A. Bertrand, J. Carreaud, S. Chenu, M. Allix, E. Véron, J.-R. Duclère, Y. Launay, T. Hayakawa, C. Genevois,

F. Brisset, F. Célarié, P. Thomas, G. Delaizir: Scalable and formable tellurite-based transparent ceramics for near infrared applications, Adv. Opt. Mater. **4**, 1482–1486 (2016)

4.241 M. Boyer, X. Yang, A.J. Fernández Carrión, Q. Wang, E. Véron, C. Genevois, L. Hennet, G. Matzen, E. Suard, D. Thiaudière, C. Castro, D. Pelloquin, L.B. Kong, X. Kuang, M. Allix: First transparent oxide ion conducting ceramics synthesized by full crystallization from glass, J. Mater. Chem. A **6**, 5276–5289 (2018)

4.242 A.J. Fernández-Carrión, K. Al Saghir, E. Véron, A.I. Becerro, F. Porcher, W. Wisniewski, G. Matzen, F. Fayon, M. Allix: Local disorder and tuneable luminescence in $Sr_{1-x/2}Al_{2-x}Si_xO_4$ ($0.2 \leq x \leq 0.5$) transparent ceramics, Inorg. Chem. **56**, 14446–14458 (2017)

4.243 J.B. Qiu, A. Makishima: Frequency up-conversion luminescence in Yb^{3+}-Ho^{3+} co-doped $Pb_xCd_{1-x}F_2$ nano-crystals precipitated transparent oxyfluoride glass-ceramics, Sci. Technol. Adv. Mater. **5**, 313–317 (2004)

4.244 M. Mortier, G. Patriarche: Structural characterisation of transparent oxyfluoride glass-ceramics, J. Mater. Sci. **35**, 4849–4856 (2000)

4.245 J.M. Jewell, E.J. Friebele, I.D. Aggarwal: Transparent heavy-metal fluoride glass-ceramic, J. Non-Cryst. Solids **188**, 285–288 (1995)

4.246 M. Mortier, A. Monteville, G. Patriarche, G. Maze, F. Auzel: New progresses in transparent rare-earth doped glass-ceramics, Opt. Mater. **16**, 255–267 (2001)

4.247 F. Auzel, K.E. Lipinska Kalita, P. Santa-Cruz: A new Er^{3+}-doped vitreous fluoride amplification medium with crystal-like cross-sections and reduced inhomogeneous line width, Opt. Mater. **5**, 75–78 (1996)

4.248 V. Lavin, I. Iparraguirre, J. Azkargorta, A. Mendioroz, J. Gonzalez-Platas, R. Balda, J. Fernandez: Stimulated and upconverted emissions of Nd^{3+} in a transparent oxyfluoride glass-ceramic, Opt. Mater. **25**, 201–208 (2004)

4.249 B.N. Samson, P.A. Tick, N.F. Borrelli: Efficient neodymium-doped glass-ceramic fiber laser and amplifier, Opt. Lett. **26**, 145–147 (2001)

4.250 J. Fu, J.M. Parker, P.S. Flower, R.M. Brown: Eu^{2+} ions and CaF_2-containing transparent glass-ceramics, Mater. Res. Bull. **37**, 1843–1849 (2002)

4.251 X.S. Qiao, X.P. Fan, J. Wang, M.Q. Wang: Luminescence behavior of Er^{3+} ions in glass-ceramics containing CaF_2 nanocrystals, J. Non-Cryst. Solids **351**, 357–363 (2005)

4.252 S. Ye, B. Zhu, J.X. Chen, J. Luo, J.R. Qiu: Infrared quantum cutting in Tb^{3+},Yb^{3+} codoped transparent glass ceramics containing CaF_2 nanocrystals, Appl. Phys. Lett. (2008), https://doi.org/10.1063/1.2907496

4.253 F. Goutaland, P. Jander, W.S. Brocklesby, G.J. Dai: Crystallisation effects on rare earth dopants in oxyfluoride glass ceramics, Opt. Mater. **22**, 383–390 (2003)

4.254 S. Ye, B. Zhu, J. Luo, J.X. Chen, G. Lakshminarayana, J.R. Qiu: Enhanced cooperative quantum cutting in Tm^{3+}-Yb^{3+} codoped glass ceramics containing LaF_3 nanocrystals, Opt. Express **16**, 8989–8994 (2008)

4.255 Y. Kawamoto, R. Kanno, J. Qiu: Upconversion luminescence of Er^{3+} in transparent SiO_2-PbF_2-ErF_3 glass ceramics, J. Mater. Sci. **33**, 63–67 (1998)

4.256 A. Biswas, G.S. Maciel, C.S. Friend, P.N. Prasad: Upconversion properties of a transparent Er^{3+}-Yb^{3+} co-doped LaF_3-SiO_2 glass-ceramics prepared by sol-gel method, J. Non-Cryst. Solids **316**, 393–397 (2003)

4.257 X.S. Qiao, X.P. Fan, J. Wang, M.Q. Wang: Judd-Ofelt analysis and luminescence behavior of Er^{3+} ions in glass ceramics containing SrF_2 nanocrystals, J. Appl. Phys. (2006), https://doi.org/10.1063/1.2189021

4.258 X.S. Qiao, X.P. Fan, M.Q. Wang: Luminescence behavior of Er^{3+} in glass ceramics containing BaF_2 nanocrystals, Scr. Mater. **55**, 211–214 (2006)

4.259 M. Mortier, F. Auzel: Rare-earth doped transparent glass-ceramics with high cross-sections, J. Non-Cryst. Solids **256**, 361–365 (1999)

4.260 Z. Pan, A. Ueda, R. Mu, S.H. Morgan: Upconversion luminescence in Er^{3+}-doped germanate-oxyfluoride and tellurium-germanate-oxyfluoride transparent glass-ceramics, J. Lumin. **126**, 251–256 (2007)

4.261 J. Lucas: Infrared glasses, Curr. Opin. Solid State Mater. Sci. **4**, 181–187 (1999)

4.262 X.H. Zhang, L. Calvez, V. Seznec, H.L. Ma, S. Danto, P. Houizot, C. Boussard-Pledel, J. Lucas: Infrared transmitting glasses and glass-ceramics, J. Non-Cryst. Solids **352**, 2411–2415 (2006)

4.263 C.G. Lin, L. Calvez, B. Bureau, H.Z. Tao, M. Allix, Z.X. Hao, V. Seznec, X.H. Zhang, X.J. Zhao: Second-order optical nonlinearity and ionic conductivity of nanocrystalline GeS_2-Ga_2S_3-LiI glass-ceramics with improved thermo-mechanical properties, Phys. Chem. Chem. Phys. **12**, 3780–3787 (2010)

4.264 M. Roze, L. Calvez, Y. Ledemi, M. Allix, G. Matzen, X.H. Zhang: Optical and mechanical properties of glasses and glass-ceramics based on the Ge-Ga-Se system, J. Am. Ceram. Soc. **91**, 3566–3570 (2008)

4.265 J.J. Mecholsky, G.R. Srinivas, P.B. Macedo, C.T. Moynihan: Chalcogenide glass-ceramics, Am. Ceram. Soc. Bull. **52**, 702–703 (1973)

4.266 J.J. Mecholsky: *Microstructural Investigations of a Chalcogenide Glass Ceramic*, PhD Thesis (Catholic Univ. of America, Washington 1973)

4.267 J. Cheng: Properties and structure of the infrared-transmitting arsenic-germanium-selenium-tin glass ceramic system, Huadong Huagong Xueyuan Xuebao **3**, 337–351 (1982)

4.268 X.H. Zhang, M.A. Hongli, J. Lucas: A new class of infrared transmitting glass-ceramics based on controlled nucleation and growth of alkali halide in a sulphide based glass matrix, J. Non-Cryst. Solids **337**, 130–135 (2004)

4.269 X.H. Zhang, B. Bureau, P. Lucas, C. Boussard-Pledel, J. Lucas: Glasses for seeing beyond visible, Chem. Eur. J. **14**, 432–442 (2008)

4.270 L. Calvez, M. Roze, Y. Ledemi, H.L. Ma, J. Lucas, M. Allix, G. Matzen, X.H. Zhang: Controlled crystallization in Ge-(Sb/Ga)-(S/Se)-MX glasses for

infrared applications, J. Ceram. Soc. Jpn. **116**, 1079–1082 (2008)
4.271 R. Balda, S. Garcia-Revilla, J. Fernandez, V. Seznec, V. Nazabal, X.H. Zhang, J.L. Adam, M. Allix, G. Matzen: Upconversion luminescence of transparent Er(3+)-doped chalcohalide glass-ceramics, Opt. Mater. **31**, 760–764 (2009)
4.272 M. Guignard, V. Nazabal, H.L. Ma, X.H. Zhang, H. Zeghlache, G. Martinelli, Y. Quiquempois, F. Smektala: Chalcogenide glass-ceramics for second harmonic generation, Phys. Chem. Glass. – Eur. J. Glass Sci. Technol. B **48**, 19–22 (2007)
4.273 M. Guignard, V. Nazabal, X.H. Zhang, F. Smektala, A. Moreac, S. Pechev, H. Zeghlache, A. Kudlinski, G. Martinelli, Y. Quiquempois: Crystalline phase responsible for the permanent second-harmonic generation in chalcogenide glass-ceramics, Opt. Mater. **30**, 338–345 (2007)
4.274 S.R. Ovshinsky: Reversible electrical switching phenomena in disordered structures, Phys. Rev. Lett. **21**, 1450 (1968)
4.275 J. Kalb, F. Spaepen, M. Wuttig: Atomic force microscopy measurements of crystal nucleation and growth rates in thin films of amorphous Te alloys, Appl. Phys. Lett. **84**, 5240–5242 (2004)
4.276 A. Hayashi, K. Minami, F. Mizuno, M. Tatsumisago: Formation of Li^+ superionic crystals from the Li_2S–P_2S_5 melt-quenched glasses, J. Mater. Sci. **43**, 1885–1889 (2008)
4.277 L.L. Hench: Bioceramics, J. Am. Ceram. Soc. **81**, 1705–1728 (1998)
4.278 L.L. Hench: Bioceramics – From concept to clinic, J. Am. Ceram. Soc. **74**, 1487–1510 (1991)
4.279 M. Guazzato, M. Albakry, S.P. Ringer, M.V. Swain: Strength, fracture toughness and microstructure of a selection of all-ceramic materials. Part II. Zirconia-based dental ceramics, Dent. Mater. **20**, 449–456 (2004)
4.280 I. Denry, J.A. Holloway: Ceramics for dental applications: A review, Materials **3**, 351–368 (2010)
4.281 W. Höland, G.H. Beall: Applications of Glass-Ceramics. In: *Glass-Ceramic Technology*, 2nd edn., (Wiley, Hoboken 2012)
4.282 T. Kokubo: A/W Glass-Ceramic: Processing and Properties. In: *An Introduction to Bioceramics*, ed. by L.L. Hench (World Scientific, Singapore 1993) pp. 75–88
4.283 T. Yamamuro, J. Shikata, H. Okumura, T. Kitsugi, Y. Kakutani, T. Matsui, T. Kokubo: Replacement of the lumbar vertebrae of sheep with ceramic prostheses, J. Bone Jt. Surg. Br. **72**, 889–893 (1990)
4.284 I.W. Donald: Immobilisation of radioactive and non-radioactive wastes in glass-based systems: an overview, Glass Technol. – Eur. J. Glass Sci. Technol. Part A **48**, 155–163 (2007)
4.285 I. Ojovan, W.E. Lee: *An Introduction to Nuclear Waste Immobilisation* (Elsevier, Oxford 2005)
4.286 P. Rigny, B. Bonin, J.M. Gras: The radioactive wastes management, Actual. Chim. **346**, 1–10 (2010)
4.287 W.E. Lee, M.I. Ojovan, M.C. Stennett, N.C. Hyatt: Immobilisation of radioactive waste in glasses, glass composite materials and ceramics, Adv. Appl. Ceram. **105**, 3–12 (2006)
4.288 I.W. Donald, B.L. Metcalfe, R.N.J. Taylor: The immobilization of high level radioactive wastes using ceramics and glasses, J. Mater. Sci. **32**, 5851–5887 (1997)
4.289 D. Caurant, P. Loiseau, O. Majérus, V. Aubin-Chevaldonnet, I. Bardez, A. Quintas: *Glasses, Glass-Ceramics and Ceramics for Immobilization of Highly Radioactive Nuclear Wastes* (Nova Science, Hauppauge 2009)
4.290 R.D. Rawlings, J.P. Wu, A.R. Boccaccini: Glass-ceramics: Their production from wastes – A review, J. Mater. Sci. **41**, 733–761 (2006)
4.291 P. Colombo, G. Brusatin, E. Bernardo, G. Scarinci: Inertization and reuse of waste materials by vitrification and fabrication of glass-based products, Curr. Opin. Solid State Mater. Sci. **7**, 225–239 (2003)
4.292 M. Romero, R.D. Rawlings, J.M. Rincon: Development of a new glass-ceramic by means of controlled vitrification and crystallisation of inorganic wastes from urban incineration, J. Eur. Ceram. Soc. **19**, 2049–2058 (1999)
4.293 Cofalit: qu'est ce que c'est? et le projet SESCO, http://europlasma.desforums.net/t37-cofalit-qu-est-ce-que-c-est-et-le-projet-sesco
4.294 J. Macdowell, G.H. Beall: Low K glass-ceramics for microelectronic packaging, Ceram. Trans. **15**, 259–277 (1990)
4.295 I.W. Donald: Preparation, properties and chemistry of glass-ceramic-to-metal and glass-ceramic-to-metal seals and coatings, J. Mater. Sci. **28**, 2841–2886 (1993)
4.296 P.A. Lessing: A review of sealing technologies applicable to solid oxide electrolysis cells, J. Mater. Sci. **42**, 3465–3476 (2007)
4.297 K.L. Ley, M. Krumpelt, R. Kumar, J.H. Meiser, J. Bloom: Glass-ceramic sealants for solid oxide fuel cells. Part 1. Physical properties, J. Mater. Res. **11**, 1489–1493 (1996)
4.298 R.N. Singh: Sealing technology for solid oxide fuel cells (SOFC), Int. J. Appl. Ceram. Technol. **4**, 134–144 (2007)
4.299 K. Hirose, T. Honma, Y. Benino, T. Komatsu: Glass-ceramics with $LiFePO_4$ crystals and crystal line patterning in glass by YAG laser irradiation, Solid State Ion **178**, 801–807 (2007)
4.300 A. Sakamoto, S. Yamamoto: Glass–Ceramics: Engineering principles and applications, Int. J. Appl. Glass Sci. **1**, 237–247 (2010)
4.301 X. Py, N. Calvet, R. Olives, P. Echegut, C. Bessada, F. Jay: Low-cost material for sensible heat based thermal storage to be used in thermodynamic solar power plants. In: *Proc. ASME 3rd Int. Conf. Energy Sust*, Vol. 2 (2009) pp. 527–532
4.302 X. Py, N. Calvet, R. Olives, A. Meffre, P. Echegut, C. Bessada, E. Véron, S. Ory: Recycled material for sensible heat based thermal energy storage to be used in concentrated solar thermal power plants, J. Solar Energy Eng. (2011), https://doi.org/10.1115/1.4004267

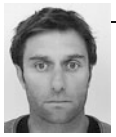

Mathieu Allix

University of Orléans
Orléans, France
mathieu.allix@cnrs-orleans.fr

Mathieu Allix received his PhD from the University of Caen, France, in 2004. He worked at the University of Liverpool (UK) and was appointed to a CNRS Researcher position in Orléans, France, in 2006. His research focuses on the elaboration and structure determination of innovative inorganic materials with a special interest to transparent glass-ceramics and transparent polycrystalline ceramics derived from fully crystallized glasses.

Laurent Cormier

IMPMC
Sorbonne University – CNRS
Paris, France
laurent.cormier@sorbonne-universite.fr

Laurent Cormier obtained his PhD from the University Pierre and Marie Curie – Paris 6, France in 1997 and worked at the Cavendish Laboratory, Cambridge University (UK) before joining CNRS in 1999. His research focuses on understanding the structure of glass at short and medium range order in relation to transport, nucleation and crystallization properties. He received the Gottardi Prize from the ICG.